Mathematical Models of Bacterial Chemotaxis

A Dissertation Presented for the

Doctor of Philosophy

Degree

The University of Tennessee, Knoxville

Mustafa Zeki Elmas

August 2018

I would like to dedicate this dissertation to my beautiful mother, who despite never seeing the inside of a classroom was able to instill upon me the importance of an education.

Acknowledgments

Undertaking this PhD has been a truly life-changing experience and would not have been possible without the support and guidance that I received from many individuals. I would like to acknowledge my appreciation to all of them.

First, I would like to express my sincere gratitude to my advisor Professor Vasilios Alexiades for the continuous support of my PhD study and related research, for his patience, motivation, and immense knowledge. His guidance has extended beyond the classroom as he became a father-like figure to me these past years. Dr. Alexiades showed immeasurable faith in me as his student, always helping me in research and in writing this thesis. I could not have imagined having a better advisor and mentor for my doctoral study. Your advice on both research as well as on my career have been invaluable.

Each of the members of my Dissertation Committee has provided me extensive personal and professional guidance and taught me a great deal about both scientific research and life in general. I would like to thank my Dissertation Committee: Professor Gladys Alexandre, Professor Xiaobing H. Feng, Professor Ohannes Karakashian, and Professor Vasileios Maroulas. Dr. Alexandre, thank you for all of your diligence in explaining and helping me to understand the biological background to develop my mathematical models. Drs. Feng, Karakashian, and Maroulas, thank you for thoroughly questioning and providing feedback to ultimately improve my research. I also want to thank all of you for contributing to making my defense an enjoyable and memorable moment. I know you are all busy individuals, but you always made time to support me and I thank you for that.

I gratefully acknowledge the funding sources that made my PhD possible, namely The University of Tennessee, Knoxville Mathematics Department and the National Science Foundation grants R01-1052148 and DMS-1216454.

I am grateful to all of those with whom I had the pleasure to work with during this and related projects. I am most appreciative to my collaborators for lending me their expertise and intuition to my scientific and technical problems. A very special thank you to Tanmoy Mukherjee for his invaluable advice and feedback and for always being so supportive of my work. I am indebted to Lindsey ONeal and Lam Vo who helped me in numerous ways during various stages of my PhD Without all of your laboratory experiments and data, my research would not have been possible.

I would be remiss to not include Dr. Suzanne Lenhart, Dr. Michael Frazier, Dr. Grozdena Todorova, Dr. Steven Wise, and Dr. Judy Day as you all taught me in classes that were an integral part of my research. To Ms. Pamela Armentrout, words cannot describe all that you have done for me assisting with paperwork, having all of the answers, and providing emotional support when I needed it the most. To Mr. Ben Walker and Ms. Angela Woofter, your technical support was irreplaceable. To Ms. Amanda Worsham, thank you for your help completing my travel paperwork so that I could attend workshops and conferences across the United States.

I cannot forget my friends - we went through hard times, but you always cheered me on and celebrated every accomplishment. My time at UT was more enjoyable due to the many friends and groups that became a part of my life. I wish to thank my friends in the mathematics department, Cara Sulyok, Ibrahim Aslan, and Mahir Demir, for all the great times that we have shared. I am grateful for time spent with my roommates, Mehmet Ayaz and Vincent Heningburg. To Cihan Eroglu, Mesut Keklik, Mehmet Alkan, and Farshad Sailimi, my backpacking buddies, our memorable trips into the mountains as well as travels through Knoxville, Nashville, and San Francisco provided unforgettable moments to relax and recharge to complete my research.

Last but not the least, I would like to express my deepest gratitude to my family for all their love, support, and sacrifices through not only this dissertation, but for life in general. My parents raised me with a love of mathematics and science, inspiring me in all my pursuits. My brothers and sisters instilled a positive energy to encourage me spiritually through all of the difficult times.

Without my advisor, mentors, family, and friends, this work would not have been possible.

Abstract

Bacterial chemotaxis, the ability of motile bacteria to navigate gradients of chemicals, plays key roles in the establishment of various plant-microbe associations, including those that benefit plant growth and crop productivity. The motile soil bacterium *Azospirillum brasilense* colonizes the rhizosphere of diverse plants across a range of environments. Aerotaxis, or the ability to navigate oxygen gradients is one of the strongest behavioral responses in *A. brasilense*. The aerotaxis response of *A. brasilense* is characterized by high precision with motile cells able to detect narrow regions in a gradient where the oxygen concentration is low enough (below 1%) to support their microaerobic lifestyle. We develop a model for aerotaxis band formation that captures most critical features of aerotaxis in *A. brasilense*. Remarkably, this model recapitulates experimental observations that were not captured in previous modeling efforts and further permits parameter values, which are difficult to obtain in experiments.

Single-particle tracking (SPT) has become an important method to study a number of well-characterized phenotypes including chemotaxis and cell migration. SPT methods extract the individual particle trajectories from time-lapse frames and provide useful information about both individual particle and collective behavior of particles. A large number of trajectories have to be analyzed to ensure that any inferences drawn from the observations are statistically representative of the particles. We develop an automated tracking software for free-swimming bacteria to track a large number of bacteria and analyze the resulting trajectories.

Biochemical pathways of chemotaxis in *A. brasilense* still remain elusive. This allows mathematical modeling to make testable predictions with biologically probable hypotheses about the biochemical mechanisms. The regulation of chemotaxis is achieved by a network

of interaction proteins constituting a signal transduction pathway. It has been recently found that *A. brasilense* cells have multiple (Che) systems whereas the model organism *Escherichia coli* possesses one chemotaxis system. We present a novel mathematical model to help determine the plausible network connectivity of chemotaxis pathways in *A. brasilense* by first developing four biologically plausible models and then invalidating all competing models, but one, which represents wild-type and all mutants data well.

Table of Contents

List of Tables

List of Figures

Chapter 1

Introduction

Many organisms live under spatially and temporally changing environmental conditions. They utilize information processing systems to constantly monitor their surrounding environments for important changes. The ability to detect and respond to these environmental changes is crucial for their metabolism, growth and survival. Bacteria have evolved a variety of mechanisms that enable them to sense changes in their living vicinity and respond appropriately to these changes they detect. Among the appropriate responses to environmental changes are alterations in physiology, development, virulence, or location [19]. Bacteria are the simplest organisms which respond to the environmental changes by movement. Motility and the ability of bacteria to orient their movement in a particular direction play essential role in their lifestyle. Bacteria sense changes in their surroundings and then move towards more beneficial and away from toxic environments that limit their growth and metabolism [22]. This mechanism is known as **chemotaxis**. It allows bacteria to locate niches that support optimal growth and metabolism. The chemicals affecting chemotaxis are called *chemoeffectors*. Chemotaxis in the direction of higher concentration gradient of a chemoeffector is defined as positive chemotaxis and these chemoeffectors are called *chemoattractants* (attractants), whereas chemotaxis away from higher concentration gradient of a chemoeffector is defined as negative chemotaxis and these chemoeffectors are called *chemorepellents* (repellents) [32].

Motile bacteria can detect and respond to a wide variety of environmental cues, including amino acids, sugars, pH, temperature, light, oxygen, osmolarity, magnetism and nutrients

[19, 44]. Behavioral responses to such environmental stimuli allow bacteria to find optimal conditions for their growth and metabolism in their surroundings. Taxis behaviors can be categorized as *chemotaxis* (taxis in chemical gradients), *aerotaxis* (movement in oxygen gradient), *phototaxis* (in response to light), *magnetotaxis* (in response to magnetic field), *thermotaxis* (in response to temperature), *osmotaxis* (in response to osmalirity), and *geotaxis* (in response to gravity) [115].

Bacteria are too small to detect spatial differences in the concentration of external stimuli. Rather than measuring concentrations at the different ends of their body, they detect gradients by use of a memory mechanism, which is based on a temporal comparison that requires a short term memory [111, 108]. This memory mechanism enables the bacteria to compare present and past environmental conditions [68]. Bacteria swim in one direction, and determine if the environmental conditions are getting better or worse for their lifestyle. If the conditions are getting better, they tend to keep swimming in the same directions. If the conditions are getting worse, they tend to change the swimming directions [100]. Motility in homogeneous (absense of chemoeffector gradient) environments consists of two main modes: swimming smoothly in the same direction for a period of time, called **runs**, and abruptly changing their swimming direction over a period of time, called **tumbles or reversals**. Run times ($>$ 1 second or so) are longer than the time spent in tumbling (0.1 second or so) [123]. The sequence of 'runs' and 'tumbles/reversals' results in a "random walk", which becomes biased when the environment is stimulated by a chemoeffector. Upon adding attractants or removing repellents, bacteria suppress the tumbles/reversals frequency (the rate at which the bacteria change their swimming direction), allowing them to bias their movement toward the region with beneficial environmental conditions. In contrast, when removing attractants or adding repellents, the motile cells change their swimming direction more frequently, allowing them to bias their movement to move away from the region with toxic environmental conditions. As a result, the sequence of runs and tumbles/reversals allows the bacteria to achieve a net motion towards chemoattractants or away from chemorepellents [68, 18, 33]. Fig.1.1 shows how tumbling/reversal frequency changes in response to attractants and repellents.

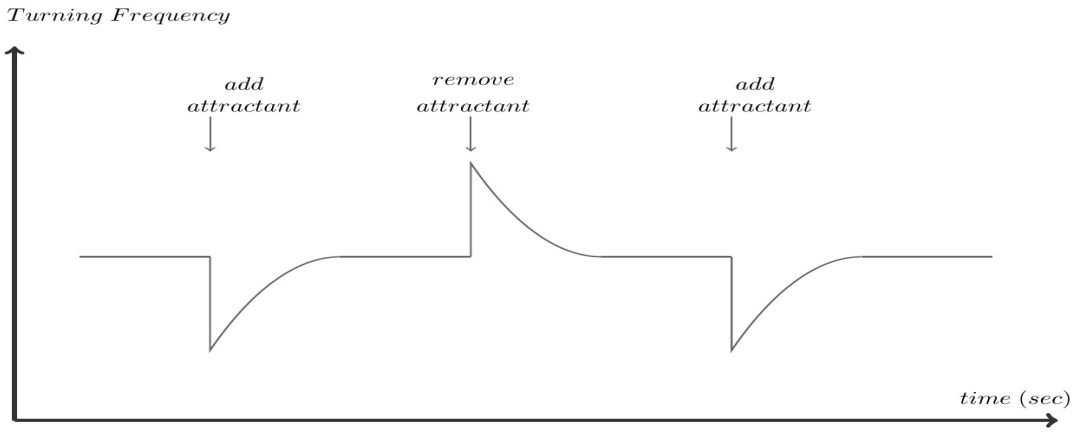

Figure 1.1: Changes in tumbles/reversals frequency in response to attractants and repellents.

The swimming pattern and motility characteristics depend on the number and distribution of flagella attached to the cell body [76]. In monotrichously flagellated bacteria (*Azospirillum brasilense*, *Vibrio cholera*, *Pseudomonas aerogenosa*), a single flagellum is attached to one end of their body. In lophotrichously flagellated cells (*Pseudomonas putida*, *Spirillum volutans*) there is a tuft of several flagella at one end of the cell. In peritrichously flagellated cells (*Esherichia coli*, *Bacillus subtilis*, *Salmonella typhimurium*) a uniform distribution of several flagella are attached across the cell body.

The most commonly studied *Esherichia coli* (*E. coli*) bacteria, being peritrichously flagellated, typically move in a sequence of persistent runs that are interupted by random changes in the swimming direction, tumbles. When flagellar motors rotate counterclockwise (CCW), flagella come together and form a bundle that pushes the cell forward, executing a run. On the other hand, when one or more of the flagellar motors rotate clockwise (CW), the flagella bundle flies apart and it leads to tumbling, [97, 7].

The model organism used in this study is the motile soil alphaproteobacterium **Azospirillum brasilense** (*A. brasilense*) that colonizes the rhizosphere of many agronomically important cereals and grasses, such as wheat, corn, maize, beans and rice, promoting plant growth [4, 99]. These gram-negative bacteria have the ability to fix atmospheric nitrogen under low oxygen concentration (microaerophilic conditions) [133]. Motility and chemotaxis

are vital traits of these soil bacteria that provide them a competitive advantage in the rhizosphere, allowing them to actively sense and move towards plant root exudates [128, 65].

The swimming pattern of the monotrichously flagellated *A. brasilense* cells with bi-directional motors is different from the *E. coli* run-and-tumble pattern [80, 45]. Single polar flagellated cells typically swim in a sequence of straight runs that are interrupted by sharp reversals in their swimming direction (run-reverse pattern). The direction of rotation of the flagellar motor determines whether the bacterium is swimming forward or reversing [79, 80]. When the flagellar motor rotates CCW, the flagellum drives the cell body from behind in a forward direction (pushing mode). When the motor rotates CW, the flagellum pulls the cell body in the backward direction (pulling mode). Reversals result by switching from pushing to pulling, changing their direction by an angle of 180° [91]. While resuming CCW rotation, a buckling instability of flagellar hook may occur switch reorients the cell in a new direction, named a **flick**, with turning angle of about 90°.Thus *A. brasilense* swimms by executing *run-reverse-flick* patterns.

Plant-microbe associations play vital role in plant health [99]. Soil harbors a diverse population of organisms which have developed various strategies to compete and survive in nutrient-limiting environments. Oxygen is one of the limiting nutrients in the rhizosphere where density and activity of organisms are greatest [65], making oxygen a potential modulator of competition in this environment. Motility and the ability of bacteria to locate niches that support optimum growth in the rhizosphere is essential for their survival. Bacterial chemotaxis enhances the competitive colonization abilities of *A. brasilense* cells in diverse rhizosperes [72, 83]. *A. brasilense* cells navigate to a region where the oxygen concentration is low enough (below 1%) to support their microaerobic lifestyle by using aerotaxis. Aerotaxis and chemotaxis serve as major mechanisms by which cells seek a position where metabolism is optimal [133]. Chemotaxis is achieved by modulation of reversal frequency. This behavior is achieved by a dedicated chemotaxis system which involves detecting the changes of environmental conditions by chemoreceptors, sending a signal through a signal transdution cascade to the fagella motors to produce an appropriate response and adaptation to the new environment [122]. Thus, the chemotaxis system allows the coordination of flagellar movement with sensing of the environmental changes. It is

important for bacteria to be able to perform chemotaxis since this mechanism gives the bacterium its ability to move up the gradient of favorable chemical concentrations.

A prominent feature of *A. brasilense* swimming in an oxygen gradient is the formation of an **aerotactic band**, a region where many bacteria congregate at their preferred oxygen concentration of about 0.4% avoiding both too low and too high oxygen.The band becomes visible in **spatial gradient assay** experiments, described later in Chapter 2, and its location and width are primary observable and measurable quantities in such experiments.

The aim of our work is to build mathematical models to help us understand the behavior of bacteria population under different environmental conditions, and to help us dicypher the connectivity of chemotaxis systems in the bacterium. The models allow us to make some testable predictions to understand the behavior of bacteria, and to determine parameter values, which are unattainable or very difficult to obtain by experiments.

This thesis is structured in the following way: In Chapter 2, a mathematical model of aerotactic band formation is described, and numerical simulations are presented. Chapter 3 describes the development of an image processing and analysis software package for tracking free-swimming cells from videos of experiments. It produces important motility parameters and statistic for swimming cells. Chapter 4 presents a novel and flexible mathematical model of biochemical signal transduction pathways in *A. brasilense* cells. We use it to determine possible connectivity of chemotaxis pathways by invalidating models of competing signaling pathways on the basis of experiments. We first developed four biologically plausible models of *A. brasilense* chemotaxis pathways. Parameters in these models were fitted so that all models represent wildtype experimental results well. The models were then compared to mutant data and three of them were invalidated.

Chapter 2

Aerotaxis Band Formation

2.1 Introduction

Aerotaxis is the ability of motile bacteria to move along gradients of oxygen. This bacterial behavior was first reported by Engelmann in 1881. He observed the aggregation of an organism around air bubbles [35, 36]. Beijerinck later confirmed Engelmanns finding and further described the formation of a sharp band of motile cells, corresponding to their accumulation, around a source of oxygen [11]. He also observed that the band of motile organisms descended when air was replaced with oxygen and ascended when air was replaced with hydrogen, implying that the organisms moved towards a specific concentration of oxygen. In 1901, Jennings and Crosby [57] observed that organisms prefer an specific oxygen concentration for their lifestyle. They also observed that the organisms swimming out of the zone immediately changed their swimming direction and returned to the zone. Pfeffer [87] observed that chemicals which can be attractant for one species may be repellent for other species. The preferred concentration of oxygen in a gradient has been determined for a few motile bacterial species (reviewed in [115]) including *Bacillus Subtilis* (an obligate aerobe) 200 μM; *Escherichia coli* (a facultative anaerobe) 50 μM; *Desulfovibrio vulgaris* (an aerotolerant anaerobe) 0.4 μM, and *A. brasilense* (a microaerobe) 3-5 μM.

2.2 Aerotactic band formation in *Azospirillum brasilense*

Azospirillum brasilense (*A. brasilense*) is a free-living, versatile soil alphaproteobacterium that colonizes the rhizosphere of many agronomically important cereals and grasses, such as wheat, corn, maize, beans and rice, promoting plant growth [4, 99]. These gram-negative bacteria are motile and have the ability to fix atmospheric nitrogen under low oxygen concentration (microaerophilic conditions) [133]. Motility and chemotaxis are vital traits of these soil bacteria that provide them a competitive advantage in the rhizosphere, allowing them to actively sense and move towards plant root exudates [128, 65]. *A. brasilense* cells swim by rotating a single bi-directional polar flagellum, Fig.2.1. When the direction of flagellar rotation switches, the swimming direction changes [3]. These cells use **run-and-reverse** strategy [16]. When the flagellar motor rotates counterclockwise (CCW), the flagellum pushes the cell forward, called **runs**. When the flagellar motor rotates clockwise (CW), it pulls the cell in the backward direction, a **reversal**, which may also reorient the cells in a new direction [132].

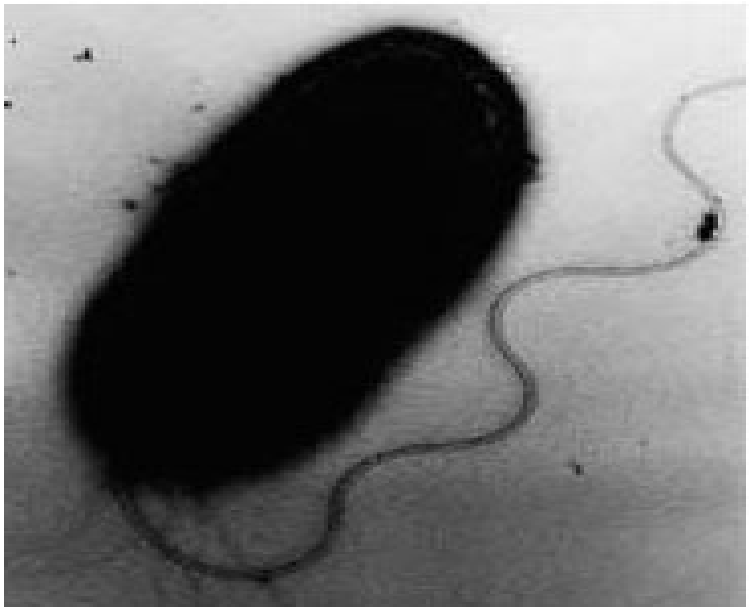

Figure 2.1: Microscopic image of Azospirillum brasilense. It is 1-2 μm long and has a single polar flagellum.

There are two types of aerotaxis responses known to date. In aerobes such as *B. subtilis* motile bacteria respond directly to the oxygen concentration and accumulate at the highest concentrations of oxygen in the gradient [55]. In other organisms, such as *E. coli* and *A. brasilense*, cells perform aerotaxis not by sensing oxygen itself, but by monitoring the effects that oxygen has on the metabolism of the cells [4]. This behavior is broadly referred to as energy taxis [115, 43]. In energy taxis-based aerotaxis, cells do not move toward the greatest concentration of oxygen but toward an intermediate concentration of oxygen that supports maximum energy levels. The signal for this type of behavior originates within the electron transport system, where oxygen-mediated changes in the rate of electron transport, redox status or proton motive force (PMF) are detected during aerotaxis [115].

Aerotaxis is a major behavioral response in *A. brasilense* and it is characterized by a remarkable ability to precisely locate niches where oxygen concentrations are low and optimum to support metabolism where cells form sharp bands. *A. brasilense* cells sense both high and very low oxygen concentrations as repellents while an intermediate concentrations oxygen of about 0.4% dissolved oxygen are attractants [133]. Aerotaxis guides *A. brasilense* to move towards microenvironments with a preferred low oxygen concentration, less than 0.5%, which is optimal for maximum energy generation and nitrogen fixation [133, 128]. The location and width of a band are primary observable and measurable quantities in aerotaxis experiments [84]. Note that 1% of oxygen in air corresponds 1300 μM dissolved oxygen in water.

A **spatial gradient assay** for aerotaxis is an experimental technique to expose cells to an oxygen gradient so as to form an observable band. Cells were grown to a desired optical density at 600nm (OD_{600nm}) of 0.4 to 0.6 (exponential phase of growth) in MMAB (Minimal Medium for Azospirillum brasilense) suplemented with malate (10 mM) and ammonium (18.7 nM). Optical density was adjusted between cultures to ensure that similar number of cells were compared across different samples. Cultures were adjusted to an equivalent number of cells by dilution in chemotaxis buffer. The motile cells were gently washed with chemotaxis buffer by centriffugation (5000 rpm for 3-4 minutes) and resuspended in 100μl MMAB containing malate as carbon source (10 mM). All cells remained motile under these conditions. Cells were transfered to an optically flat microcapillary tube (inner dimensions,

0.1 by 2 by 50 mm, Vitro Dynamics, Inc., Rockaway, N.J.) by immersing a capillary tube into the cell suspension. Aerotaxis was visualized under light microscope as the formation of a stable band of motile cells at a distance from the air-liquid interface (the meniscus). An aerotaxis band was formed within 1 to 3 minutes, depending on the oxygen concentration, and is stable for a minimum of 25 minutes under these conditions. The band moved closer to the meniscus and eventually disappeared when air (oxygen) was switched to nitrogen. The band was again formed when air was reintroduced. Temporal changes in aerotactic band formation, indicative of the ability of cells to sense changes in aeration, were analyzed by placing the same capillary tubes in the gas perfusion chamber and switching air flow from air to nitrogen flow. Distance from the meniscus was measured from the center of the meniscus to the center of the aerotactic band, and width of the aerotactic band was measured at the middle of the band upon formation of a stable band [83, 84, 133].

Aerotaxis is adventageous for cell survival because finding optimal concentration of oxygen is essential for cell metabolism and growth [2]. The bacteria monitor their internal energy levels and respond to a decrease in energy by swimming to a microenvironment that reenergizes the cells [115, 132]. In a spatial oxygen gradient, *A. brasilense* cells form a sharply defined aerotactic band, Fig.2.2, at a preferred oxygen concentration. The distance from the band and the air-water interface was 400 to 900 μm, depending on the carbon source and ocygen concentration was used for the experiments [84, 133]. It has been reported that PMF and other energy related parameters of the cells are maximum in the band [115, 133]. Bacteria swimming away from the band will encounter high or low oxygen concentrations, they will experience a loss of energy and return to the band. This supports the concept that the bacteria seek an intermediate concentration of oxygen [72].

2.3 Mathematical Model

Mathematical modeling of bacterial chemotaxis has been useful and insightful in helping to understand experimental observations. The hope is to get biologically meaningful results from mathematical models. In successful models, the mathematical analysis leads to insights which are unattainable or very diffucult to obtain experimentally.

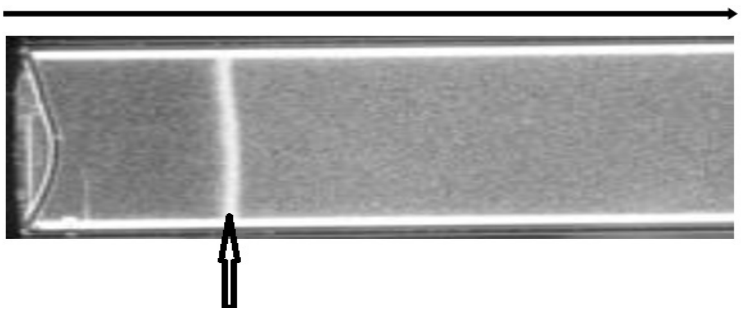

Figure 2.2: Aerotactic band formation in the spatial gradient assay. The wild-type *A. brasilense* cells formed an aerotactic band at a distance from the air-liquid interface where the disolved oxygen concentration is optimal for energy generation and nitrogen fixation. The horizontal arrow indicates the direction of the air gradient from the air-liquid interface and the vertical arrow indicates the location of the aerotactic band. The image was taken 5 minutes after placement of the cells in the capillary tube. Adopted from [16].

Modeling approaches for chemotaxis include: ODE models for signaling pathways [34, 74, 40], PDE models of various types for chemotactic movement, most commonly Keller-Segel type models [62], stochastic models of various types [64], [114], [29], and also agent-based models [61], [17].

The most extensively studied *mathematical* models for chemotaxis are *Keller-Segel type* models, named after the 1971 work of Evelyn Keller and Lee Segel [63], even though similar models were derived already by C.S. Patlak in 1953 [86]. Such models describe evolution of bacterial density by a parabolic PDE involving an anti-diffusion "chemotaxis term" proportional to the gradient of the chemoattractant, thus allowing movement up-the-gradient, the most prominent feature of chemotaxis. It has been shown that in 2 and higher (space) dimensions, under certain conditions, finite-time blow-up may occur which is clearly unphysical (sometimes interpreted as "overcrowding") [38]. An excellent summary of mathematical results on Keller-Segel models up to 2004 can be found in [53, 54].

In this work we employ a model for aerotactic band formation which considers the movement of bacteria in one dimension and distinguishes right- and left-moving bacteria depending on their swimming direction to the oxygen gradient by advection-reaction equations, and oxygen evolving by a diffusion equation with a sink term to account for its consumption by bacteria.

This type of model was formulated for chemotaxis by Lee Segel [101, 102], and it is more physical (and more "primitive", in the sense that under appropriate assumptions it reduces to the Keller-Segel model). Eventually it was adapted for aerotaxis by Mazzag et. al [72]. A great advantage of the model is that it incorporates experimentally measurable parameters, namely swimming speed and reversal frequencies, as it will be described below. While the work of Mazzag et.al [72] captured some of the features of the aerotaxis response of A. brasilense, it failed to produce a stable aerotactic band, which is typical of that formed by *A. brasilense*. Here, we use experimentally determined values and develop a model that accurately recapitulates various features of aerotaxis band formation in this bacterial species. Furthermore, we use the model to make a number of testable prediction by varying model parameters and provide experimental evidence that support these predictions.

2.3.1 Swimming of the Bacteria

We formulate a system of partial differential equations that describe movement of the bacteria whose reversal frequency is regulated by local oxygen concentration. We consider one-dimensional movement (along the x-axis) for simplicity, in an interval $0 \leq x \leq S$. The advection terms describe the directed swimming of bacteria with speed v, while the reaction terms denote the turning of bacteria at frequencies f_{RL} and f_{LR}. $R(x,t)$ and $L(x,t)$ are the number (densities) of right-moving and left-moving bacteria at position x and time t, respectively.

$$\frac{\partial R(x,t)}{\partial t} + v\frac{\partial R(x,t)}{\partial x} = -f_{RL}\, R(x,t) + f_{LR}\, L(x,t), \tag{2.1}$$

$$\frac{\partial L(x,t)}{\partial t} - v\frac{\partial L(x,t)}{\partial x} = +f_{RL}\, R(x,t) - f_{LR}\, L(x,t), \tag{2.2}$$

where v is the (constant) swimming speed, f_{LR} and f_{RL} are the probability with which bacteria reverse their direction from to left to right and from right to left, respectively, given by

$$f_{RL} = \begin{cases} F_{max} & if \quad \widehat{C}_{min} < C < C_{max} \\ F_{min} & if \quad C < \widehat{C}_{min} \quad or \quad C > C_{max}, \end{cases} \tag{2.3}$$

$$f_{LR} = \begin{cases} F_{max} & if \quad C_{min} < C < \widehat{C}_{max} \\ F_{min} & if \quad C > \widehat{C}_{max} \quad or \quad C < C_{min}, \end{cases} \tag{2.4}$$

where F_{max} and F_{min} are maximum and minimum reversal frequencies, respectively. $\widehat{C}_{min} < C_{min} < C_{max} < \widehat{C}_{max}$ are specified switch values of oxygen concentration C at which frequencies change from low F_{min} to high F_{max} and vice versa. The formulas are depicted in Fig.2.3.

In our implementation, we actually use different values for F_{max} inside and outside the band, which are found experimentally, see Table 2.1.

$B(x,t)$ will denote the concentration of bacteria, i.e. the total number of of right- and left-moving cells:

$$B(x,t) = R(x,t) + L(x,t). \tag{2.5}$$

Cell reproduction is much slower than band formation time-scale and it is ignored.

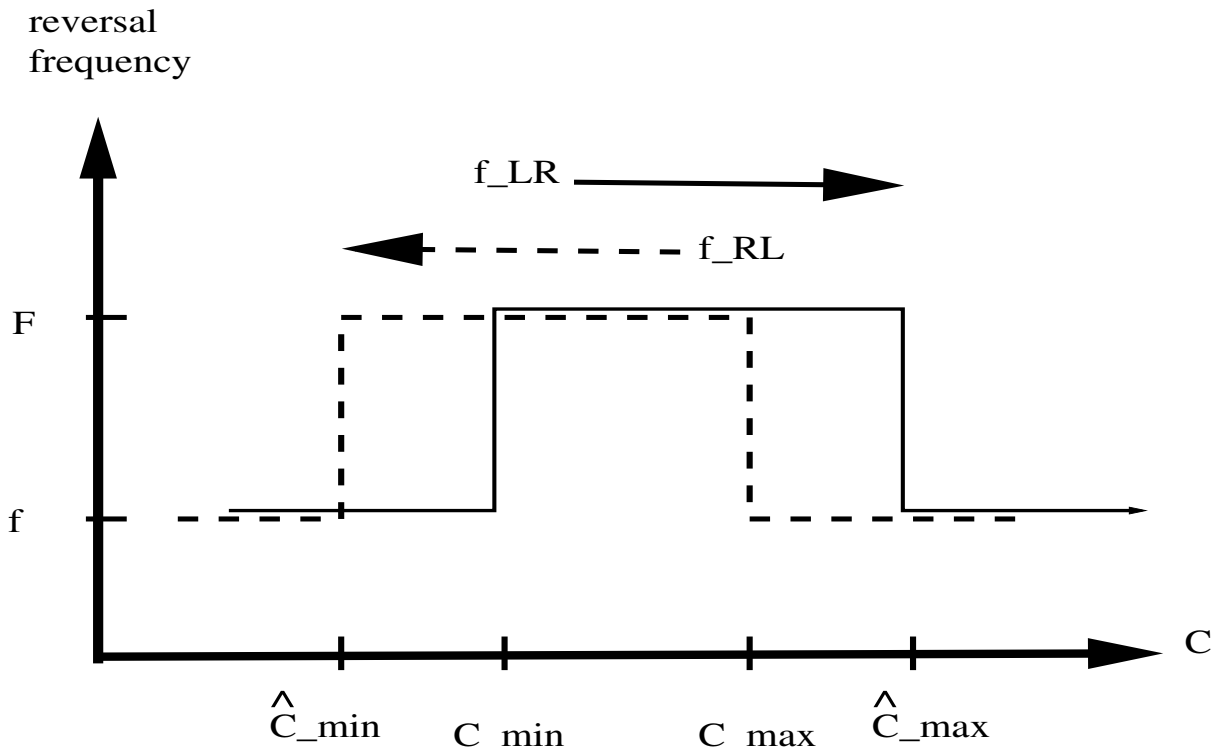

Figure 2.3: Reversal frequency of right swimming (solid line) and left swimming (dashed line) cells.

Initially, $R(x,0) = R_o(x)$ and $L(x,0) = L_o(x)$ in $[0\,, S]$, for some initial distributions $R_o(x)$ and $L_o(x)$. At the left boundary all left-moving cells turn to the right, and at the right boundary all right-moving cells turn to the left.

$$R(0,t) = L(0,t), \quad R(S,t) = L(S,t). \tag{2.6}$$

These boundary conditions ensure that there is no depletion of bacteria from the capillary. Thus the total number of bacteria in the capillary $[0\,, S]$ remains constant and equal to the initial number $B_o = R_o + L_o$:

$$\int_0^S B(x,t)dx = const. = B_o. \tag{2.7}$$

2.3.2 Diffusion of Oxygen

The oxygen concentration $C(x,t)$ in the capillary $[0,\ S]$ is determined by a diffusion-reaction equation that also accounts the consumption of oxygen by the bacteria,

$$\frac{\partial C(x,t)}{\partial t} = D\frac{\partial^2 C(x,t)}{\partial x^2} - K\,\theta(C(x,t))\,B(x,t)\,, \tag{2.8}$$

where $B(x,t)$ is the concentration of bacteria, K is the rate of consumption of oxygen by bacteria, and D is diffusion constant of oxygen in water. To ensure there is no consumption after oxygen depletion, $\theta(C)$ is set as

$$\theta(C(x,t)) = \begin{cases} 1 & \text{if } C(x,t) > 0, \\ 0 & \text{if } C(x,t) \le 0. \end{cases} \tag{2.9}$$

Initially there is no oxygen in the capillary, so the initial condition is $C(x,0) = 0$. At the open end $x = 0$ the oxygen concentration is a specified value C_o, while the other end of the capillary is sealed (with wax) to prevent oxygen from entering or leaving. Thus the boundary conditions are

$$C(0,t) = C_o\,, \qquad \frac{\partial C(x,t)}{\partial x} = 0 \quad \text{at } x = S\,. \tag{2.10}$$

2.4 Scaling and undimensionalization

It is useful to un-dimensionalize all variables in the model before computing, as it reduces the number of parameters, and prevents round-off errors due to arithmetic with large/small numbers. We rescale time, space, oxygen concentration, bacteria concentrations and oxygen consumption rate, by corresponding scales t_c, x_c, C_c, R_c, L_c, B_c,, K_c (to be chosen):

$$\tau = \frac{t}{t_c}, \quad \xi = \frac{x}{x_c}, \quad c = \frac{C}{C_c}, \quad r = \frac{R}{R_c}, \quad l = \frac{L}{L_c}, \quad b = \frac{B}{B_c}, \quad k = \frac{K}{K_c}.$$

We also set dimensionless frequencies

$$F_{rl} = f_{RL} t_c, \quad F_{lr} = f_{LR} t_c, \quad f_{max} = F_{max}\, t_c, \quad f_{min} = F_{min}\, t_c.$$

The diffusion equation (2.8) becomes

$$\frac{\partial c}{\partial \tau} = \frac{D t_c}{x_c^2} \frac{\partial^2 c}{\partial \xi^2} - \frac{K_c t_c B_c}{C_c} k\theta(c) b.$$

Setting $\frac{Dt_c}{x_c^2} = 1$, $\frac{K_c t_c B_c}{C_c} = 1$, $C_c = C_o$ (oxygen concentration at the meniscus) and $B_c = B_o$ (initial bacteria concentration), we obtain $t_c = \frac{x_c^2}{D}$ and $K_c = \frac{DC_o}{B_o x_c^2}$. Thus, (2.8) becomes

$$\frac{\partial c}{\partial \tau} = \frac{\partial^2 c}{\partial \xi^2} - k\,\theta(c)\,b \tag{2.8*}$$

The initial and boundary condition for the diffusion equation become

$$c(0,\tau) = 1, \qquad \frac{\partial c(\xi,\tau)}{\partial \xi} = 0 \tag{2.10*}$$

For the advection equations, choosing $R_c = L_c$ and setting $\frac{vt_c}{x_c} = 1$, we obtain $x_c = \frac{D}{v}$ (with $t_c = \frac{x_c^2}{D}$). Thus, equations (2.1) and (2.2) become

$$\frac{\partial r}{\partial \tau} + \frac{\partial r}{\partial \xi} = -F_{rl}\, r + F_{lr}\, l \tag{2.1*}$$

$$\frac{\partial l}{\partial \tau} - \frac{\partial l}{\partial \xi} = F_{rl}\, r - F_{lr}\, l \tag{2.2*}$$

and equations (2.3) and (2.4) become

$$F_{rl} = \begin{cases} f_{max} & \text{if} \quad \widehat{c}_{min} < c < c_{max} \\ f_{min} & \text{if} \quad c < \widehat{c}_{min} \quad \text{or} \quad c > c_{max}, \end{cases} \tag{2.3*}$$

$$F_{lr} = \begin{cases} f_{max} & \text{if} \quad C_{min} < C < \widehat{C}_{max} \\ f_{min} & \text{if} \quad C > \widehat{C}_{max} \quad or \quad C < C_{min}. \end{cases} \tag{2.4*}$$

The boundary conditions for right- and left-moving bacteria become

$$r(0,\tau) = l(0,\tau), \quad r\left(\frac{S}{x_c},\tau\right) = l\left(\frac{S}{x_c},\tau\right). \tag{2.6*}$$

2.5 Numerical Schemes

The equations describing the right-moving and the left-moving bacteria were discretized with an upwind Finite Volume scheme and forward Euler time discretization. The diffusion equation for oxygen was also discretized by Finite Volume scheme with forward Euler time discretization.

We divide the domain into M control volumes each of width $\Delta\xi = \frac{b-a}{M}$ where $a = 0$ and $b = \frac{S}{x_c}$. The nodes are: $\xi_i = a + (i - 1/2)\Delta\xi, \quad i = 1, \cdots, M$, and the faces of control volumes are indexed by $i - 1/2$ for $i = 1, \cdots, M + 1$, as seen in the figure below.

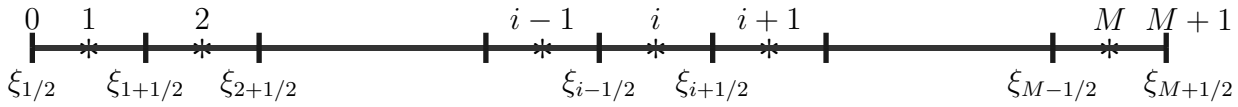

Figure 2.4: One dimensional space discretization for finite volume method

2.5.1 Finite volume discretization

The dimensionless equation (2.1*) can be written as

$$\frac{\partial r}{\partial \tau} + \frac{\partial F}{\partial \xi} = -F_{rl}\, r + F_{lr}\, l, \tag{2.11}$$

where flux $F = r$. Integrating (2.11) over each control volume $I_i = [\xi_{i-1/2}, \xi_{i+1/2}]$, we get

$$\int_{I_i} \frac{\partial r}{\partial \tau} d\xi + \int_{I_i} \frac{\partial F}{\partial \xi} d\xi = \int_{I_i} (-F_{rl}\, r + F_{lr}\, l) d\xi. \tag{2.12}$$

This equation can be rewriten as

$$\frac{d}{d\tau} \int_{I_i} r d\xi + F_{i+1/2} - F_{i-1/2} = \int_{I_i} (-F_{rl}\, r + F_{lr}\, l) d\xi. \tag{2.13}$$

Integrating the last equation over a timestep from τ_n to τ_{n+1}, we obtain

$$\int_{\tau_n}^{\tau_{n+1}} \frac{d}{d\tau} \int_{I_i} r d\xi d\tau + \int_{\tau_n}^{\tau_{n+1}} (F_{i+1/2} - F_{i-1/2}) d\tau = \int_{\tau_n}^{\tau_{n+1}} \int_{I_i} (-F_{rl}\, r + F_{lr}) d\xi d\tau. \tag{2.14}$$

Set the time-step $\Delta\tau = \tau_{n+1} - \tau_n$, and define the numerical quantities

$$\begin{aligned} r_i^n &= \frac{1}{\Delta\xi} \int_{\xi_{i-1/2}}^{\xi_{i+1/2}} r(\xi, \tau_n) d\xi \quad &&= \text{mean value of } r(\xi, \tau_n) \text{ over } I_i, \\ F_{i-1/2}^n &= \frac{1}{\Delta\tau} \int_{\tau_n}^{\tau_{n+1}} F_{i-1/2} d\tau \quad &&= \text{mean flux } F(\xi_{i-1/2}, \tau) \text{ during } [\tau_n, \tau_{n+1}] \ , \end{aligned} \tag{2.15}$$

which is assumed to be be the flux at τ_n making the scheme explicit. Plugging (2.15) into (2.14) and rearranging, we obtain the numerical scheme for equation (2.1*):

$$r_i^{n+1} = r_i^n + \frac{\Delta\tau}{\Delta\xi}(F_{i-1/2}^n - F_{i+1/2}^n) + \Delta\tau(-F_{rl}\, r_i^n + F_{lr}\, l_i^n), \quad i = 1, \cdots, M, \tag{2.16}$$

where $F_{i-1/2}^n = r_{i-1}^n$ (upwind scheme for advection). The numerical scheme for (2.2*) can be obtained similarly (with flux F $= -l$),

$$l_i^{n+1} = l_i^n + \frac{\Delta\tau}{\Delta\xi}(F_{i-1/2}^n - F_{i+1/2}^n) + \Delta\tau(F_{rl}\, r_i^n - F_{lr}\, l_i^n), \quad i = 1, \cdots, M, \tag{2.17}$$

where $F^n_{i-1/2} = -l^n_i$ (upwind with negative speed). Then the updated bacterial concentration of the i-th control volume is

$$b^{n+1}_i = r^{n+1}_i + l^{n+1}_i. \tag{2.18}$$

The dimensionless diffusion equation (2.8*) can be written as

$$\frac{\partial c}{\partial \tau} + \frac{\partial F}{\partial \xi} = -k\,\theta(c)\,b, \tag{2.19}$$

with flux $F = -\frac{\partial c}{\partial \xi}$ (Fick's law). Integrating (2.19) over control volume $I_i = [\xi_{i-1/2}, \xi_{i+1/2}]$, we get

$$\int_{I_i} \frac{\partial c}{\partial \tau} d\xi + \int_{I_i} \frac{\partial F}{\partial \xi} d\xi = \int_{I_i} -k\,\theta(c)\,b\,d\xi, \tag{2.20}$$

which can be rewriten as

$$\frac{d}{d\tau}\int_{I_i} c\,d\xi + F_{i+1/2} - F_{i-1/2} = \int_{I_i} -k\,\theta(c)\,b\,d\xi. \tag{2.21}$$

Integrating the last equation over time from τ_n to τ_{n+1}, we obtain

$$\int_{\tau_n}^{\tau_{n+1}} \frac{d}{d\tau}\int_{I_i} c\,d\xi d\tau + \int_{\tau_n}^{\tau_{n+1}} (F_{i+1/2} - F_{i-1/2}) d\tau = \int_{\tau_n}^{\tau_{n+1}}\int_{I_i} -k\,\theta(c)\,b\,d\xi d\tau \tag{2.22}$$

Set

$$c^n_i = \frac{1}{\Delta\xi}\int_{\xi_{i-1/2}}^{\xi_{i+1/2}} c(\xi,\tau_n)d\xi \quad = \text{mean value of } c(\xi,\tau_n) \text{ over } I_i\ , \tag{2.23}$$

and $F^n_{i-1/2}$ as in (2.15). Plugging into (2.22), we obtain the discretized diffusion-consumption equation:

$$c^{n+1}_i = c^n_i + \frac{\Delta\tau}{\Delta\xi}(F^n_{i-1/2} - F^n_{i+1/2}) - \Delta\tau\,k\,\theta(c^n_i)\,b^n_i, \quad i = 1, \cdots, M, \tag{2.24}$$

where $F^n_{i-1/2} = -\frac{c^n_i - c^n_{i-1}}{\Delta\xi}$ is the discrete diffusion flux.

2.5.2 Setting the timestep

The upwind scheme is stable if the following Courant-Friedrichs-Lewy condition (CFL) is satisfied: For the right-moving bacteria,

$$\frac{\Delta\tau}{\Delta\xi} + \Delta\tau F_{RL} \leq 1, \quad \text{which implies} \quad \Delta\tau \leq \frac{1}{\frac{1}{\Delta\xi} + F_{max}}, \tag{2.25}$$

and for left moving bacteria,

$$\frac{\Delta\tau}{\Delta\xi} + \Delta t F_{LR} \leq 1, \quad \text{which implies} \quad \Delta\tau \leq \frac{1}{\frac{1}{\Delta\xi} + F_{max}} =: \Delta\tau_{adv}. \tag{2.26}$$

Clearly, oxygen concentration should never become negative. However, the consumption term $k\,b$ is always a sink reducing c, and proportional to bacterial density b. To ensure that the numerical scheme preserves positivity, we use *adaptive* time stepping, obtained as follows. Rewriting (2.24), when $\theta = 1$, as

$$c_i^{n+1} = c_i^n - \Delta\tau(\frac{\Delta F_i^n}{\Delta\xi} + kb_i^n) \quad \text{with} \quad \Delta F_i^n = F_{i+1/2}^n - F_{i-1/2}^n, \tag{2.27}$$

we see that positivity of c, and stability, is ensured if

$$c_i^n - \Delta\tau(\frac{\Delta F_i^n}{\Delta\xi} + kb_i^n) \geq 0, \quad \text{which implies} \quad \Delta\tau \leq \frac{c_i^n}{\frac{\Delta F_i^n}{\Delta\xi} + kb_i^n}, \tag{2.28}$$

provided $\frac{c_i^n}{\frac{\Delta F_i^n}{\Delta\xi} + kb_i^n} > 0$. To ensure (2.28) holds for all $i = 1, \cdots, M$, we find the maximum of the denominator, and restrict $\Delta\tau$

$$\Delta\tau \leq \frac{\widehat{c}_{min}}{\max\limits_{i=1,\ldots M}(\frac{\Delta F_i^n}{\Delta\xi} + kb_i^n)} =: \Delta\tau_{diff}. \tag{2.29}$$

To satisfy both (2.26) and (2.29) the timestep is chosen to be $\Delta\tau = \min\Big(\Delta\tau_{adv}\,, \Delta\tau_{diff}\Big)$.

2.5.3 Implementation

The numerical scheme was implemented and solved in FORTRAN 90, compiled with *GNU gfortran* compiler on Linux. In the simulations presented below, We used a rather coarse mesh of $M = 640$ control volumes over the 5 mm interval $[0,\ S]$ (128 control volumes per millimeter).

In the simulations, we take the initial conditions for right-moving bacteria and left-moving bacteria to be equal to each other and equal to $B_o/2$. We tested sinusoidal perturbations of $B_o/2$ and found no detectable effect on the band, indicating (rather surprising) strong robustness to initial bacterial distribution.

The primary unknowns are the concentration of oxygen $C(x,t)$ and of bacteria $B(x,t) = R(x,t) + L(x,t)$, found from (2.24) and (2.16), (2.17).

We ouput **profiles**: values versus space at desired times, and **histories**: values versus time at desired locations, of (normalized) bacterial density $b = B/B_o$ and oxygen $c = C/C_o$. Thus, the initial b is 1, and c at $x = 0$ is 1.

However, the main interest is to find the location and width of the band at each timestep, and thus trace its evolution in time. The band becomes visible by plotting profiles of bacterial density, i.e. by plotting $b(x_i, t_n)$ versus space x_i at desired times t_n. It appears as a "bump", see Fig.2.5(b). Of course, the width of the bump is not uniform, so we must choose a rule of measuring width of such bumps. We quantify width as **Full Width at Half Maximum (FWHM)**, a standard measure used in many fields. This is done by finding: (1) the maximum and minimum values of the array $[b_i]$, and setting B_{half} as their average, (2) the location *xLeft* where the profile $b(x)$ first exceeds B_{half} (on the way up), (3) the location *xRght* where the profile $b(x) \le B_{half}$ (on the way down). Linear interpolation is used in (2),(3). Then width of bump at half max (FWHM) is $width = xRght - xLeft$, and **band location** is set as the midpoint $\frac{xLeft+xRght}{2}$.

To visualize evolution of the band, we output and plot the left-side *xLeft(t)* and right-side *xRght(t)* of the band as they evolve in time, see Fig.2.5(a). Also, we plot (normalized) oxygen profiles at times 50 s and 300 s, as in Fig.2.5(c), as well as histories of oxygen at a node to the left of the band and at a node inside the band, as in Fig.2.5(d).

2.6 Numerical simulations

The main results of the band formation model is decribed in this section. In all the simulations, bacteria formed a stable aerotactic band as it is observed in the actual experiments. The location and width of the band agree well with those measured for microaerophilic *A. brasilense* cells in [133, 84].

Below, we present a set of numerical simulations of aerotaxic band formation for *A. brasilense*, starting with the base case of parameter values listed in Table 2.1 validating the model against experiments. Then we conduct parametric studies to examine the effect of main parameters influencing the band.

Table 2.1: Parameter values for the aerotactic band formation model.

Parameter	Description	Value
B_o	Total bacteria concentration	7×10^8 cells/ml
C_o	Oxygen concentration at the meniscus	21%
D	Oxygen Diffusion coefficient	2×10^3 μm^2/s
K	oxygen consumption rate	4×10^{-9} μM ml/s/cell
v	Swimming speed	20 μm/s
F_{min}	min reversal frequency	0.35 /s
F_{max}	max reversal frequency inside the band	0.96 /s
F_{max}	max reversal frequency outside the band	0.65 /s
$\widehat{C}_{max}$	Upper switch oxygen concentration	10%
C_{max}	Upper favorable oxygen concentration	2%
C_{min}	Lower favorable oxygen concentration	0.3%
$\widehat{C}_{min}$	Lower detectable oxygen concentration	0.01%
S	Length of the capillary	5 mm

2.6.1 Model validation on wild type *A. brasilense* cells

We begin with results of simulations of actual experiments on wild type (Sp7) *A. brasilense* cells grown in malate (as food source). The spatial gradient assay experiments were conducted by Lindsey O'Neil at the Alexandre lab at the University of Tennessee, as described in §2.2. Experimentally measured band location and width were respectively 407

and 132 μm. Parameter values, along with experimentally measured values for v, F_{max}, F_{min} are listed in Table 2.1. Note that reversal frequencies were measured separately inside the band ($F_{max} = 0.96$ /s) and outside the band ($F_{max} = 0.65$ /s). Similarly, in the simulations we apply (2.3), (2.4) separately inside and outside the band.

We determined the switch parameters $\widehat{C}_{max}$, C_{max}, C_{min}, $\widehat{C}_{min}$ (for the base case shown in Fig. 2.5) to capture the experimentally measured band location and width. The bacterial density is initially uniform everywhere. The oxygen concentration is a specified constant ($C_o = 21\%$) at the air-water interface (left side of the band) and zero everywhere else. The cells at open side of the capillary are exposed to high level of oxygen concentration and start swimming toward a lower level of oxygen concentration and some cells on the back are able to sense the favorable oxygen concentration; thus, the formation of the band begins from both sides, shown in Fig.2.5b. A steep gradient of oxygen forms, due to consumption of oxygen by the bacteria, shown in Fig.2.5c. In all simulations, the band formed at a location where oxygen concentration is below 1%, which agrees well with the experimental observations [57, 132, 84]. The cells density far to the right of the band remains unchanged since these cells do not sense the oxygen. The band location and the width are in good agreement with the experimental measurements, our simulation produced the remarkably close values 406 and 131 μm for band location and width, shown in Fig.2.5a.

2.6.2 Effect of bacterial density B_o

Band location and width depend on the initial bacteria density. The band formed further away from the meniscus with wider width when B_o was decreased by 50%, as shown in Fig.2.6, whereas it formed closer to the meniscus with narrower width when B_o was increased by 50%, as shown in Fig.2.7. Thus, the band position and width are decreasing function of B_o. Experiments with various bacterial densities (with higher and lower bacterial density) show similar trends. These experimental results are in good agreement with the model's prediction.

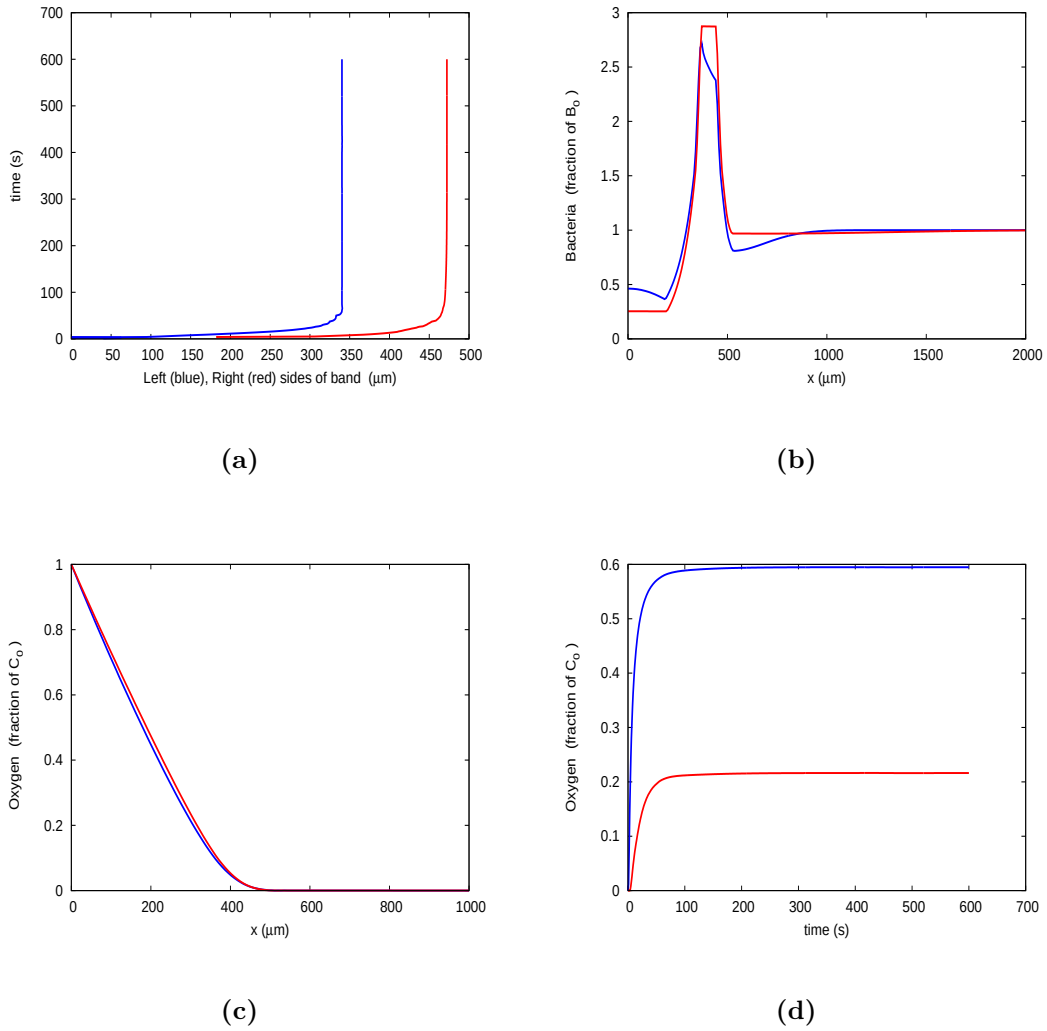

Figure 2.5: Aerotactic band formation with base case parameters. Parameters are shown in Table 2.1. (a) Band evolution in time: Left (blue) and Right (red) sides of the band. Band location and width are 406 μm and 131 μm, in excellent agreement with measured values. (b) Profiles of (normalized) bacteria concentration at time 50 s (blue) and 300 s (red). (c) Profiles of oxygen concentration at time 50 s (blue) and 300 s (red). (d) History of oxygen concentration in front of the band (blue) and in the band (red).

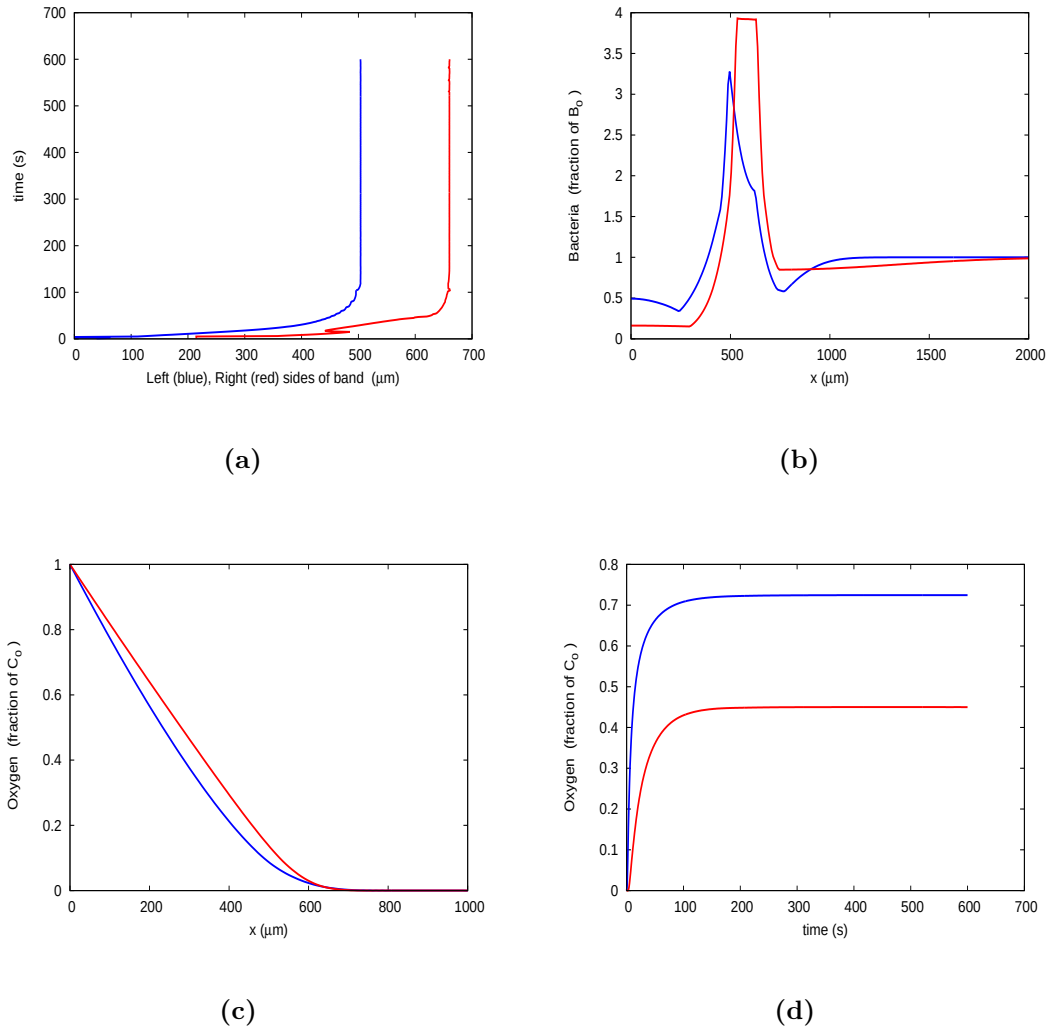

Figure 2.6: Aerotactic band formation with a lower cell density. Effect of decreasing B_o to 50% of base value: $B_o = 3 \times 10^8$ (a) Band evolution in time: Left (blue) and Right (red) sides of the band. Band location and width are 576 μm and 157 μm. (b) Profiles of (normalized) bacterial concentration at time 50 s (blue) and 300 s (red). (c) Profiles of oxygen concentration at time 50 s (blue) and 300 s (red). (d) History of oxygen concentration in front of the band (blue) and in the band (red)

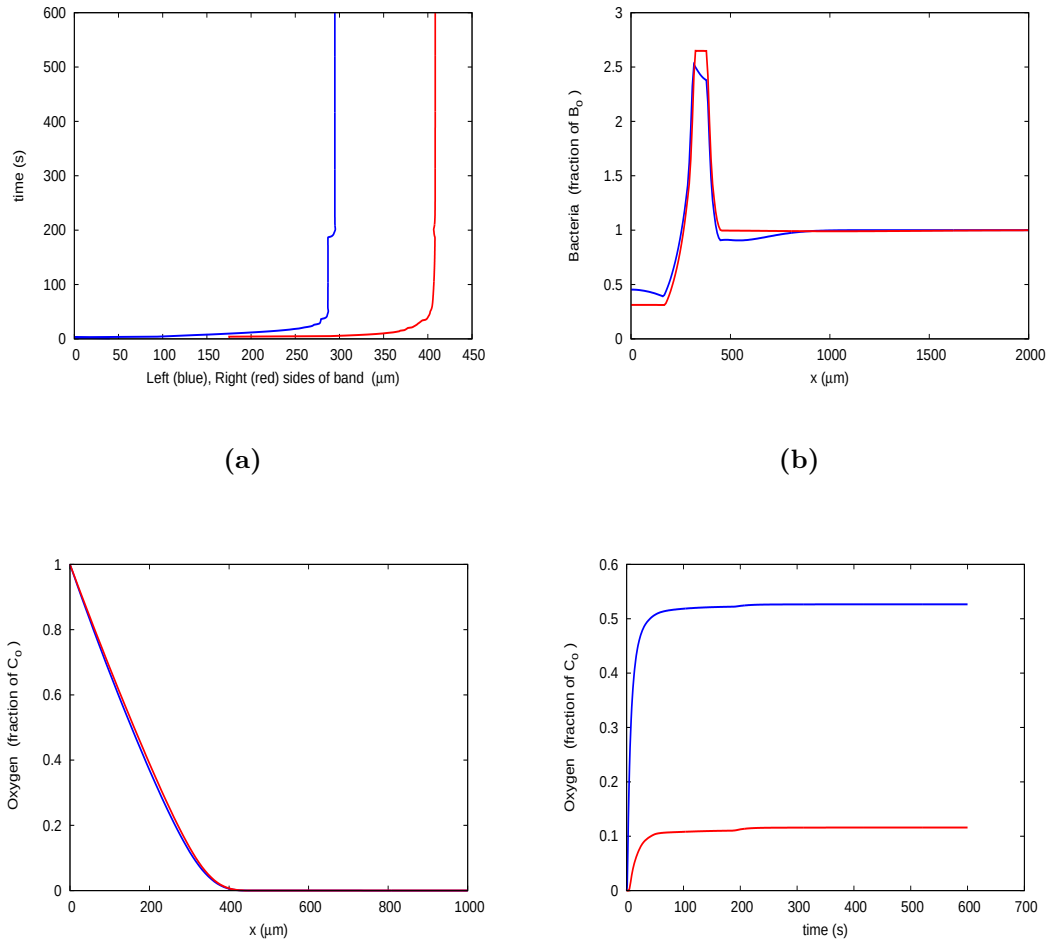

Figure 2.7: Aerotactic band formation with a higher cell density. Effect of increasing B_o by 50% of base value: $B_o = 10^9$. (a) Band evolution in time: Left (blue) and Right (red) sides of the band. Band location and width are 351 μm and 113 μm. (b) Profiles of (normalized) bacteria concentration at time 50 s (blue) and 300 s (red). (c) Profiles of oxygen concentration at time 50 s (blue) and 300 s (red). (d) History of oxygen concentration in front of the band (blue) and in the band (red).

2.6.3 Effect of Oxygen at the capillary opening C_o

Band location and width depend on the oxygen concentration at the meniscus opening. The band formed closer to the meniscus with almost the same width when C_o was decreased by 50%, as shown in Fig.2.8, whereas it formed further away from the meniscus with narrower width when C_o was increased by 50%, as shown in Fig.2.9. Thus, the band position is an increasing function of C_o since bacteria tend to move further away from the meniscus to escape unfavorable oxygen level.

2.6.4 Effect of consumption rate K

Band location and width depend on the oxygen consumption rate. To test further the effect of oxygen consumption rates on the aerotactic band formation, we altered the consumption rate and determined the effect on band formation in our simulations. The position and width of the aerotaxis band varied with oxygen consumption rates. The band was formed further away from the meniscus with wider width when K was decreased by 50%, as shown in Fig.2.10, whereas the band was formed closer to the meniscus with narrower width when K was increased by 50%, as shown in Fig.2.11. Thus, the model predicts the aerotaxis band position and width are decreasing functions of oxygen consumption rate.

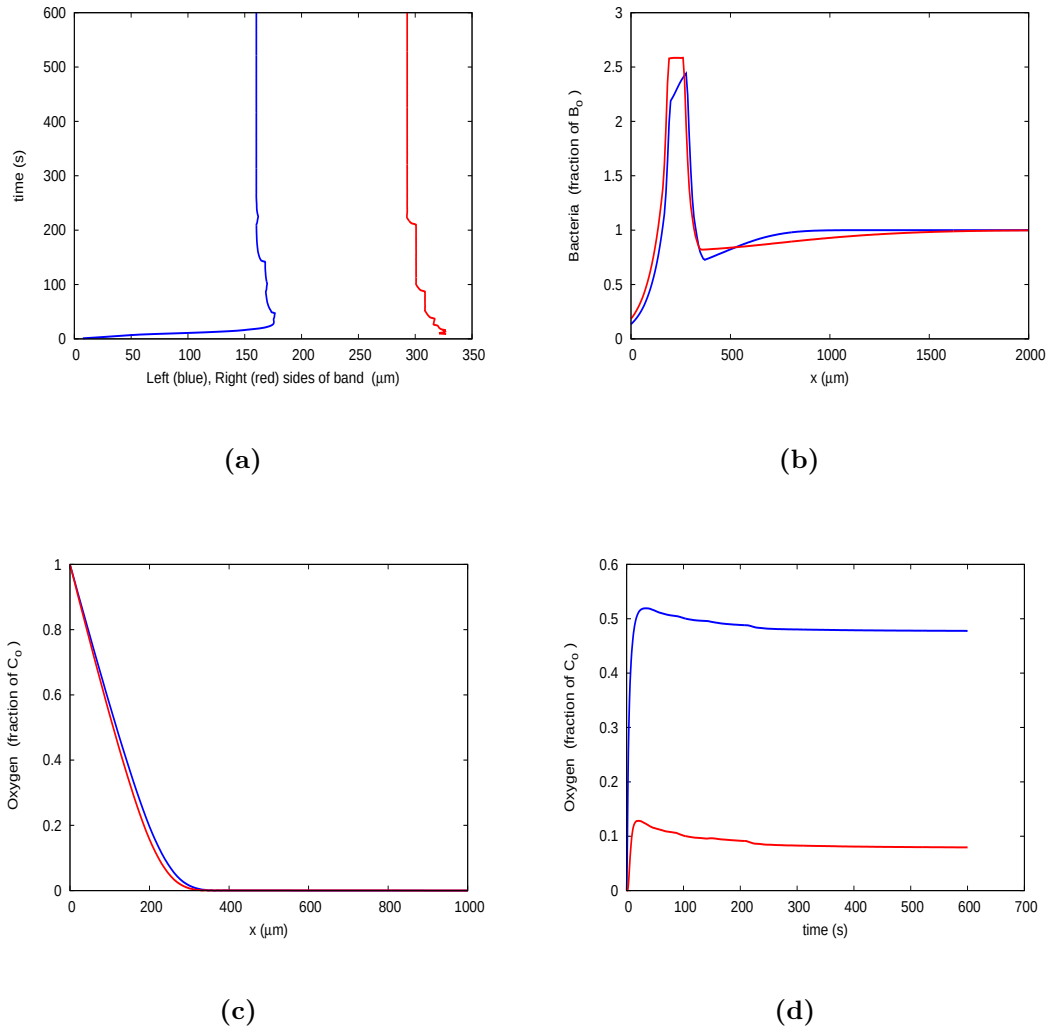

(a) **(b)**

(c) **(d)**

Figure 2.8: Aerotactic band formation with a lower oxygen concentration. Effect of lower Oxygen concentration at $x = 0$: $C_o = 10\%$. (a) Band evolution in time: Left (blue) and Right (red) sides of the band. Band location and width are 226 μm and 132 μm. (b) Profiles of (normalized) bacteria concentration at time 50 s (blue) and 300 s (red). (c) Profiles of oxygen concentration at time 50 s (blue) and 300 s (red). (d) History of oxygen concentration in front of the band (blue) and in the band (red) band.

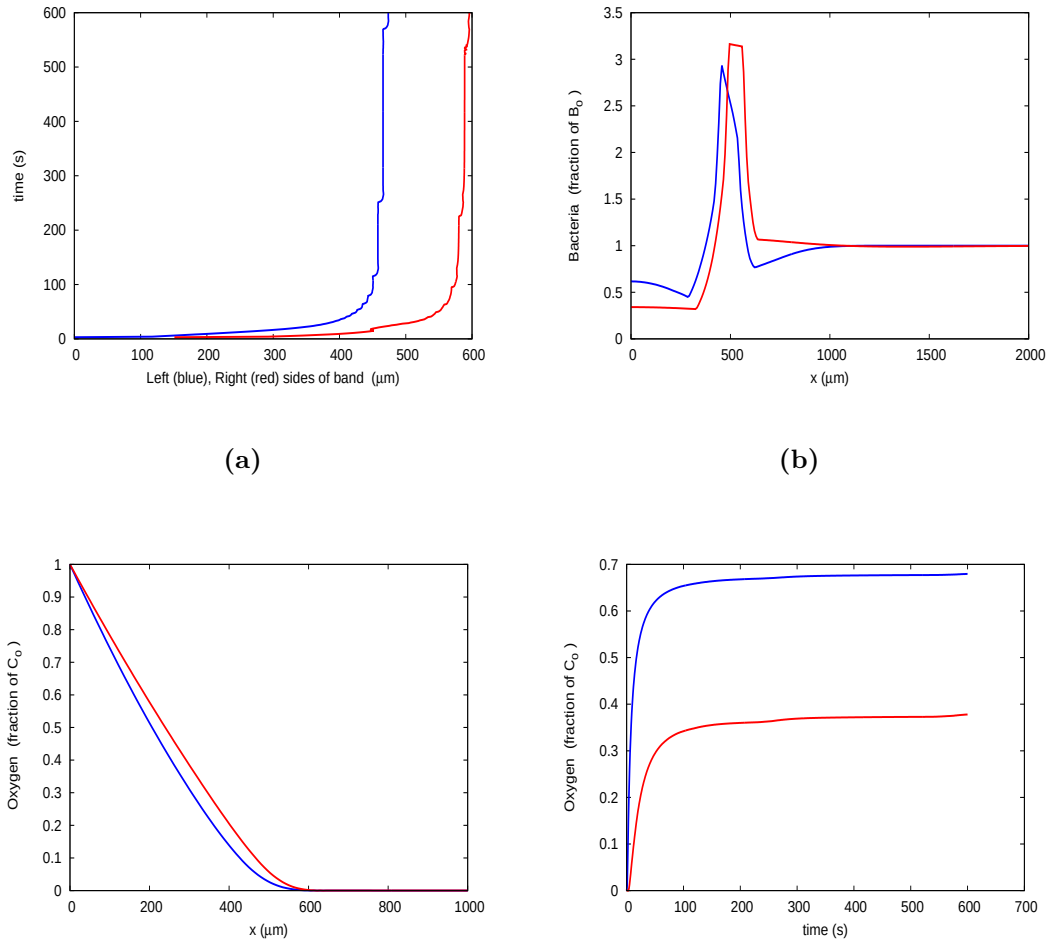

Figure 2.9: Aerotactic band formation with a higher oxygen concentration. Effect of higher Oxygen concentration at $x = 0$: $C_o = 40\%$. (a) Band evolution in time: Left (blue) and Right (red) sides of the band. Band location and width are 526 μm and 122 μm. (b) Profiles of (normalized) bacteria concentration at time 50 s (blue) and 300 s (red). (c) Profiles of oxygen concentration at time 50 s (blue) and 300 s (red), but they are almost same. (d) History of oxygen concentration in front of the band (blue) and in the band (red).

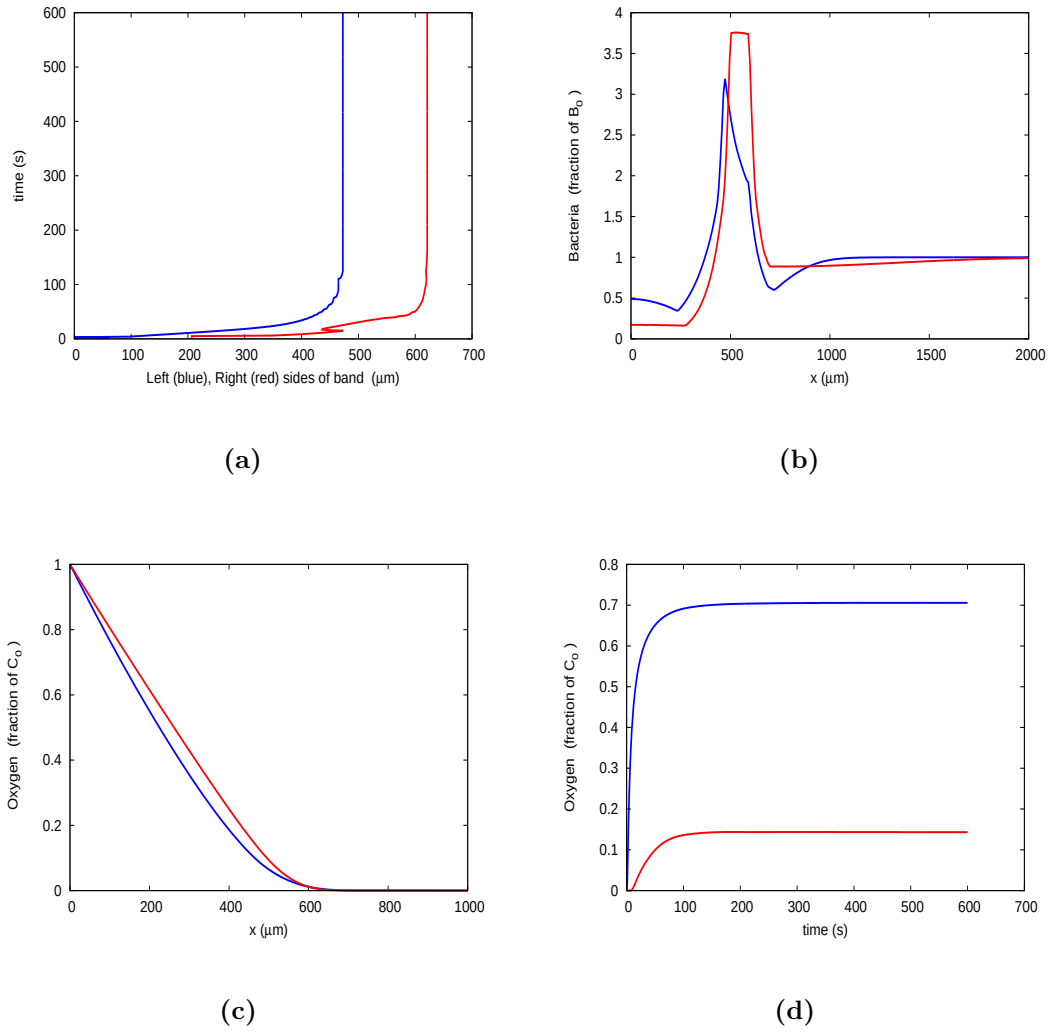

Figure 2.10: Aerotactic band formation with a lower oxygen consumption rate. Effect of decreasing oxygen consumption rate by 50% to $K = 2 \times 10^{-9}$. (a) Band evolution in time: Left (blue) and Right (red) sides of the band. Band location and width now are 546 μm and 148 μm. (b) Profiles of (normalized) bacteria concentration at time 50 s (blue) and 300 s (red). (c) Profiles of oxygen concentration at time 50 s (blue) and 300 s (red). (d) History of oxygen concentration in front of the band (blue) and in the band (red).

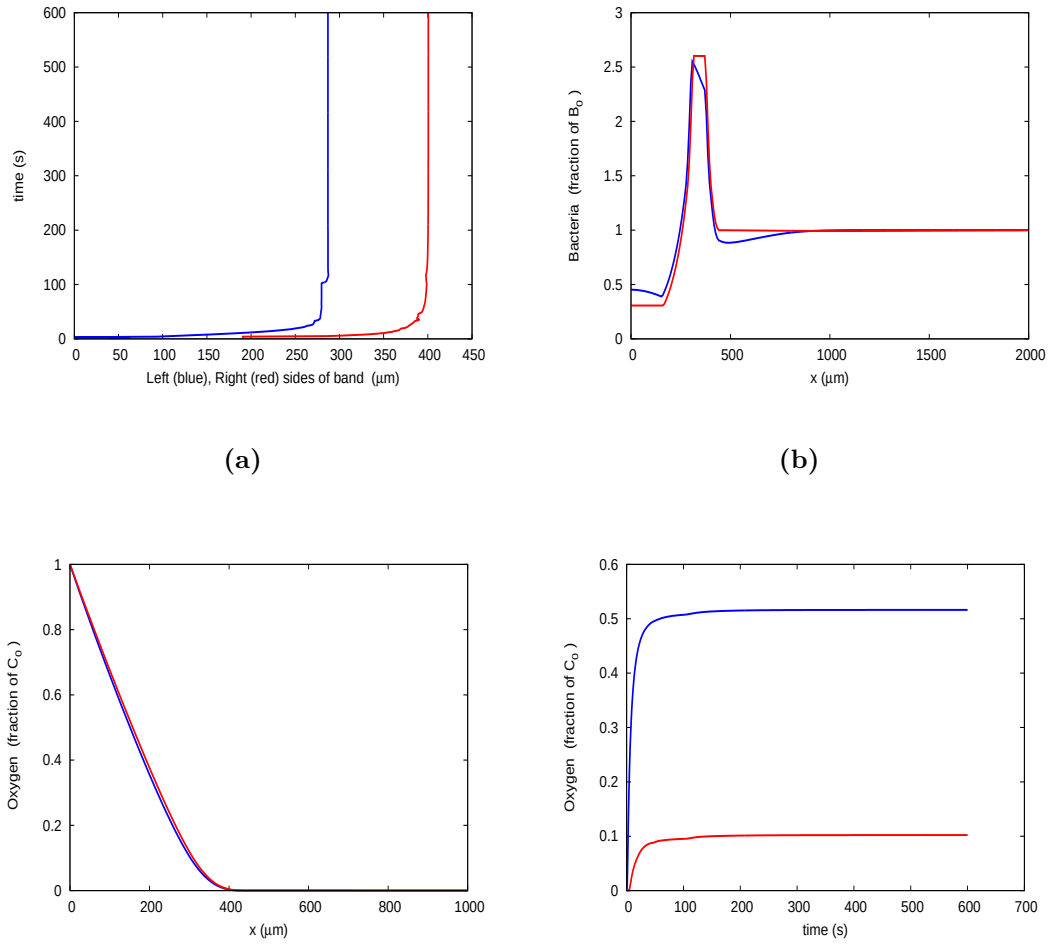

Figure 2.11: Aerotactic band formation with a higher oxygen consumption rate. Effect of increasing oxygen consumption rate by 50% to $K = 6 \times 10^{-9}$. (a) Band evolution in time: Left (blue) and Right (red) sides of the band. Band location and width are 343 μm and 113 μm. (b) Profiles of (normalized) bacteria concentration at time 50 s (blue) and 300 s (red). (c) Profiles of oxygen concentration at time 50 s (blue) and 300 s (red). (d) History of oxygen concentration in front of the band (blue) and in the band (red).

2.6.5 Effect of swimming speed v

Band location and width depend on the swimming speed. The band was formed closer to the meniscus with narrower width when v was decreased by 50%, as shown in Fig.2.12, whereas the band was formed further away from the meniscus with wider width when v was increased by 50%, as shown in Fig.2.13. Thus, the band position and width are a increasing function of the swimming speed.

2.6.6 Effect of the ratio F_{max}/F_{min} of reversal frequencies

Band location and width depend on the ratio of maximum and minimum reversal frequencies. The band formed closer to the meniscus with narrower width when the ratio was increased by reducing F_{min} by 50%, as shown in Fig.2.14, whereas it formed further away from the meniscus with wider width when the ratio was decreased by reducing F_{max} by 50%, as shown in Fig.2.15. Thus, the band position and width are decreasing functions of the ratio F_{max}/F_{min}.

2.6.7 Effect of the difference of detectable oxygen concentrations $C_{max} - C_{min}$

Band location and width depend on the difference between upper and lower detectable oxygen concentrations. The band was formed closer to the meniscus with wider width when C_{max} was increased by 50%, as shown in Fig.2.16, whereas the band was formed further away from the meniscus with narrower width when C_{max} was increased by 50%, as shown in Fig.2.17. Thus, the band position is an increasing function of the difference between C_{max} and C_{min}, but band width is a decreasing function of $C_{max} - C_{min}$.

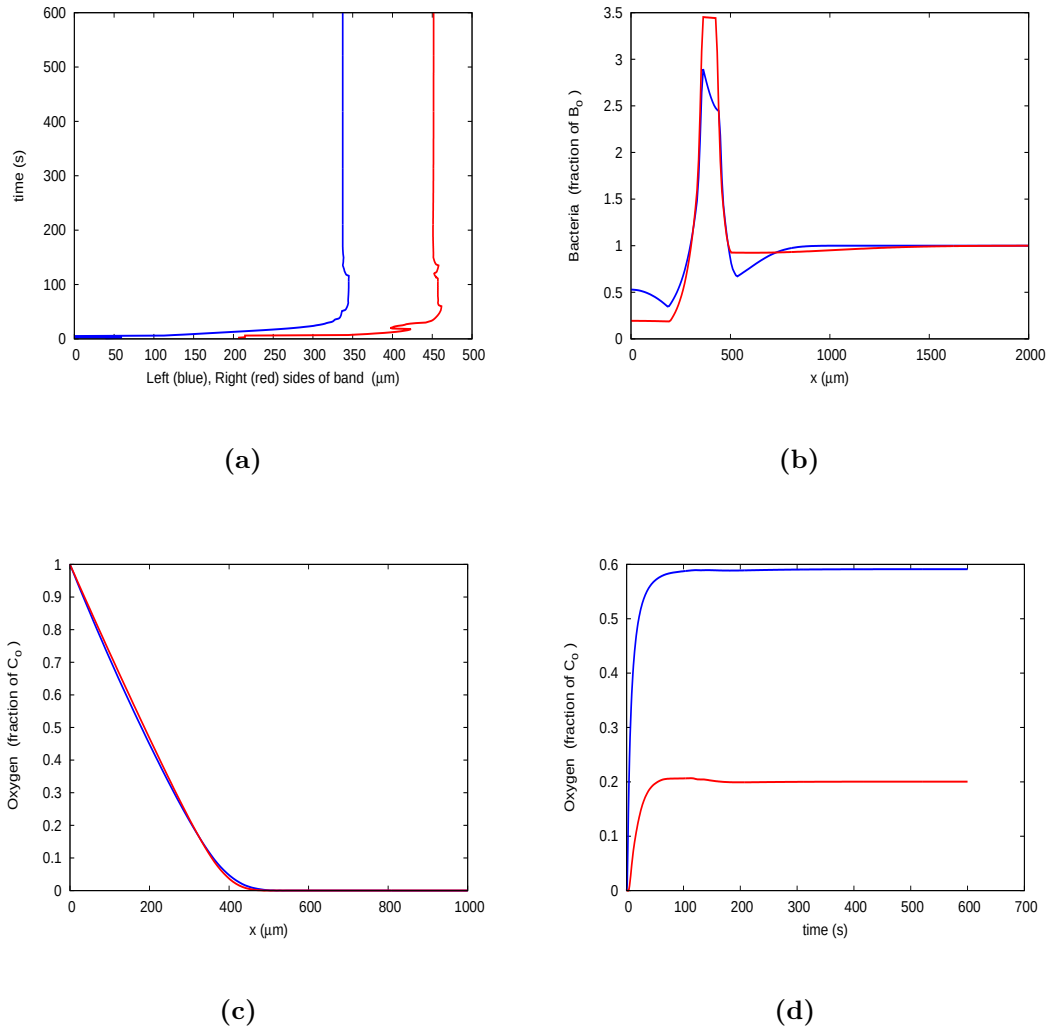

Figure 2.12: Aerotactic band formation with a lower swimming speed. Effect of decreasing speed to $v = 15\mu m/s$. (a) Band evolution in time: Left (blue) and xRight (red) sides of the band. Band location and width are 394 μm and 114 μm. (b) Profiles of (normalized) bacteria concentration at time 50 s (blue) and 300 s (red). (c) Profiles of oxygen concentration at time 50 s (blue) and 300 s (red). (d) History of oxygen concentration in front of the band (blue) and in the band (red).

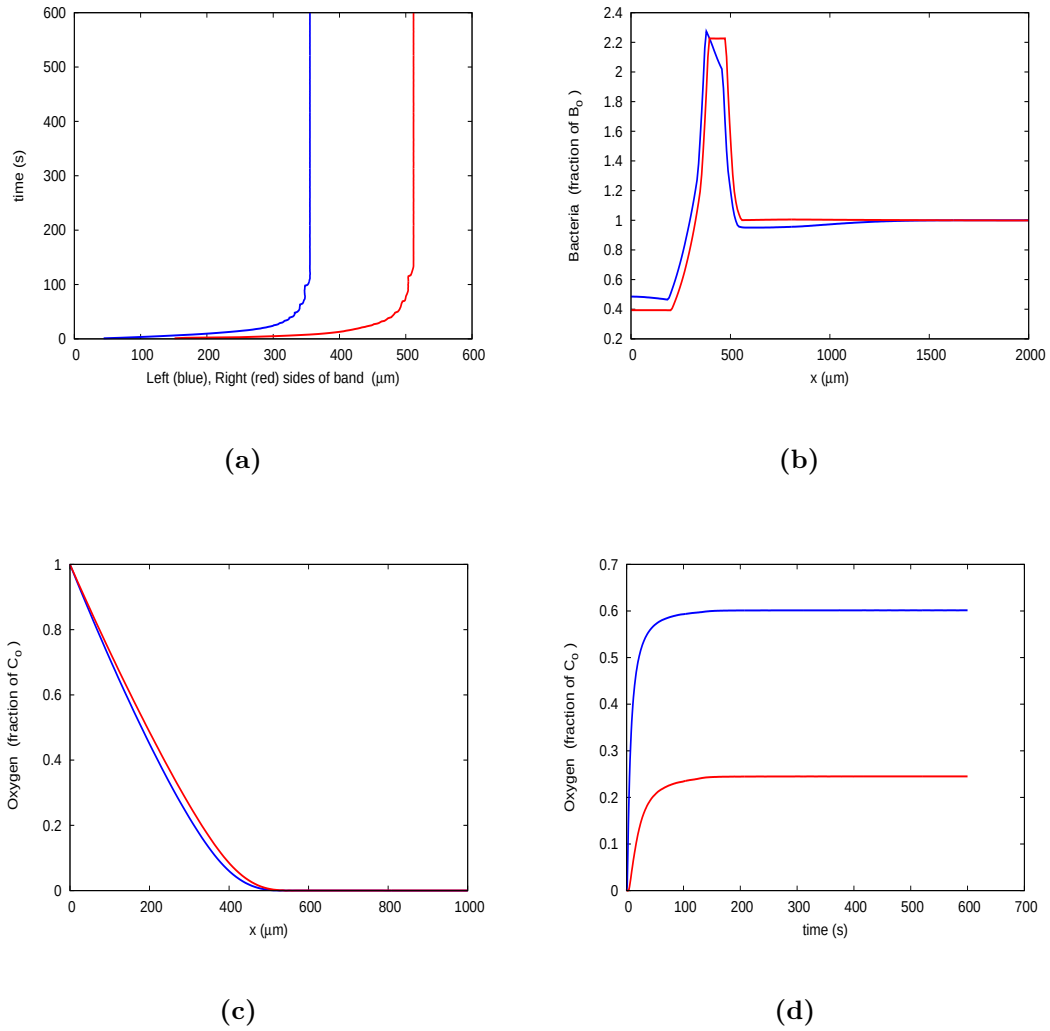

Figure 2.13: Aerotactic band formation with a higher swimming speed. Effect of increasing speed to $v = 35\mu m/s$. (a) Band evolution in time: Left (blue) and Right (red) sides of the band. Band location and width are 433 μm and 156 μm. (b) Profiles of (normalized) bacteria concentration at time 50 s (blue) and 300 s (red). (c) Profiles of oxygen concentration at time 50 s (blue) and 300 s (red). (d) History of oxygen concentration in front of the band (blue) and in the band (red).

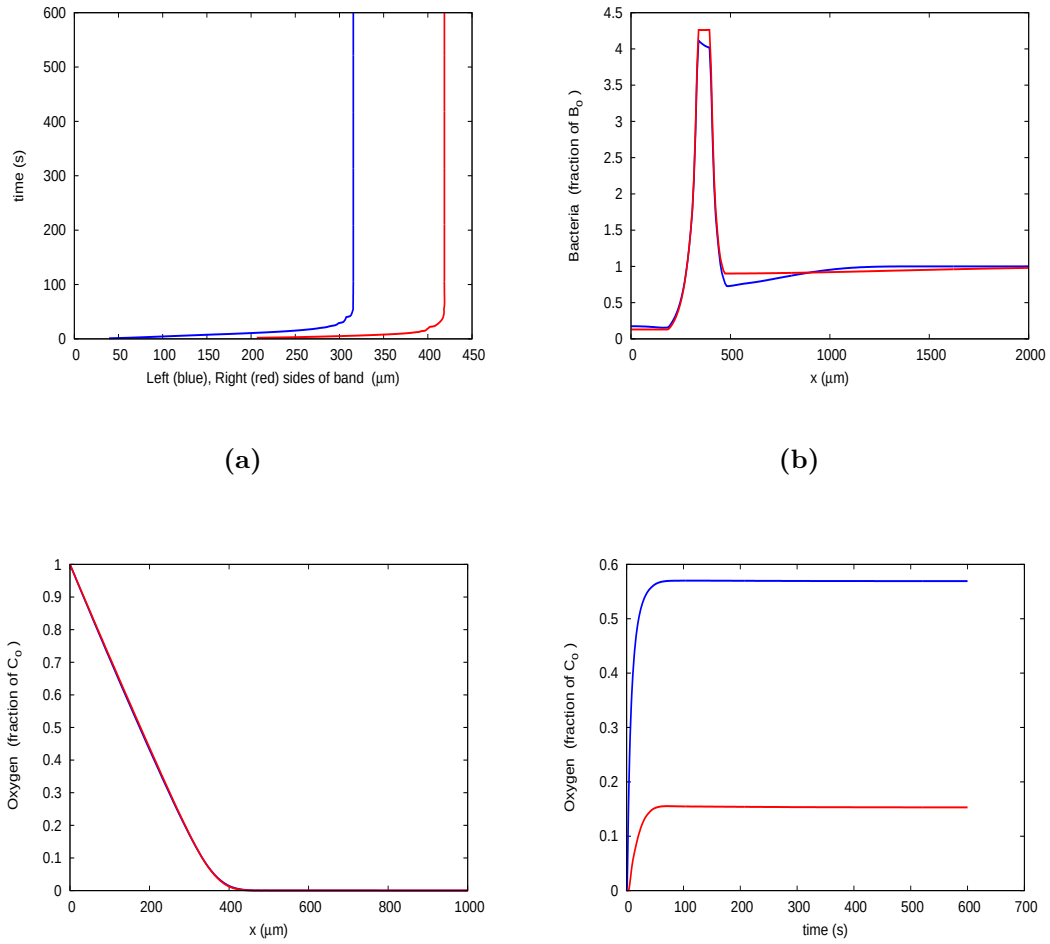

Figure 2.14: Aerotactic band formation with a lower minimum reversal frequency. Effect of decreasing F_{min} to $F_{min} = 0.15$. (a) Band evolution in time: Left (blue) and Right (red) sides of the band. Band location and width are 367 μm and 103 μm. (b) Profiles of (normalized) bacteria concentration at time 50 s (blue) and 300 s (red). (c) Profiles of oxygen concentration at time 50 s (blue) and 300 s (red), but they are almost same. (d) History of oxygen concentration in front of the band (blue) and in the band (red).

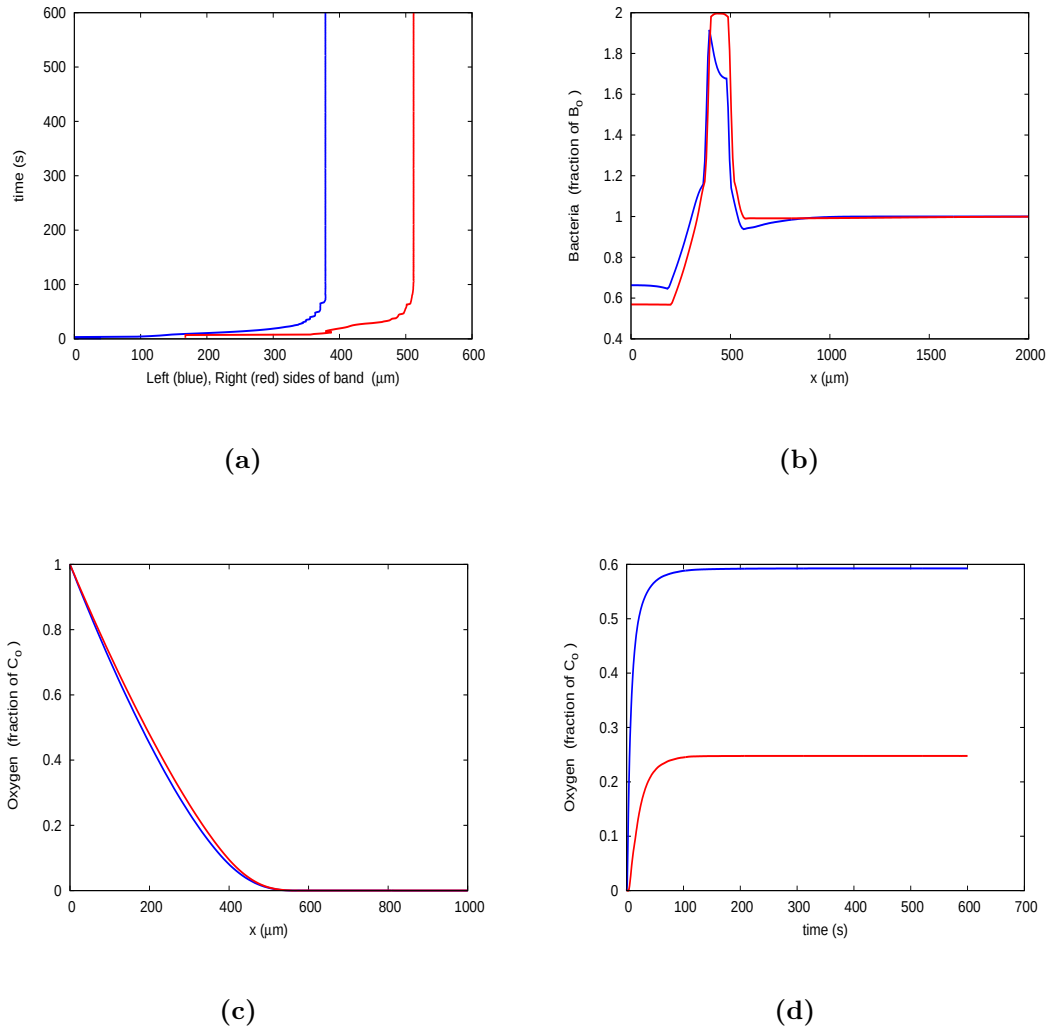

Figure 2.15: Aerotactic band formation with a lower maximum reversal frequency. Effect of decreasing F_{max} to $F_{max} = 0.45$, with $F_{min} = 0.35$. (a) Band evolution in time: Left (blue) and Right (red) sides of the band. Band location and width are 445 μm and 153 μm. (b) Profiles of (normalized) bacteria concentration at time 50 s (blue) and 300 s (red). (c) Profiles of oxygen concentration at time 50 s (blue) and 300 s (red), but they are almost same. (d) History of oxygen concentration in front of the band (blue) and in the band (red).

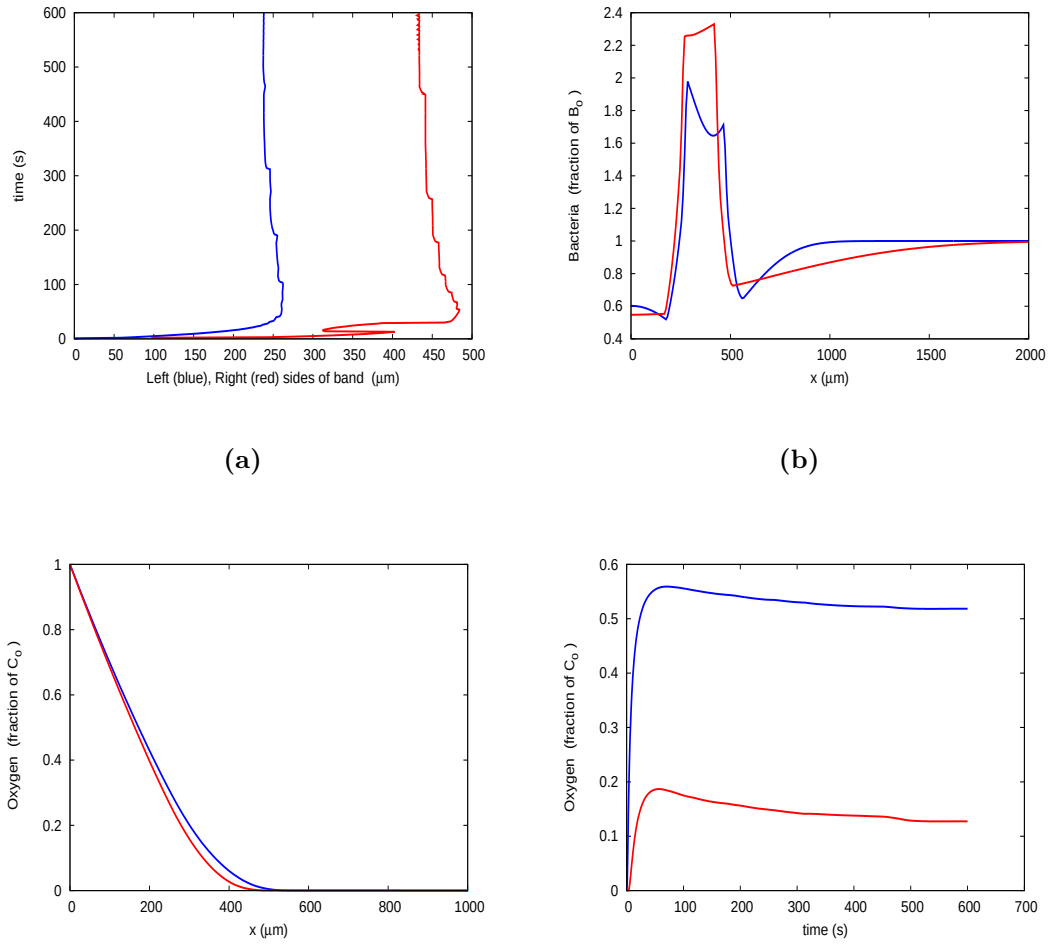

Figure 2.16: Aerotactic band formation with a higher upper detectable oxygen concentration. Effect of wider gap $C_{max} - C_{min}$, by increasing C_{max} to 5% (from 2%), keeping C_{min} at 0.3%. (a) Band evolution in time: Left (blue) and Right (red) sides of the band. Band location and width are 344 μm and 196 μm. (b) Profiles of (normalized) bacteria concentration at time 50 s (blue) and 300 s (red). (c) Profiles of oxygen concentration at time 50 s (blue) and 300 s (red). (d) History of oxygen concentration in front of the band (blue) and in the band (red).

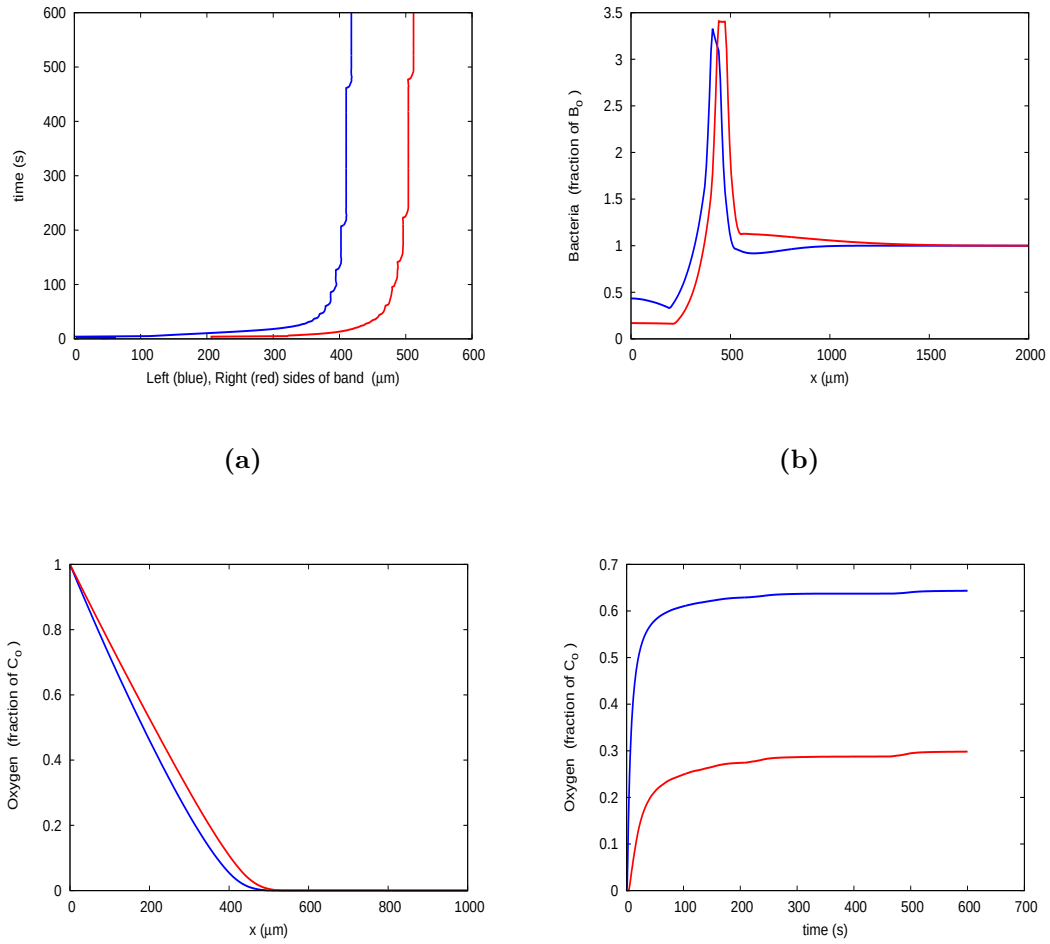

Figure 2.17: Aerotactic band formation with a lower upper detectable oxygen concentration. Effect of narrower gap $C_{max} - C_{min}$, by decreasing C_{max} to 1% (from 2%), keeping C_{min} at 0.3%. (a) Band evolution in time: Left (blue) and Right (red) sides of the band. Band location and width are 457 μm and 93 μm. (b) Profiles of (normalized) bacteria concentration at time 50 s (blue) and 300 s (red). (c) Profiles of oxygen concentration at time 50 s (blue) and 300 s (red). (d) History of oxygen concentration in front of the band (blue) and in the band (red).

2.7 Conclusions

The ability to navigate gradients of oxygen is key to regulate metabolic activities of bacteria with a range of lifestyles. It is thus not surprising to observe that aerotaxis is a widespread behavior in bacteria and Archaea [115].

Several mathematical models have be developed to recapitulate the movement of bacteria in oxygen gradients. The models developed for bacteria that track higher concentrations of oxygen such as *B. subtilis* [75] or which prefer lower oxygen concentrations such as *Desulfovibrio desulfiricans* [39] are not appropriate for *A. brasilense* because the aerotaxis strategies of these organisms are distinct. *B. subtilis* detects oxygen directly and navigates toward elevated oxygen concentrations while *D. desulfuricans* is a strict anaerobe that forms a band at the oxic-anoxic interface with the band being far less stable than that observed for *A. brasilense*.

When we attempted to use the previously developed model and parameters for *A. brasilense* aerotactic band formation [72] we were unable to produce a stable band, which is characteristic of the *A. brasilense* aerotaxis response [133, 4]. The model and parameters, along with experimental values, used here provide a robust model that captures all significant features of *A. brasilense* aerotaxis band formation.

In all the simulations, bacteria formed a stable aerotactic band in the range of $0 - 10\ \mu M$ oxygen. The location and width of the band agree well with those measured for microaerophilic *A. brasilense* cells in [133, 72, 84]. Our model estimates unknown parameters well, on the basis of which one can make testable predictions about the dynamics of the band. The numerical simulations explored the dependence of the aerotactic band location and width on various parameters, such as effects of cell density, oxygen concentration at the meniscus or oxygen consumption rate on the position and thickness of the aerotactic band. In addition to the experimental data validating at least some of these observations here, [9, 8] demonstrated that increasing the oxygen concentration available at the capillary opening delayed band formation, and led to an increase in the number of attracted bacteria to the band, i.e., the band became thicker over time. Our model also predicts that swimming speed should alter the position of the aerotaxis band in the gradient. While we used slightly

different growth conditions than those used here for modeling purposes, it has been shown in [83] that a mutant derivative of *A. brasilense* Sp7 altered in swimming speed ($\Delta cheY1$) was able to form an aerotaxis band with a significant delay relative to the wild type strain and the band formed closer to the meniscus and was noticeably thinner.

The tight aerotactic band formed by *A. brasilense* in gradients of oxygen depends on the abilty to sense oxygen as both an attractant and a repellent. *A. brasilense* senses very low or very high oxygen concentrations as repellents and motile cells navigate the gradients to stay away from these two strong repellents to position as a band at a location where oxygen is an attractant [133]. These opposing behaviors are captured in the model described here and by our experimental data indicating a very high probability of reversal in the swimming direction for cells within the band. In contrast to [72], we have not been able to observe any other behavior within the aerotaxis band, including no cell displaying significant straight runs. This discrepancy could perhaps explain the difference in the stability of the aerotaxis band that is captured well in our model but not in [72].

Chapter 3

Tracking software for free-swimming cells

3.1 Introduction

Chemotaxis is the process by which a cell alters its speed or frequency of turning in response to changes in the surrounding environment [68, 31]. Thus, chemotaxis helps motile bacteria to find the favorable environment for their metabolism and survival [3]. The swimming pattern displayed by flagellated bacteria varies with the flagellar arrangement, bacterial shape, and the mode of flagellar motor rotation. The overall resulting swimming pattern is assumed to be optimized for navigation under specific conditions and to influence dispersal and chemotaxis [113]. Most motile bacteria typically move in a sequence of approximately straight lines that are interrupted by turning events. Bacteria drive their swimming locomotion with the help of rotating flagella, which are attached to the cell body. Counterclockwise (CCW) rotation induces formation of a flagellar bundle that pushes the cell forward, known as "runs". On the other hand, clockwise (CW) rotation of one or more flagellar motor causes the flagella bundle to fly apart and it leads to reorintation of the cell, known as "tumbles"/"reversals" [123, 40]. The most extensively studied peritrichously flagellated *Escherichia coli* has a "run-and-tumble" swimming behavior [12]. On the other hand, the motile soil bacteria *Azospirillum brasilense* swim using a single polar flagellum that can only backtrack its trajectory when the motor reverses (to CW rotation), as seen in

Fig. 3.1, owing to low Reynolds number hydrodynamics [66], and also change its rotational speed (swimming speed) [132, 83].

The flagellar motor activity of bacteria is regulated by a **signal transduction pathway**, which integrates changes of enviromental chemical concentrations into a behavioral response [10, 6, 104]. The study of the signal transduction pathway and the flagellar motor activity requires monitoring bacterial locomotion and analysis of collective dynamics.

Single particle traking (SPT) using video microscopy is a powerful experimental tool to study a number of well-characterized phenotypes including chemotaxis, biofilm formation, intracellular protein traffcking and cell migration [103, 69]. SPT methods extract the indvidual particle trajectories from time-lapse frames and provide useful information about both individual particle and collective behavior of particles. A large number of trajectories have to be analyzed to ensure that any inferences drawn from the observations are statistically representative of the particles. It would be very difficult and tedious to analyze a large number of particles by a manual analysis (eye). Several commercial tracking software exist. However, there are some limitations of using these software, including their high cost, inability of tracking more than a hundred cells or so, hardware requirements, being not user-friendly or a minimal provided information of motility parameters. Thus, an automated tracking software suit for free swimming bacteria was implemented in order to track a large number of bacteria and analyze the resulting trajectories.

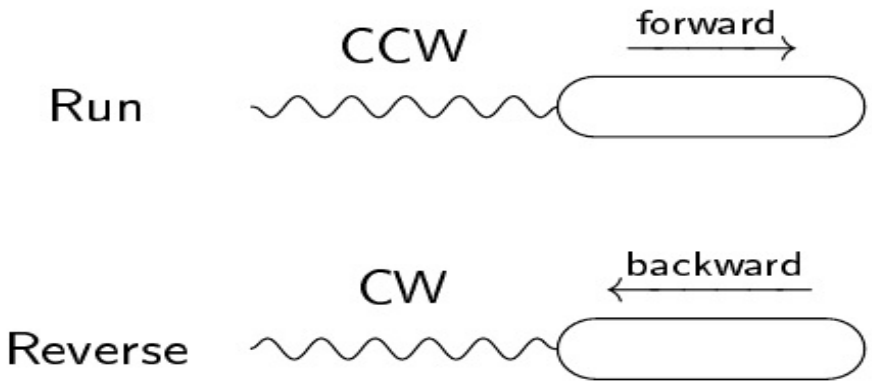

Figure 3.1: Movement strategies of *Azospirillum brasilense*. Counterclockwise rotation of the flagellum induces forward move, whereas clokwise rotation induces backward move.

The tracking software presented in this chapter obtains dynamic information of free swimming cells from a recorded real-time digital video. It simultaneously reconstructs trajectories of cell bodies by matching their centroid (center of mass) from a sequence of images without limitations on the sequence length and without lowering the image visual field (the focal plane). Then, it automatically generates statistical analysis for each trajectory, and then of all trajectories, which includes run average speed, total average speed, average run time, average reversal time, reversal frequency, turning angle, mean squared displacement and the distributions of reversals, speeds, runs time and pauses. The statistics from a large data set provides quantitative information of the swimming behavior of bacterial population in response to environmental cues.

3.2 Experimental setup and imaging

Bacterial cell culture was prepared as follows: stocks from -80° were streaked on a minimal medium (MMAB) - Nitrogen (N) + carbon source (C) plate. Single colony from the freshly streaked plate was inoculated in liquid MMAB+N+C media. Culture was re-inoculated at least once more until 0.6 OD before recording. The mid log phase culture was then harvested and washed in Che buffer 3 times @ 3000 rpm for 3 min and waited for at least 30 minutes before recording. All recordings were completed within 2 hours of washing. The density of bacteria was kept low to avoid mistmatching association in the tracking

All recordings were done using a Concavity Microscope Slides from Thermo Fisher scientific (cat no- 1518006). These slides have a concave depression with 5-18mm diameter well and are $0.6-0.8$ mm deep, as shown in Fig.3.2. A 10 μl drop of culture in Che buffer was placed in the middle of the depression well and covered with coverslip (Corning, #1 Cover Glass, cat no 2975-223). The coverslip in addition to the necessary contrast also provided a setting where there was little or no perturbation due to air or fluid current. Recording was done using Nikon E200 upright microscope equipped with 20$\times$ (Nikon, Plan Fluor ELWD, $\times$ 20, NA 0.45). The microscope was focused in the middle of the drop such that the focal plane was at least 300-400 μM away from the surface owing to the depth of the well in

the slide. All recording was done using Leica MC120HD at 30fps at resolution 1920×1280 pixels.

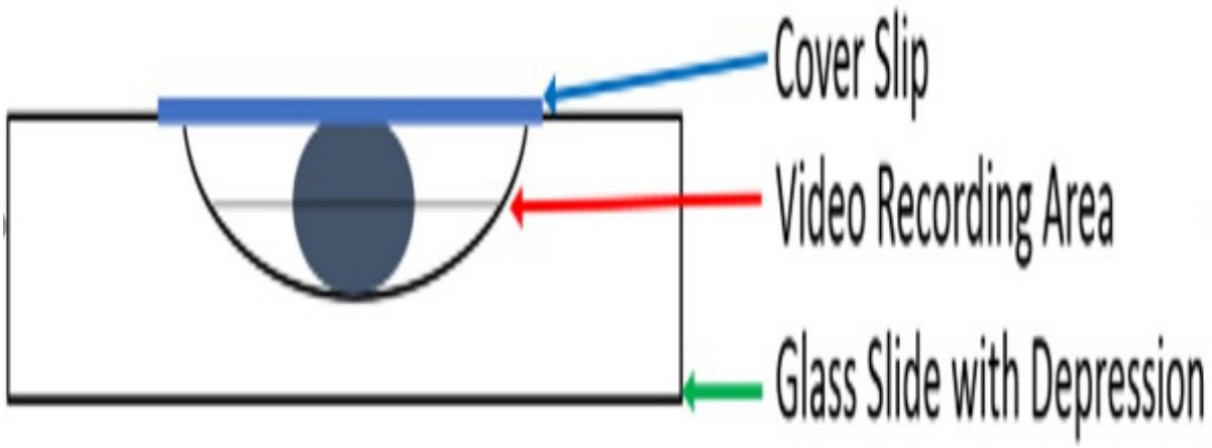

Figure 3.2: Experimental setup for linear channel time lapse microscopy.

3.3 Image processing and cell tracking

In this section, we go step-by-step through the cell tracking algorithm. We focus on how images are processed to identify the cells that will be tracked. To reconstruct the cell trajectories, each image sequence is processed using custom code written in MATLAB (version R2017a, The MathWorks, USA).

3.3.1 Pre-processing

First, a lowpass filter is constructed by convolving the original image with a gaussian kernel with parameters $\mu = 5$ and $\sigma = 2$, and a highpass filter is constructed by convolving the original image with a boxcar function with 15 x 15 averaging (mean) kernel, described in detail in [28]. Next, a bandpass filter is obtained by subtracting a highpass filter from a lowpass filter. This bandpass filter is then applied to all frames in order to remove noise in the frames due to uneven illumination (non-uniform background intensity, as shown in Fig.3.3a) prior to locating the cells. From the filtered image sequence, a background image, as shown in Fig.3.3b, is constructed to remove unwanted background features and noise. This background image is obtained by calculating the mean pixel intensities of frames over

the image sequence. The background image is then subtracted from each image in the image sequence to exclude nonmoving cells. After a 3 x 3 median filter is applied to background-free images, cells in each image are segmented by an automatically selected intensity threshold, which depends on the brightest pixel in the image. The positions of all cells in all images are determined by calculating the centroid of the brighest pixels in frames.

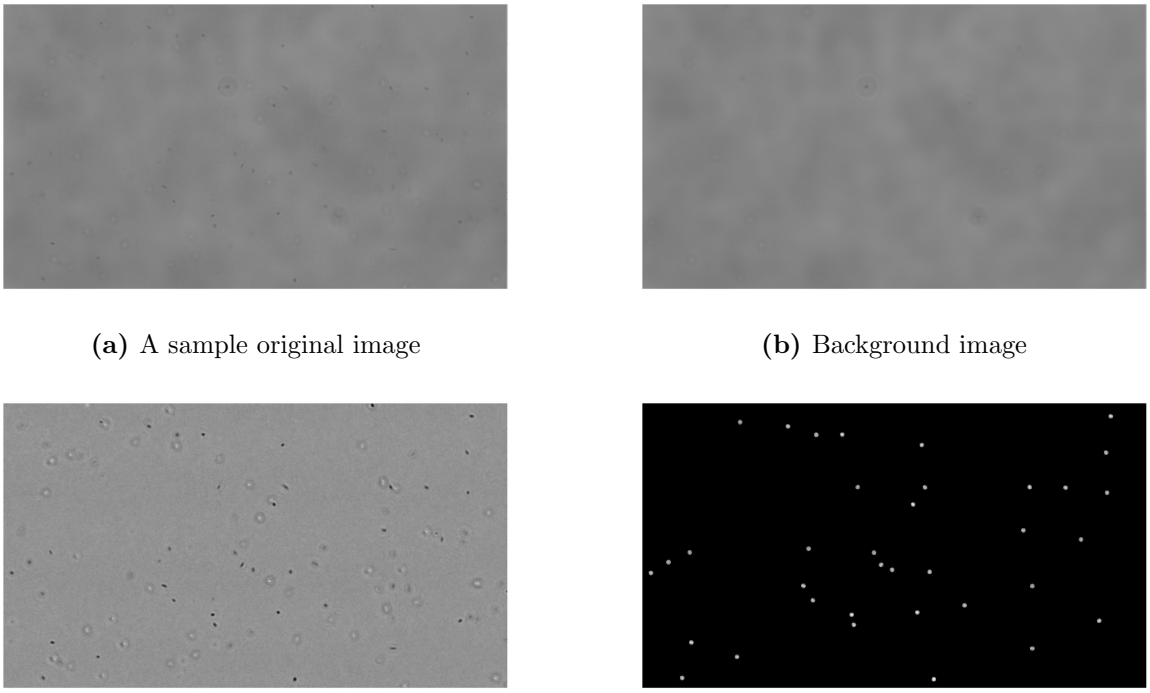

(a) A sample original image

(b) Background image

(c) Background free image

(d) Segmented image

Figure 3.3: Images in pre-processing step of image processing. Cells out of the focal plane appear as circles with a bright central spot, as shown in (c). In the segmented image, (d), cell locations are indicated with white dots.

3.3.2 Cell tracking

Locating cells in each frame is the first step of cell tracking. To identify the same cell in neighboring frames, so that a trajectory can be formed as a function of time, a MATLAB version of the particle tracking algorithm by Crocker and Grier [28] is used on the two-dimensional data to link the positions of cells in order to form trajectories in time and space. This algorithm is based on nearest neighbor approach in which it links locations at frames

i and $i+1$ to the same cell based on proximity. Among all possible assignments, as shown in Fig. 3.4b, the algorithm considers the assignments that have shorther distance that pre-specified radius for maximum search displacement parameter (MD), as shown in Fig. 3.4c, and chooses the combination that yields minimum displacement for the cell, as shown in Fig. 3.4d. The traking performance is affected by the choice of MD. Thus, MD has to be choosen very carefully. It must be small enough to discard false connections, but large enough to detect all possible connections that represent real cell displacements [71]. Each frame may contain a different number of cells, since cells can enter and leave the focal plane at any time.

3.3.3 Post-processing

In every experiment, we observed that some cells never moved or they collided with other cells. In order to remove these inappropriate trajectories (such as floating and dead cells) from the analysis, we use the following filters:

- The trajectories with an average speed of less than 15 $\mu m/s$ are disregarded.
- The trajectories with a tracked duration greater than 2 s are considered for the analysis.
- The trajectories in the case of bacterial collision are discarded since the trajectories have been modified by a physical impact. This ensures that hydrodynamic interactions between the cells do not play a role in the analysis.
- The trajectories with highest median curvature are removed. This curvature filter removes trajectories where the cells reverse for very long times.

Furthermore, the first three and the last three frames of each recorded trajectory are disregarded in order to avoid over-estimating swimming parameters (such as reversal frequency) since the most common way for cells to enter or leave the focal plane is by changing their direction. The resulting trajectories are smoothed with a running average over three frames for further analysis.

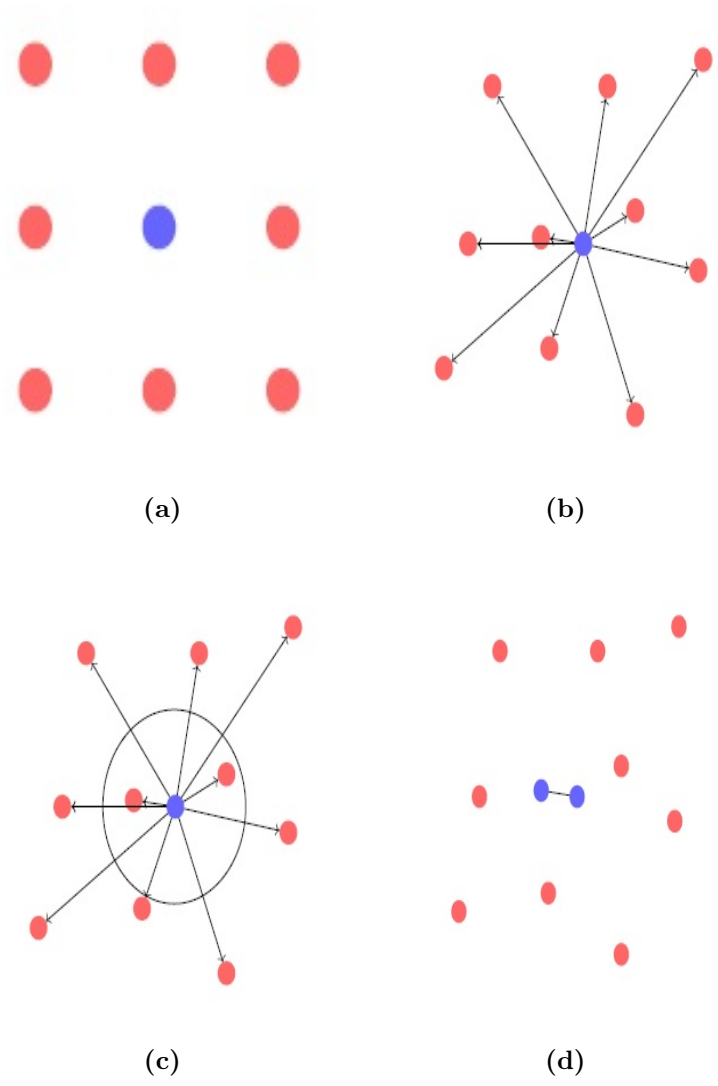

Figure 3.4: Nearest neighbor link assignment. The location of cells in each frame are indicated by red circles. This schematic drawing illustrates traking of a cell (blue circle). (a) Locations of cells at frame i. (b) Locations of cells at frame $i + 1$. Arrows indicate all possible assignments of blue circle (the location of the cell being traked from prior frame). (c) The algorithm only considers the links that are shorter than specified maximum search radius displacement. (d) A trajectory is formed by choosing the nearest location.

3.3.4 Trajectory Plotting

Our software can produce Matlab plots of individual trajectories, displaying different types of motion in different colors, e.g. blue for runs, green for pauses, red for turn events, as seen in Fig.3.6.

3.4 Analysis of cell trajectories

3.4.1 Movement detection of two-dimensional trajectories

Cell motion, characterized by swimming velocity and angular velocity, as defined in Fig.3.5, is described in this section. Trajectories after post-processing are considered for the analysis. From a large data set of swimming trajectories of bacteria, several quantities are computed, including average run speed, maximum speed, minimum speed, average run time, frequency of reversals, average angle of reversal, pause frequency, average pause time, and mean square displacement of bacteria. It has been reported ([70, 116, 89]), and we observe visually, that during the reversal state the bacterium reduces its speed and reorients rapidly in a new direction. Thus, reversal events are identified by rapid changes in the angular velocity and/or speed.

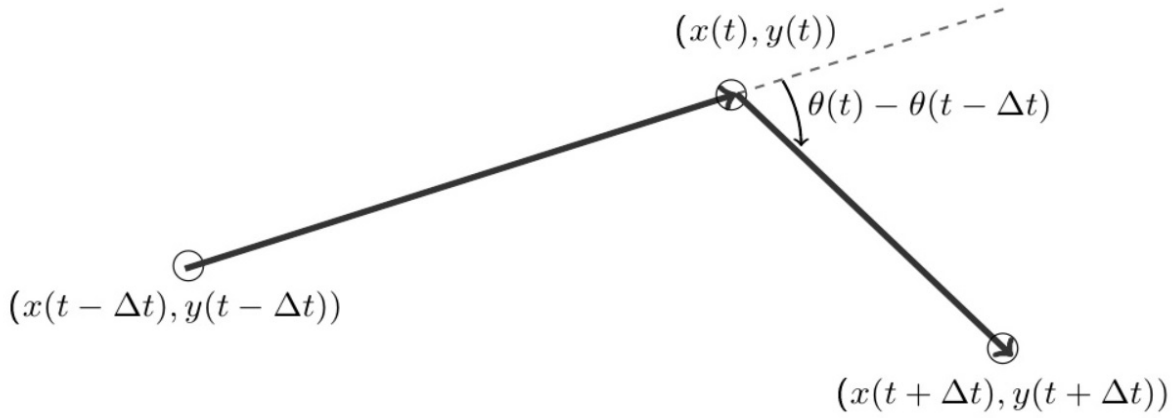

Figure 3.5: Schematic of bacterial turning event. An open circle represents the center of the cell body. The velocity at time t is determined from the positions of the cell body at times t and $t - \Delta t$. The angular velocity at time t is determined from the cell orientation at times t and $t - \Delta t$. The cell moves in direction $\theta(t)$ at time t and moves in the new direction $\theta(t + \Delta t)$ at time $t + \Delta t$. Thus, the turning angle at time t becomes $\theta(t) - \theta(t - \Delta t)$.

Speed and acceleration

A cell trajectory is represented by a two-dimensional position vector $r(t) = (x(t), y(t))$ of the centroid of the cell at time t. Velocity of cell movement is measured as the distance moved between consecutive frames, divided by the time elapsed in between. Thus, cell speed is calculated by

$$\nu(t) = \frac{\Delta r}{\Delta t} = \frac{r(t) - r(t - \Delta t)}{\Delta t} \tag{3.1}$$

where $\Delta r = \sqrt{(x(t) - x(t - \Delta t))^2 + (y(t) - y(t - \Delta t))^2}$ and Δt $(= 0.033s)$ is the time between frames (at frame rate 30 fps).

The acceleration of the cell is determined by the rate of change in the swimming speed between two time steps, calculated as

$$a(t) = \frac{\Delta v}{\Delta t} = \frac{\nu(t) - \nu(t - \Delta t)}{\Delta t}. \tag{3.2}$$

Angular velocity

The orientation $\theta \in [0°, 360°]$ of each cell at time t is given by

$$\theta(t) = \frac{180}{\pi} arctan\left(\frac{\Delta y(t)}{\Delta x(t)}\right), \tag{3.3}$$

where $\Delta x(t) = x(t) - x(t - \Delta t)$ and $\Delta y(t) = y(t) - y(t - \Delta t)$.

The angular velocity is determined as the rate of change of angular displacement between two time steps

$$\omega(t) = \frac{\theta(t) - \theta(t - \Delta t)}{\Delta t}. \tag{3.4}$$

Mean square displacement

Mean square displacement (MSD) is used to measure how much cells displace or explore, on average, in a given interval of time [120, 88]. It is calculated after cell trajectories have been formed. The MSD is determined as a function of time lag, $\tau = n\Delta t$, where Δt is the time between frames and n is the number of time intervals. MSD is calculated by taking average over the square displacements for all possible time lags of all cells (trajectories) in the data.

Square displacements between frames can be calculated using x and y coordinate data from the cell trajectories. The MSD for the time lag n is determined by the formula

$$MSD(\tau) =< \Delta r^2(\tau) >= \frac{1}{N-n} \sum_{i=1}^{N-n} (x_{i+n} - x_i)^2 + (y_{i+n} - y_i)^2, \tag{3.5}$$

where $< \cdot >$ denotes the ensemble average. The formula uses all available displacements of a given duration $\tau = n\Delta t$. N is the maximum number of connections of the local positions of a cell trajectory that has N+1 data points. The ensemble MSD was considered for the analysis, where data points for longer lag times ($\tau > 6$ s) were discarded. The advantage of this formula is that it uses the maximum number of overlapping displacements of time duration τ, which results in averaged MSD values [127].

As time lag increases, large fluctuations (deviations) can be observed in MSD due to the fact that in the averaging, $N - n$ decreases. This suggest that an ensemble averaging should be considered in order to eliminate the influence of fluctuations.

Diffusion coefficient

Bacterial diffusivity D is an essential parameter for measuring the chemotactic potential of bacteria [129, 24]. The diffusion coefficient is calculated via the Einstein relation from the mean square displacement curve:

$$MSD(\tau) = 2mD\tau, \tag{3.6}$$

where $MSD(\tau)$ is the mean square displacement, τ is the observation time over which the displacement occurred, and m is the dimensionality of the diffusion process (here $m = 2$).

The mean squared displacement is used to determine whether cells are spreading only due to diffusion, or if another force (such as advection) contributes to their movement. The MSD curve can be fitted to a power law with an exponent λ as $MSD(\tau) \sim \tau^{\lambda}$. The value of λ is a key parameter. There are five possible cases that can be considered depending on the value of λ [27].

1. $\lambda = 0$: the process is stationary, no movement.

2. $0 < \lambda < 1$: this is known as *sub-diffusion*.

3. $\lambda = 1$: this is a standard diffusive movement (random walk). Thus, the linear relationship between the MSD and time t is used to determine the diffusion constant D by some fitting method, such as standard least-square fitting approach.

4. $1 < \lambda < 2$: this is known as *super-diffusion*. The MSD increases faster than in typical diffusion. This type of movement is also known as *Levy walk*.

5. $\lambda = 2$: the movement is known as *balistic motion*. The ballistic regime is observed graphically when the MSD has a parabolic dependence with time lags. In this case, the bacterium effectively moves in a straight line away from the origin with no reversals or tumbles.

Mean square angular displacement

The mean square angular displacement (MSAD) is calculated in order to determine the rotational diffusion coeeficient, labeled by D_r.

$$MSAD(\tau) = < \Delta\theta^2(\tau) > = \frac{1}{N-n} \sum_{i=1}^{N-n} (\theta_{i+n} - \theta_i)^2 \,. \tag{3.7}$$

where the formula uses all available displacements of a given duration $\tau = n\Delta t$. N is the maximum number of connections of the local positions of a cell trajectory that has N+1 data points. The ensemble MSAD was considered for the analysis, where data points for longer lag times ($\tau > 2$ s) were discarded.

3.4.2 Identifying turn events

To identify abrupt changes in speed, the local minimum of the instantaneous velocity is first detected. The time where a local minima was achieved is denoted by t_{min}. The location of two closest local maxima immediately before and after t_{min} are denoted respectively by t_1

and t_2. The relative change in speed is given as

$$\frac{\Delta\nu}{\nu(t_{min})}, \tag{3.8}$$

where the depth of minimum is given by

$$\Delta\nu = \max\{\nu(t_1) - \nu(t_{min}),\ \nu(t_2) - \nu(t_{min})\}.$$

If the relative change of velocity is sufficiently large: $\frac{\Delta\nu}{\nu(t_{min})} > 3.5$, it is considered that a turn event occured during the time interval around t_{min}, provided

$$\nu(t) \leq \nu(t_{min}) + 0.2\Delta\nu. \tag{3.9}$$

To identify abrupt changes in angular velocity, the local maximum in the absolute value of the angular velocity is detected. The time where a local maximum is achieved is denoted by t_{max}. The location of two closest local minima immediately before and after t_{max} are denoted respectively by t_1 and t_2. If the total change in direction over the interval $[t_1, t_2]$ was sufficiently larger than a threshold, which depends on the rotational diffusivity ($D_r = 0.2\ \frac{rad^2}{s}$), i.e. if

$$\Delta\theta > 7\sqrt{D_r(t_2 - t_1)}, \tag{3.10}$$

then it is considered that the bacterium is undergoing direction change during the time intervals around t_{max}, provided the angular speed $\omega(t)$ satisfies the following condition

$$|\omega(t_{max})| - |\omega(t)| \leq 0.7\,\Delta\omega, \tag{3.11}$$

where the depth of maximum is given by

$$\Delta\omega = \max\{|\omega(t_{max})| - |\omega(t_1)|,\ |\omega(t_{max})| - |\omega(t_2)|\}.$$

The parameters used in image processing, cell tracking, and analysis have a significant effect on the tracking quality. The parameters were chosen such that the detection of reversals or pauses were correct by visual inspection.

3.5 Results

In this section, we present results from analysis of a large data set of experimentally recorded swimming trajectories of wild-type and of several mutant strains of *A. brasilense*. Trajectories of 1360 cells were detected by our video processing software, some were discarded, and the remaining 1317 were analyzed.

3.5.1 Swimming patterns of *A. brasilense*

A. brasilense exhibits multiple swimming patterns, which we labeled **run-reverse**, **run-reverse-flick**, and **run-pause-run**. A **pause** is defined as a sudden decrease in the speed to nearly 0 $\mu m/s$, as shown in Fig.3.6b. During this pause phase, the flagellar motor stops rotating for a short time before it resumes the motion [91]. It was reported that one purpose of the pause phase is to enable the cells to change their direction of swimming. It is suggested that pausing is a result of incomplete reversal event [33]. Thus, pause phase is needed for some species to reorient their swimming direction by possibly Brownian motion or rotational diffusion [116, 89]. *Rhodobacter sphaeroides* cells cannot reverse their direction of rotation. Pausing allows the cell body to reorient and change its swimming direction [47]. The pause phase in this swimming pattern allows the cell to turn at a large angle. However, not every turning event is associated with a speed change [52]. A **reversal** event is associated with an angular change of $\sim 180°$, whereas a **flick** is identified with an angular change of $\sim 90°$. An example of a cell trajectory displaying several turning events can be seen in Fig.3.6a. The corresponding swimming speed and absolute value of angular velocity are shown as functions of time in Fig.3.6b. The sudden jumps in swimming speed (pauses) and sharp peaks in the angular velocity confirms that the bacterium reduces its velocity and reorients rapidly in a new direction. Thus, variations in speed and orientation angle are strongly coupled to each other during a turning event. The pause phase in this swimming pattern allows the cell to

turn at a large angle. However, not every turning event is associated with a speed change [52].

In *run-reverse* swimming pattern, the flagellum rotates CCW and pushes the cell body from behind (run), and then the bacterium reverses its direction of motion and continue moving in the opposite direction (reversal), where the flagellum rotates CW and pulls the cell body in an almost straight trajectory. This type of swimming strategy is prevalent in the ocean [23, 25].

In *run-reverse-flick* swimming pattern, the cell executes a run-reverse motion and then a flick. The flick event occurs due to a buckling instability of flagellar hook upon resuming CCW rotation, after the run and backward movement segments of the pattern. Upon a flick event, the bacterium reorients in a new direction with a turning angle of about 90°, as seen in Fig. 3.7a.

In *run-pause-run* swimming pattern, the cell body remains stationary for short periods of time after persistent swimming and then resumes its swimming, as shown in Fig.3.8a. The swimming direction after and before such events tends to remain the same, the angular change is about 0°. In some bacteria, such as *Rhodobacter sphaeroides*, a brief pause allows the cell body to reorient itself and swim in a new direction [91].

A close analysis of the trajectories revealed that the majority of the turning events is charaterized by an angle of 180°, the cell reverses its direction of swimming. *A. brasilense* cells change their swimming direction by reversal events. Cells might change their swimming of direction with an angle of less than 180° as seen in Fig. 3.9 due to rotational diffusivity [70, 25].

Run times is defined as the time between reversal events. The total number of reversals occuring up to time t follows a *Poisson process* which results in the distribution of run times obeying an exponential distribution. The run times data were fitted with the following exponential function,

$$f(t) = \alpha \, exp(-t/\tau) \tag{3.12}$$

where $\tau = 0.53\,s$ and $\alpha = 0.55$. The time-scale τ characterizes the mean run time.

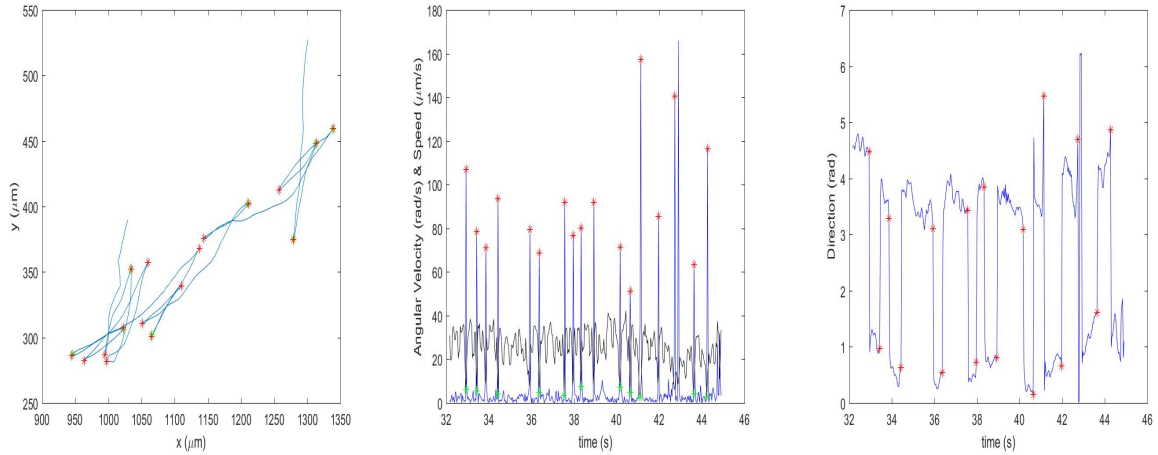

(a) **(b)** **(c)**

Figure 3.6: A swimming trajectory with typical *run, turn*, and *pause* events. (a) A representative trajectory with forward and backward runs (blue), switches in direction (red mark) and pauses (green mark). (b) The swimming speed (black) and absolute value of angular velocity (blue) over time. (c) The corresponding direction change of the trajectory over time.

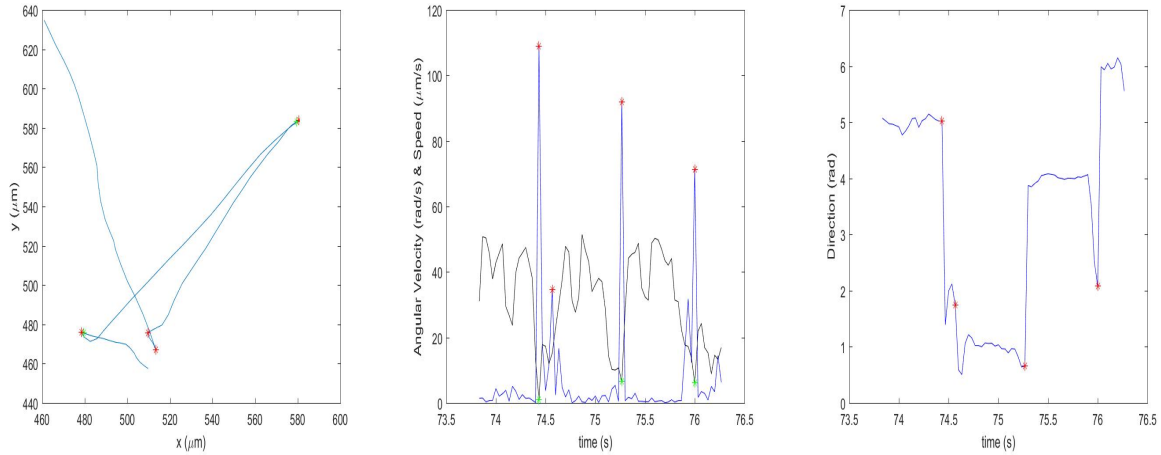

(a) **(b)** **(c)**

Figure 3.7: A swimming trajectory with typical *run, turn* and *flick* events. (a) A representative trajectory with forward and backward runs (blue), switches in direction (red mark) and pauses (green mark). (b) The swimming speed (black) and absolute value of angular velocity (blue) over time. (c) The corresponding direction change of the trajectory over time.

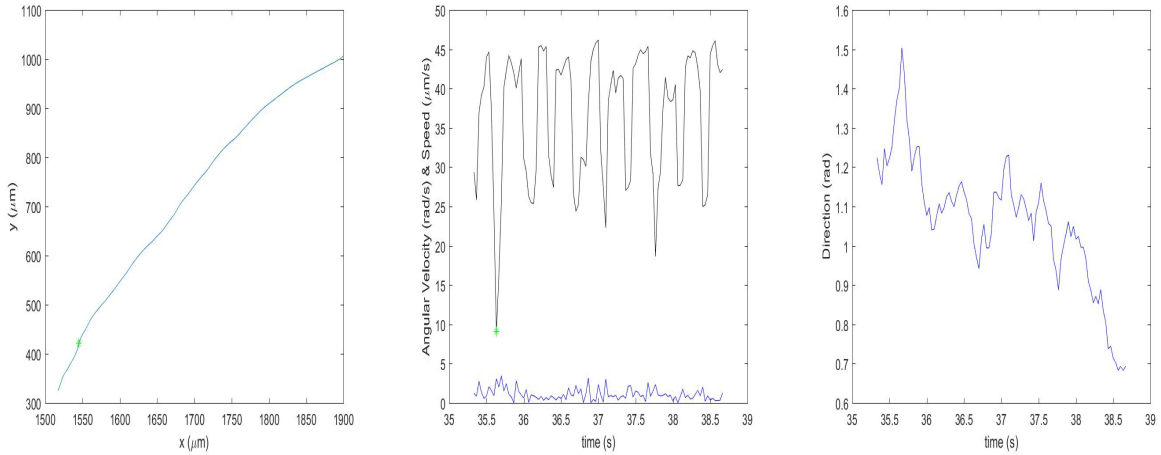

(a) **(b)** **(c)**

Figure 3.8: A swimming trajectory with typical *run*, *pause*, and *run* events. (a) A representative trajectory with forward runs (blue) and pauses (green mark). (b) The swimming speed (black) and absolute value of angular velocity (blue) over time. (c) The corresponding direction change of the trajectory over time.

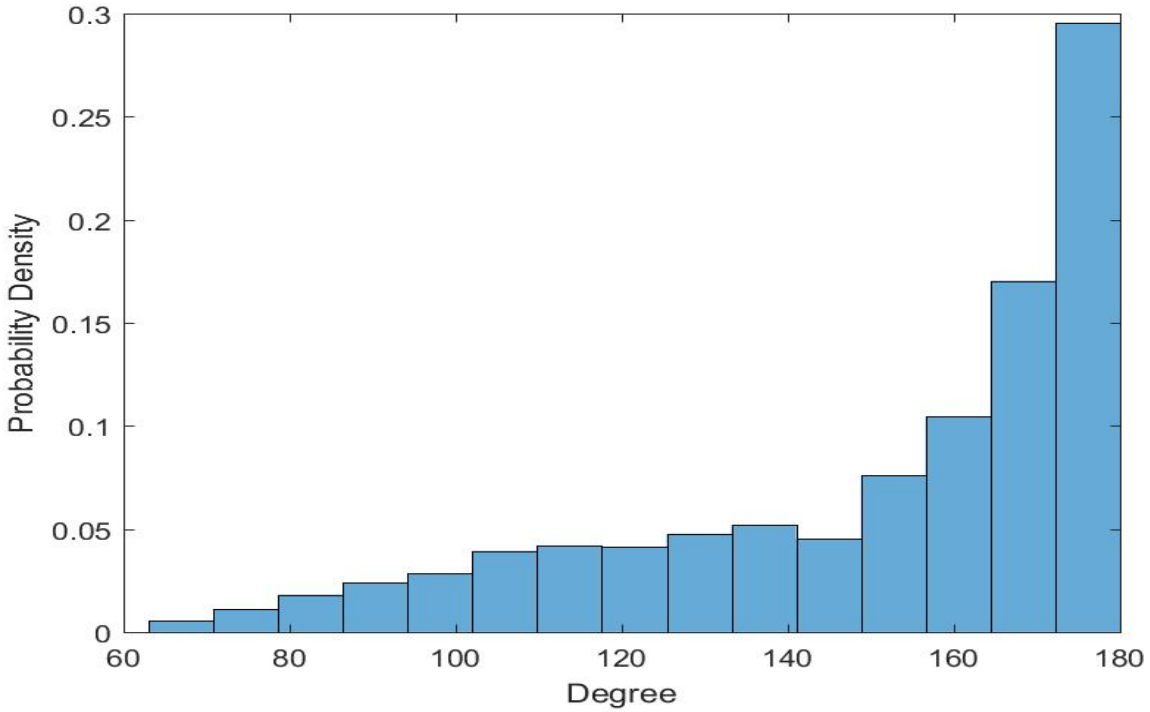

Figure 3.9: Turning angle distribution of *A. brasilense* cells. Majority of the turn events are associated with $\sim 180^\circ$ change in swimming direction.

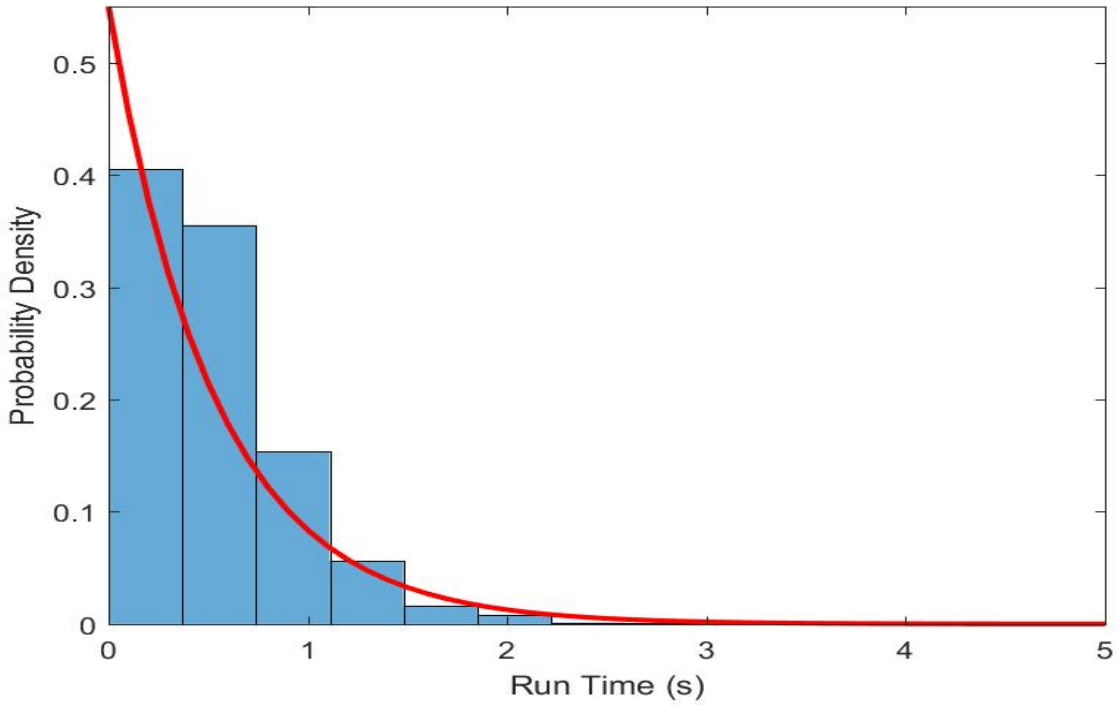

Figure 3.10: Distribution of run times between two reversal events. Trajectories with turning events were considered for this analysis. Run time is defined as the time between reversals. The distribution of run duration to obey exponential distribution. The line (red) is a fit to the exponential function, which is given by eq. (3.12)

A closer look revealed that the distribution of swimming speed of all trajectories and the one only with reversal events can be fitted by the sum of two Gaussian functions with different means and standard deviations [60, 59]. The fitting parameters for the swimming speed of all trajectories (with and without reversal events) are estimated as

$$\mu_1 = 17.63\ \mu m/s,\ \sigma_1 = 1.54\ \mu m/s$$

$$\mu_2 = 29.13\ \mu m/s,\ \sigma_2 = 5.14\ \mu m/s$$

and for the swimming speed of the trajectories with reversal events are estimated as

$$\mu_1^* = 17.68\ \mu m/s,\ \sigma_1^* = 1.52\ \mu m/s$$

$$\mu_2^* = 28.72\ \mu m/s,\ \sigma_2^* = 5.67\ \mu m/s$$

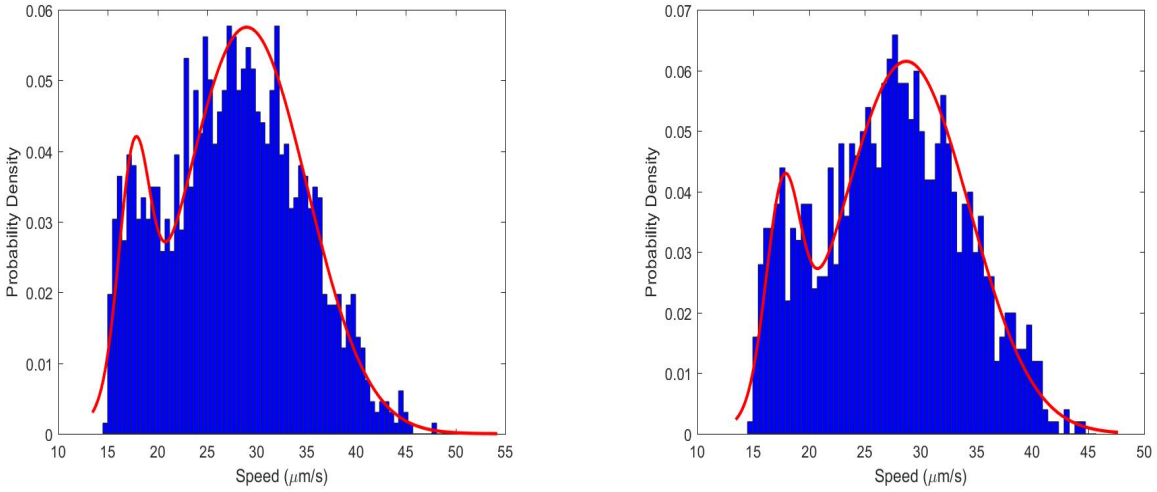

(a) **(b)**

Figure 3.11: Distribution of swimming speeds. (a) All trajectories were considered for the analysis. The distribution was fitted by a normal distribution (red curve) with means μ_1 and μ_2, and standard deviations σ_1 and σ_2. (b) Only trajectories with turning events were considered for the analysis. The speed distribution was fitted by sum of two normal distribution (red curve) with means μ_1^* and μ_2^*, and standard deviations σ_1^* and σ_2^*.

An in-depth analysis of the trajectories revealed that the swimming speeds before and after a reversal event (a pause event) are similar. We analyzed all the trajectories and calculated a ratio (R) which is the difference between the swimming speeds before a reversal, ν_i, and after a reversal, ν_{i+1}, normalized by the sum of both speeds, which is given by

$$R = \frac{\nu_{i+1} - \nu_i}{\nu_{i+1} + \nu_i} \tag{3.13}$$

We show the distrubitons of R with revarsals in Fig. 3.12a and with pauses in 3.12b. In both figures, the two maxima at $R = 0$ indicates that there is no difference, on average, in the swimming speeds before and after a reversal event (a pause event).

MSD is a computable measure of the average distance that a cell travels with respect to starting position over time lags. The results of MSD calculation allows us to characterize the mode of movement of the cells. MSD is calculated by eq. (3.5).

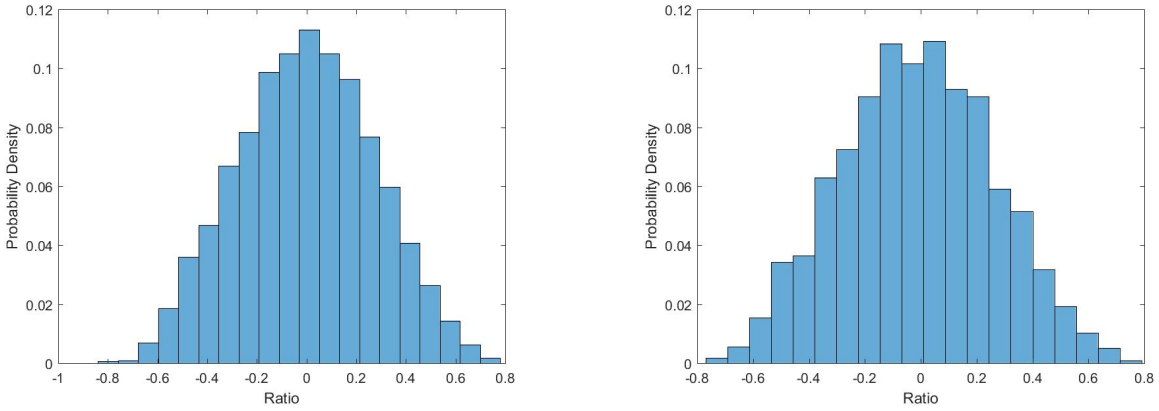

(a) **(b)**

Figure 3.12: Normalized difference between the swimming speeds before and after pause events. The normalized difference is calculated as difference between the swimming speeds before and after pause events, divided by the sum of the two swimming speeds. The ratio R is being plotted. (a) Distribution of R for trajectories with pause events. (b) Distribution of R for trajectories with reversal events. There is no major difference in swimming speed between (a) and (b).

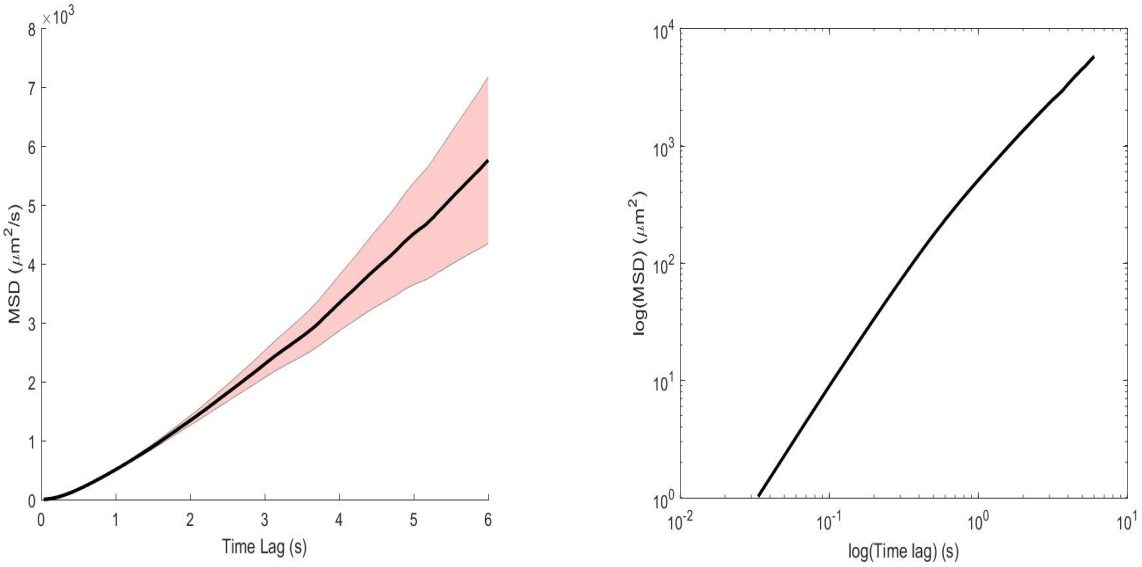

(a) **(b)**

Figure 3.13: Mean square displacement vs time lags. (a) Solid black curve is the ensemble MSD over time lags, and transperent red is standard deviation of corresponding MSD over time lags. (b) Log-log plot of MSD vs time lags.

The calculated MSD over the entire trajectory indicates that trajectories may contain more than one diffusion type [73]. As it can be seen in Fig. 3.14a, a ballistic regime (red curve) was observed over time lags less than 2 s in which the MSD has a parabolic dependence, whereas the MSD has a linear dependence over time lags greater than 2 s, the typical diffusive regime. In the diffusive regime (black curve), the slope is proportional to the diffusion coefficient of the cells, see eq.(3.6). The diffusion coefficient was found to be $D = 276\,\mu m^2/s$, which is close to what was reported for Pseudomonas putida in [116]. We also calculated and plotted the MSAD in order to determine rotational diffusivity. Fitting the linearly growing part of MSAD curve with $2D_r t$ gave $D_r = 0.072\,rad^2/s$, which is close to that reported for *E. coli* [13].

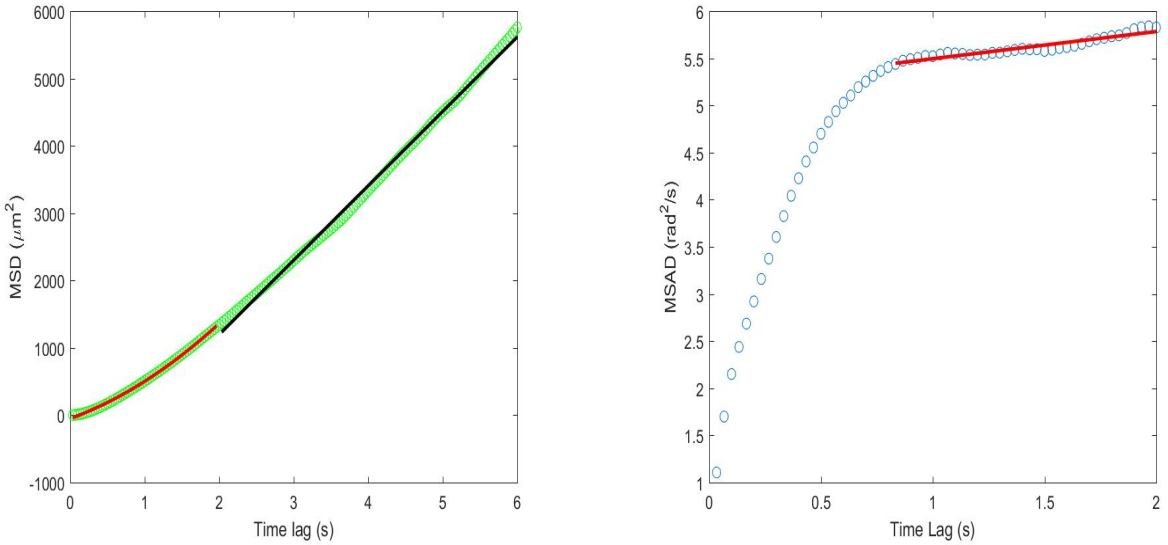

(a) **(b)**

Figure 3.14: Fitted mean Square Displacement vs time lag. (a) Fitted MSD over time lags (green curve). (b) Mean Square Angular Displacement over time lags. Fitting the linearly growing part of MSAD curve (red).

3.5.2 Analysis of mutant strains

An in-depth analysis of trajectories of different mutant strains of *A. brasilense* cells provides useful information about the role of the proteins in signal transduction pathway. Absence

of $CheA4$ greatly reduces reversal frequency, which suggest that $CheA4$ protein is the main regulator in the system, as it has been reported in [83].

The data shown in Fig.3.15 suggests that cells are unable to switch the direction of the flagellar motor in absence of any of $CheY4$, $CheY6$, and $CheY7$.Thus, these three proteins must be present in the cell in order to execute a reversal event, with $CheY7$ being the main regulator of the motor switch.

Pause frequency is dramatically suppressed in absence of $CheY7$ or its combination with other CheYs. A trajectory with more turn events would have more pause events, as it was reported before in [33]. Thus, pause frequency is positively correlated with reversal frequency.

Swimming speed of cells is less in strains lacking $Che1$ and $Che4$ operons. On the other hand, absence of $CheY4$ hardly affects speed. These results agree with the hypothesis that Che_1 is responsible for controling swimming speed in *A. brasilense cells*[15, 83].

We used Pearson correlation coefficient in order to measure a relationship between pause frequency and reversal frequency in all strains of *A. brasilense* cells. It was found that reversal frequency and pause frequency are strongly correlated as seen in Fig. 3.18. If reversal frequency increases (decreases), pause frequency also increases (decreases). Thus, Changes in reversal frequency and pause frequency are qualitatively similar.

In comparing different *A. brasilense* strains, the result revealed that the correlation between swimming speed and reversal frequency in all strains is weak as shown in Fig. 3.19.

3.6 Conclusion

The swimming behavior of the single polar flagellated bacterium *A. brasilense* was investigated. Analysis of experimental chemotactic data shows that *A. brasilense* cells display three different types of swimming behavior, which we labeled "run-and-reverse", "run-pause-run", "run-reverse-flick".

Our statistical analysis of trajectories for wild-type cells has shown that motility parameters of these cells obey distinct probability distribution functions. Swimming speed

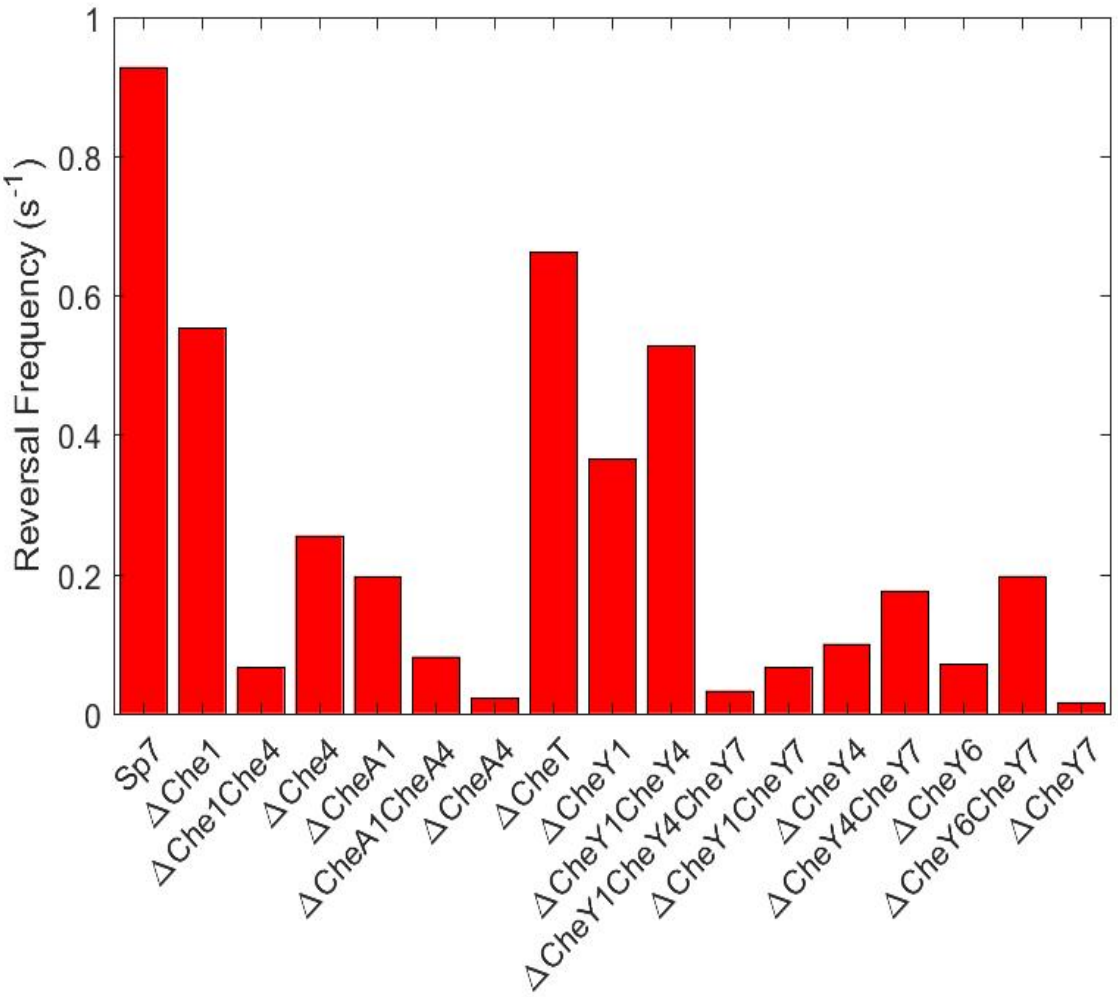

Figure 3.15: Reversal frequency for different strains in *A. brasilense* cells. The wild-type is Sp7, the others are knock-out mutants with the indicated protein missing. The reversal frequency of wild-type strain (Sp7) was $\sim 0.93\ s^{-1}$. All knock-out mutants exhibit reduced reversals.

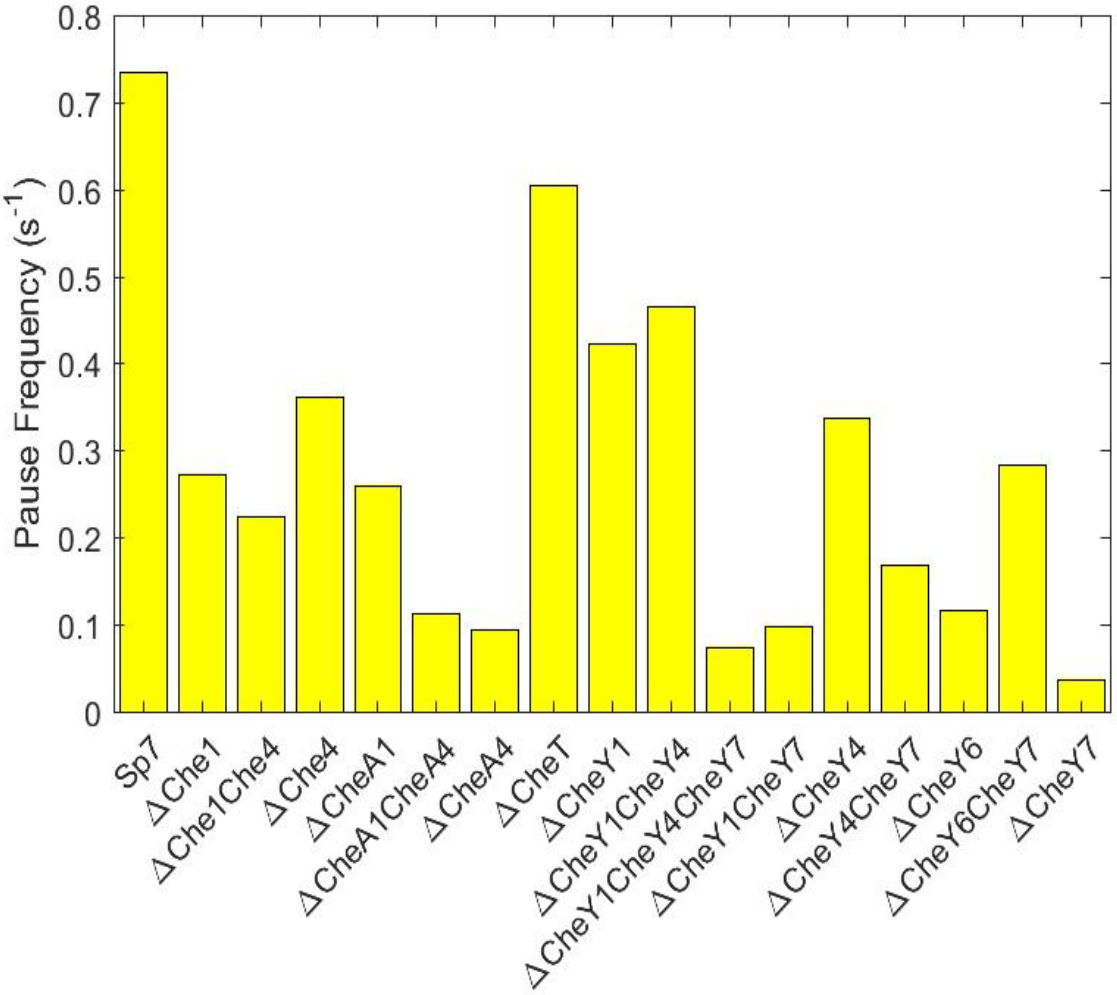

Figure 3.16: Pause frequency of different strains in *A. brasilense* cells. The pause frequency of wild-type strain (Sp7) was $\sim 0.74\ s^{-1}$.

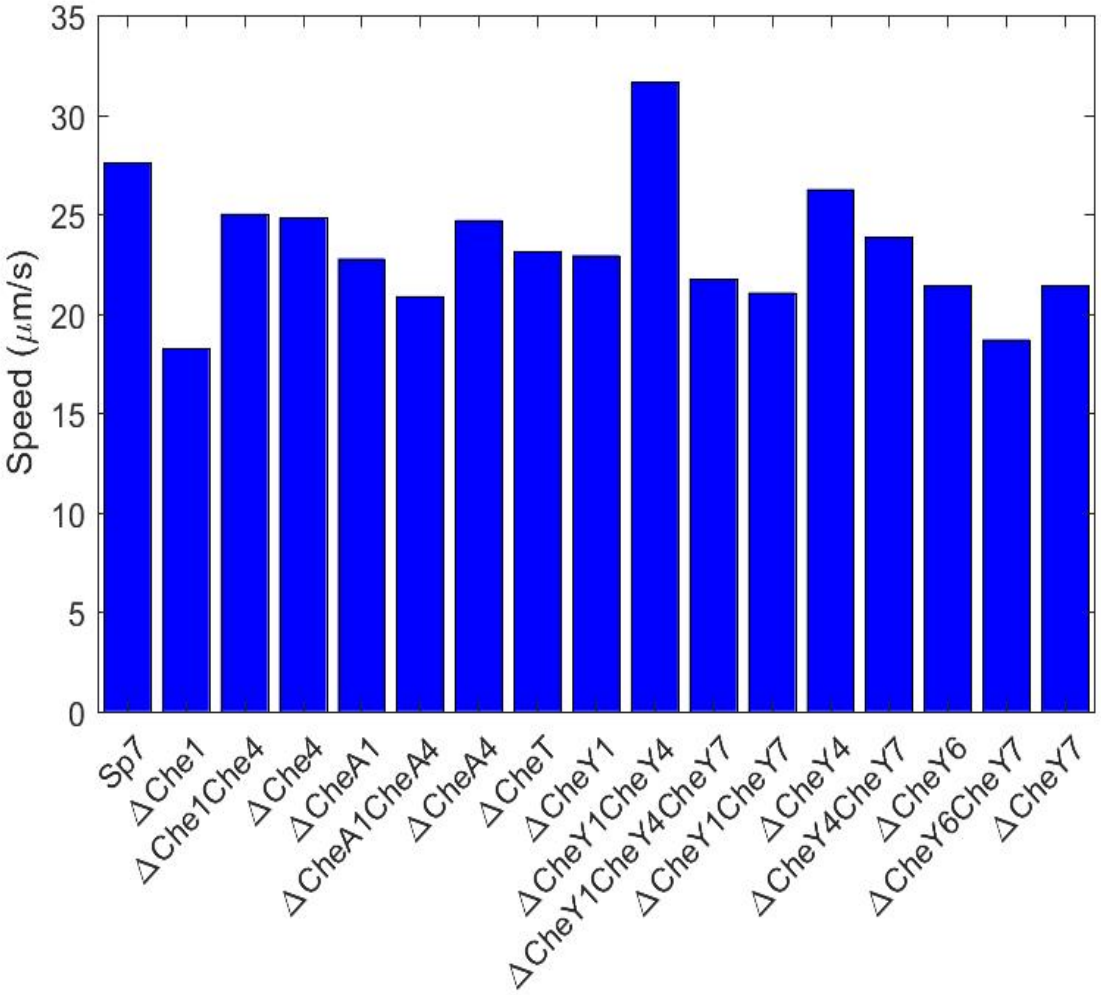

Figure 3.17: Swimming speed for different strains in *A. brasilense* cells. The speed of wild-type strain (Sp7) was 27.6 $\mu m/s$.

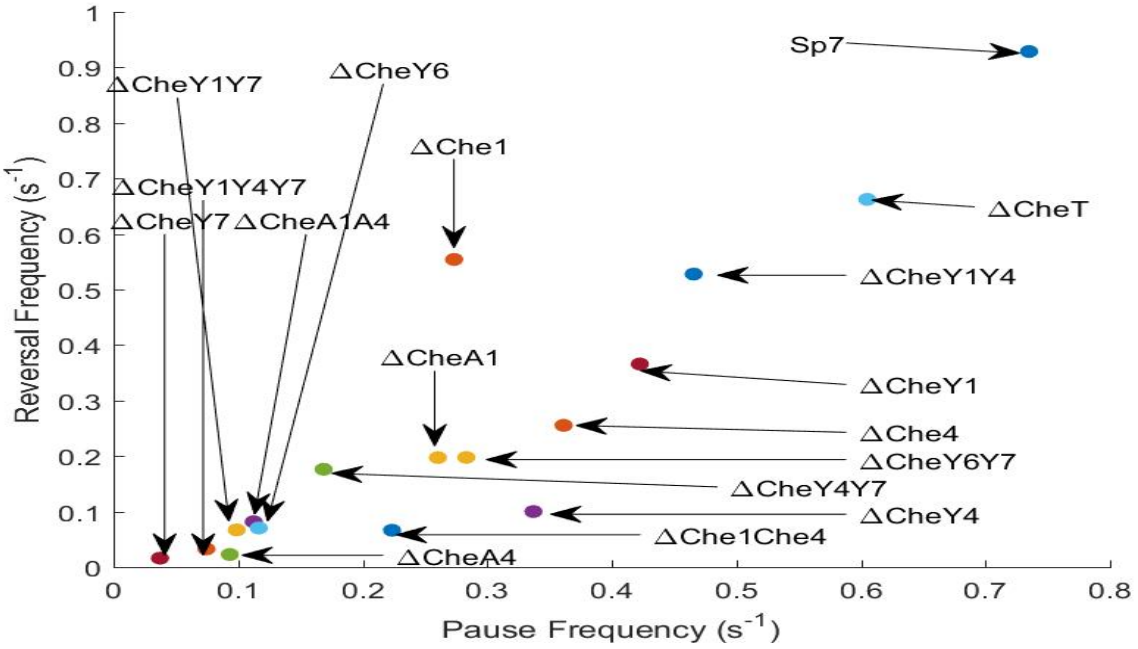

Figure 3.18: Correlation between pause frequency and reversal frequency for all strains. The correlation was calculated as 0.91.

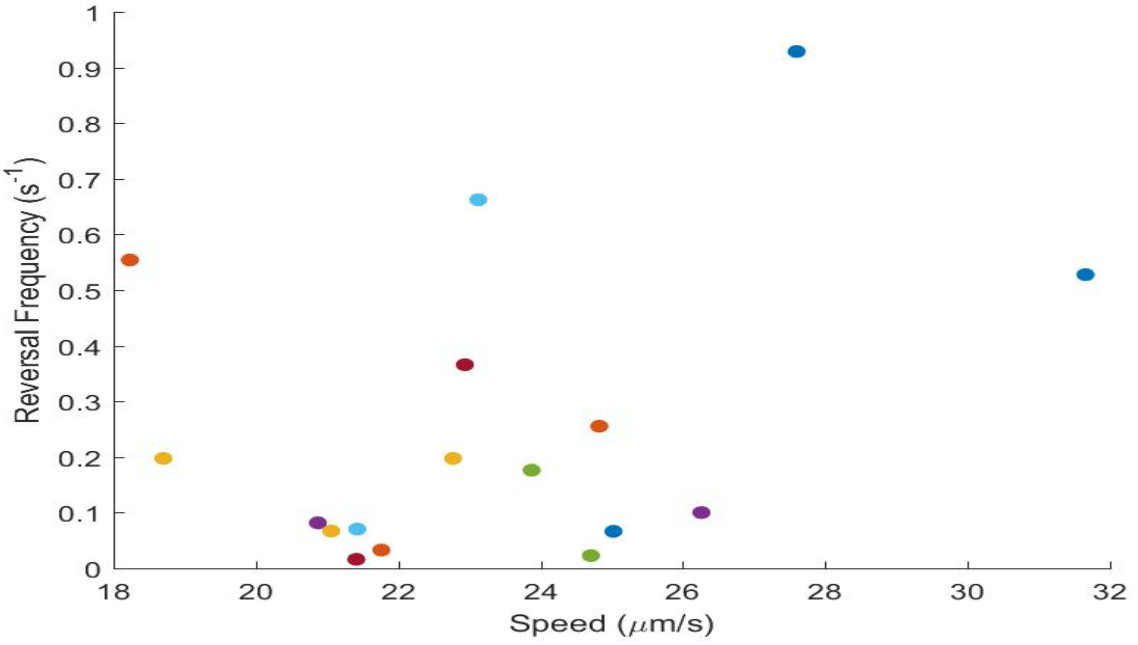

Figure 3.19: Correlation between swimming speed and reversal frequency for all strains. The correlation was calculated as 0.34. Each color represents different strains of *A. brasilense* cells and these strains are label as in Fig. 3.18

of trajectories with or without turning events obey a sum of two normal distribution. The run times between two reversal events follow exponential distribution. Furthermore, the swimming speeds, on average, before and after a turning (or a pause) event are similar. Diffusion coefficient and rotational diffusion coefficient were obtained respectively by a mean squared displacement and a mean square angular displacement analysis of bacteria trajectories. The calculated diffusion and rotational diffusion coefficients agree well with the those reported before.

The swimming behavior and motility parameters of *A. brasilense* cells are controlled by the rotation of flagellar motor, which is regulated by the main output (phosphorylated CheY) of the chemotaxis signal transduction pathways. It has been reported that there are four chemotaxis operons in the genome of *A. brasilense* and only two of them are responsible for chemotaxis and aerotaxis [83]. However, the connectivity of signal transduction pathways in *A. brasilense* is still unknown and Chapter 4 addresses this issue.

Different strains of *A. brasilense* cells were analyzed in order to understand the role of each protein in the signaling pathways. Experimental results (reversal frequencies in Fig.3.15) obtained by our tracking algorithm has shown that the flagellar motor switch is regulated by three $CheY$'s: $CheY_4$, $CheY_6$ *and* $CheY_7$. In the absence of any of these three $CheY$'s, the bacterium is unable to execute a turn (reversal), which suggests that all three CheYs must be present in the bacterium genome in order to execute a reveral. Moreover, statistical results in the absence of $CheA_4$ has shown that the bacterium cannot reverse at all. This suggest that $CheA_4$ is the main regulator in the systems, as reported before. The swimming speed and pause frequencies for different strains of *A. brasilense* have been obtained. It was found that swimming speed was affected the most in the absence of Che_1 operon and hardly affected in the absence of $CheY_4$ protein. These results agree well with those reported before. We found that there is a strong correlation between pause and reversal frequencies.

Our tracking software can handle any type of digital videos. There is no limitation on the size and the type of the videos. The only input for our tracking software is a digital video. However, the parameters must be fine-tuned depending on the objects of interest.

Chapter 4

Chemotaxis Signaling Transduction Pathway

4.1 Introduction

Bacteria are able to change their swimming direction by a change of the rotation direction of flagella that attached to their body [12, 6]. In peritrichously flagellated *Esherichia coli (E. coli)*, the swimming behavior is characterized by straight runs (period of forward movement) interupted by random changes in the swimming direction, tumbles (sudden reorientation of swimming direction). When flagellar motors rotate counterclockwise (CCW), a default direction, which causes them to come together and form a bundle that pushes the cell forward, called runs. On the other hand, when one or more of the flagellar motors rotate clockwise (CW), the flagella bundle flies apart and it leads to the tumbling of bacteria. Tumbling periods enable the bacteria to alter its swimming direction, randomly determined swimming directions [97, 6]. Run times ($>$ 1 second or so) are longer than the time spent in tumbling (0.1 second or so) [123, 19]. When motile bacteria move up a gradient of an attractant, the frequency of tumbling decreases, allowing the bacteria to bias their movement towards the attractant. In contrast, when the bacteria move up a gradient of a repellent, the frequency of tumbling increases, allowing the bacteria to bias their movement away from the repellent [68, 18, 33]. As a result, the sequence of runs and tumbles allows the bacteria achieves a net motion towards chemoattractants or away from chemorepellents.

Bacteria carry out chemotaxis by modulating the tumbling frequency which is the main output of the signaling pathway [3]. The pathway acts as a computational unit. Each component of the pathway receives one or more inputs, the signals, and then generates one or more outputs. From the sensing of external stimuli to the activation of the flagella motor switch, a series of chemical reactions are involved in processing and relaying the signal [21, 82]. The processes from detection of signals to a response may be depicted as in Fig.4.1.

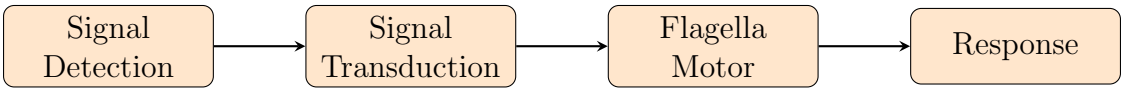

Figure 4.1: The processes from signal to response in bacteria.

At the cellular level, taxis behaviors depend on a dedicated signal transduction system, a network of interacting proteins that controls the reversal frequency and swimming direction. This network integrates environmental cues into a behavioral response [108, 121, 95]. This behavior is achieved by detecting the changes of environmental chemical concentrations by chemoreceptors, sending a signal through internal signal transduction pathway to the flagella motor which regulates the tumbling frequency according to the concentrations of proteins in the signaling pathway [110]. The chemical reactions in the chemotaxis signal transduction pathway for *E. coli* is described in detail in the next section.

4.2 Chemotaxis Pathway in *Esherichia coli*

The components of chemotaxis signal transduction systems that mediate changes in environmental conditions are highly conserved among bacteria. The molecular mechanism of chemotaxis signal transduction in *E. coli* has been extensively studied in most detail and used as a model organism. It possesses a *single* chemotaxis system [20, 37, 109, 49]. The chemotaxis pathway in this bacterium is a simple network of protein interactions, pictured in Figure 4.2. This network enables bacteria to couple the sensing of external cues to the flagellar motors through a cytoplasmic signaling cascade and ultimately it determines the swimming pattern of the cells. The major players in the pathway are chemoreceptors (also referred to as Methyl-accepting proteins or MCPs) and cytosolic proteins (Che) [40, 85].

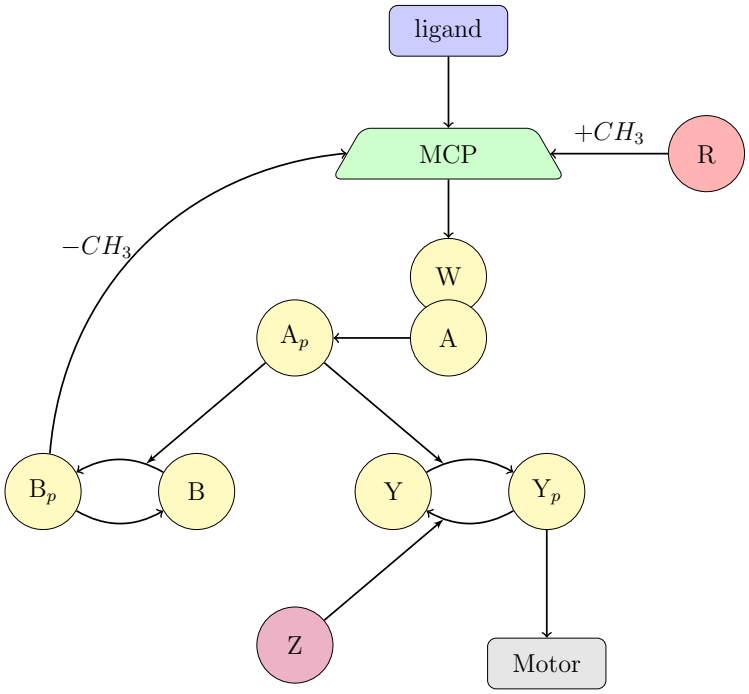

Figure 4.2: A schematic diagram of the *E. coli* chemotactic signal transduction pathway. Methyl-accepting chemotaxis proteins, MCPs, transduce signals from chemoeffectors in the periplasmic space thereby modulating the activity of the histidine kinase, CheA, which is linked to the MCPs by an adaptor protein CheW. Once CheA is phoshorylated via ATP, it transfers the phosphate group to the response regulators CheB and CheY whose phosphorylated forms interact with the MCPs and the flagellar motor switch, respectively. Methyltransferase, CheR, also interacts with the MCPs whereas the dephosphatase CheZ dephosphorylates CheY for signal termination.

$MCPs$, $CheW$, $CheA$ and $CheY$ constitute an excitation pathway in chemotaxis, whereas $CheZ$, $CheR$ and $CheB$ constitute an adaptation pathway [125, 126].

The detection of extracellular cues via dedicated receptors initiates signal transduction during bacterial chemotaxis. The existence of suitable receptors is very important for a chemotactic response; in the absence of such receptors, the bacteria show no response [58, 41, 50]. The E. coli genome encodes five receptors that are clustered at one or both cell poles; four transmembrane MCPs and one MCP-like receptor [123, 105]. Each MCP senses the periplasmic concentrations of a specific chemoeffectors: Tar (aspartate and maltose chemoreceptor), Tsr (serine chemoreceptor), Trg (ribose and galactose chemoreceptor), Tap (dipeptide chemoreceptor), and Aer (oxygen) which is MCP-like cytoplasmic receptor but does not have a periplasmic sensing domain [94, 14].

Bacterial transmembrane receptors (MCPs) constitute an extracellular ligand-binding domain (N-terminal domain). They span the cell membrane to help detect physico-chemical cues in the environment. There is a conserved cytoplasmic signaling domain (C-terminal domain) that controls motor responses and undergoes reversible methylation at multiple sites [10, 7, 105], whereas the cytoplasmic receptor contains a C-terminal Per-Arnt-Sim (PAS) domain that binds a flavin adenine dinucleotide (FAD) cofactor to sense the change in electron transport by sensing a change in redox potential, PMF or possibly electron flux due to changes in oxygen concentrations [128]. Most of the MCP receptors in *E. coli* form clusters at the cell poles [19, 78, 42]. In these clusters, the receptors are organized into units of trimers of dimers, which form stable ternary signaling complexes with intracellular proteins, the chemotaxis histidine kinase $CheA$ and adaptor protein $CheW$ [21, 22]. The presence of $CheW$ and $CheA$ is required for $MCPs - CheA - CheW$ complex formation [108]. It is believed that receptor clustering contributes to signal amplification and the high sensitivity of *E. coli* chemotaxis network, giving the ability to respond to very small changes in chemoeffector concentration over a wide range of background concentrations [67, 77]. Cooperative binding of the response regulator $CheY$ protein to the flagellar motor switch complex $FliM$ also plays a role in signal amplification [26, 130, 131]. The cell is capable of integrating signals (different stimuli) from a variety of receptors to generate a unified

output [97]. The signals from multiple MCPs to the $CheA$ kinase is made by $CheW$, which functionally links the chemoreceptors to the $CheA$ kinase [51, 41].

The signaling activity of receptors is thought to exist in two states, active (activating $CheA$ autophosphorylation) or inactive (inhibiting $CheA$ autophosphorylation) [18, 41]. The catalytic activity of $CheA$ is affected by occupancy of receptors with a ligand (an attractant or a repellant). The signaling properties of the receptors is influenced not only by ligands, but also by the state of methylation of specific glutamate residues within their cytoplasmic domain [111, 81]. Ligand binding to a chemoreceptor induces a conformational change in receptor proteins and this conformational change in turn causes a change in the rate of $CheA$ autophosphorylation. Attractant binding to chemoreceptors induces a conformational change in the receptors that is transmitted through the membrane, changing the cytoplasmic signaling domain to the positive signaling mode. The positive signaling conformation inhibits $CheA$ autophosphorylation, reducing $CheY$ phosphorylation and thereby promoting CCW rotation of the flagella, which results in smooth swimming of the cell without direction changes [98, 104]. On the other hand, upon binding of repellents or decreasing concentration of attractants, chemoreceptors undergo a comformational change which increases the autophosphorylation rate of $CheA$ [49, 95]. The activated $CheA$ acquires a phosphate group through autophosphorylation. The Phosphorylated $CheA$, $CheA_p$, then transfers the phosphate group to the response regulator proteins $CheY$ and $CheB$. The phosphorylated $CheY$ is released from the chemotaxis cluster and diffuses through the cell, binds the flagellar switch complex protein $FliM$ and induces CW motor rotation, a change in the swimming direction of the motile cell. The phosphotransfer between $CheA_p$ and $CheY$ occurs faster than the phosphotransfer between $CheA_p$ and $CheB$ in order to respond to changes in the levels of chemoeffector, to adapt to the changed environmental conditions [119, 96]. Signal termination is crucial for the bacterial cells to continuously sense and appropriately respond to environmental stimuli. Therefore, even though $CheY_p$ is dephosphorylated spontaneously, this process is enhanced by the phosphatase $CheZ$ [30, 109, 130]. This is the excitation phase of the bacterial chemotaxis pathway.

The bacterial chemotaxis pathway has the ability to detect and adapt to changes in the levels of external stimuli over a wide range (five orders of magnitude). After initial response to

environmental changes, the bacteria tumbling frequency returns to its prestimulus level [74]. This adaptation mechanism allows the cell to remain sensitive to respond to further changes since the mechanism for temporal sensing is dependent on adaptation to the current level of external stimuli [117]. Bacteria are too small to detect spatial differences in the concentration of external stimuli; instead, they detect gradients by use of a memory mechanism which is based on a temporal comparison that requires a short-term memory [121]. This memory mechanism enables the bacteria to compare present and past environmental conditions they encountered recently [100]. Methylation and demethylation at the level of receptors occur at much slower time scales than other reactions involved in the network, thereby providing a memory mechanism..

The adaptation phase of the bacterial chemotaxis pathway involves the methyltransferase $CheR$ and the methylesterase $CheB$, which are the only known chemoreceptor modification enzymes in *E. coli* [10, 6]. $CheR$ adds methyl groups to the specific glutamate residues on cytoplasmic domain of chemotaxis receptors in response to changes in the receptor conformation and thus kinase activity, whereas $CheB_p$ removes the methyl groups. $CheR$ preferentially methylates receptor in an inactive conformation and phosphorylated $CheB$ preferentially demethylates receptors in an active conformation [81]. E. coli mutants lacking $CheB$ and $CheR$ have tumbly and smooth swimming biases, respectively [110]. An increase in $CheB_p$ concentration reduces the receptor methylation states, which mediates adaptation by the ability of the receptor to decrease $CheA$ autophosphorylation [122, 108]. The demethylation process serves as the feedback control of the chemotaxis system [119]. Receptor methylation compensates for attractant binding, by modifying the receptor to be in the active state. Thus, $CheR$ promotes adaptation to increasing levels of attractant, and $CheB$ promotes adaptation to decreasing levels of attractants [21, 82].

4.3 Chemotaxis Pathway in *Azospirillum Brasilense*

It has been found recently that many bacteria possess chemotaxis pathways that are more complicated than the well-known example of *E. coli*. They contain *multiple* homologues of the proteins found in E. coli pathway [97, 90]; may contain chemotaxis proteins not found

in E.coli: *CheC*, *CheD* and *CheV* [92, 93]; may not contain some of the E. coli proteins: *CheR* and *CheB* [96, 128]. In addition, some bacteria possess multiple chemotaxis systems in their genomes, unlike E. coli genome which has only one chemotaxis system [95, 47]. For example, *Rhodobacter sphaeroides* has four chemotaxis systems; *Rhodospirillum centenum* has three chemotaxis systems, whereas *Myxococcus xanthus* has nine chemotaxis systems. Some of these chemotaxis systems were reported to regulate cell size, flagellar systhesis, biofilm formation, cyst formation, and other cellular functions, other than flagellar motility [16, 83, 45].

A. brasilense is a motile soil alphaproteobacterium that colonizes the rhizosphere of various agronomically important grasses and cereals, such as wheat, corn, maize, beans and rice, promoting plant growth [99]. These gram-negative bacteria have the ability to fix atmospheric nitrogen under low oxygen concentration (microaerophilic conditions) [133]. Motility and chemotaxis are vital traits of these soil bacteria that provide them a competitive advantage in the rhizosphere, allowing them to actively sense and move towards plant root exudates. *A. brasilense* cells swim by rotating a *single* bi-directional polar flagellum [72, 122]. These cells use run-and-reverse strategy [16]. When the flagellar motor rotates counter-clock-wise (CCW), the flagellum pushes the cell forward, called **runs**. When the flagellar motor rotates clock-wise (CW), it pulls the cell in the backward direction and causes **reversals**, which may also reorient the cell in a new direction by a **flick** [132].

The available genome squence of *A. brasilense* reveals the presence of four distinct chemotaxis operons *Che*1, *Che*2, *Che*3, and *Che*4 [124], depicted in Fig.4.3. However, *A. brasilense* cells utilize only two pathways, *Che*1 and *Che*4, to regulate chemotaxis. The *Che*1 pathway regulates transient changes in swimming speed in response to chemoeffector. The cells were impaired but not null for chemotaxis when it was deleted. Thus, *Che*1 has a minor role in chemotaxis. The *Che*4 pathway regulates the probability of reversal in the swimming direction. The cells were null for chemotaxis when it was deleted. Experimental evidence indicates that signals from *Che*1 and *Che*4 are functionally integrated to coordinate changes in swimming motility patterns in response to physicochemical cues, despite each of *Che*1 and *Che*4 regulating different signaling outputs [110, 15, 96, 83, 46]. It is unknown how these two chemotaxis pathways coordinate singaling output to generate a single integrated

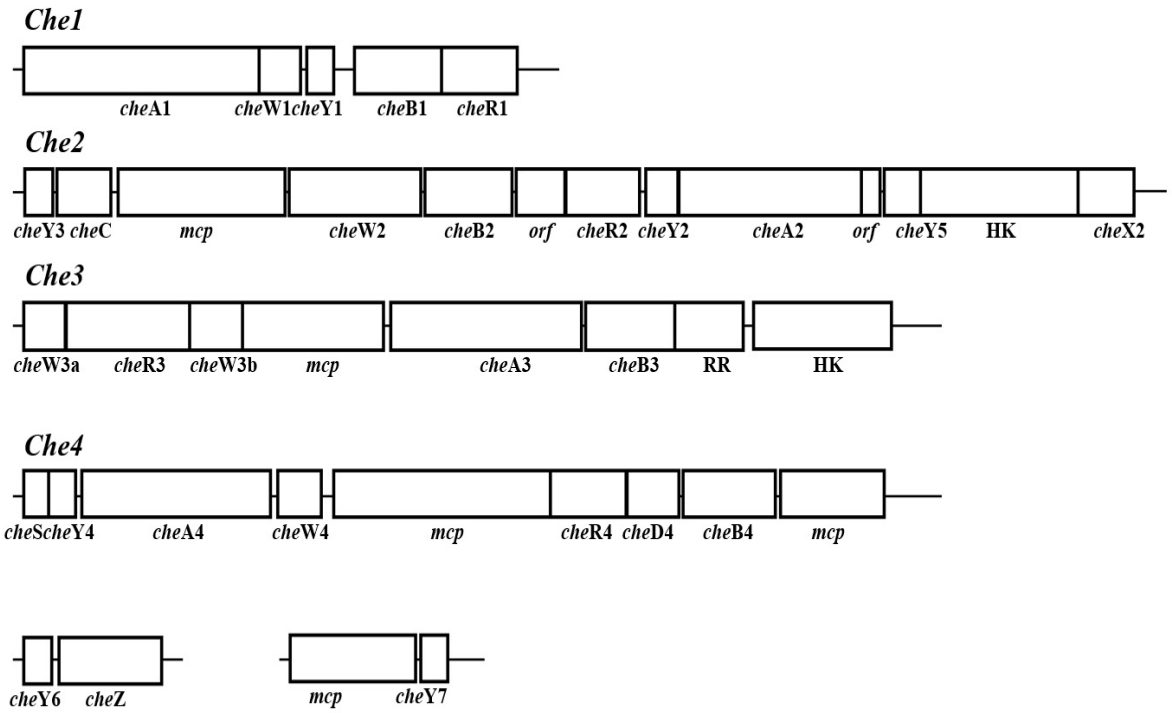

Figure 4.3: Chemotaxis genes encoded in *A. Brasilense* genome. *Che*1 pathway controls the swimming velocity of cells in response to changes in gradients of physicochemical cues and has a minor role in regulating the swimming reversal frequency. *Che*2 pathway is involved in flagella biosynthesis. *Che*3 is a chemotaxis-like alternative cellular function (ACF) pathway that is involved in cyst cell production. *Che*4 is the dominant pathway controlling the probability of changes in the swimming direction. It is interesting that different aspects of swimming behavior are controlled by different pathways in this organism. *Che*1 and *Che*4 pathways have been experimentally determined to be important in chemotaxis to regulate motility parameters. Adopted from [83]

response. This is a main issue explored in this chapter via mathematical modeling of signal transaction pathways.

It has been reported that there are over 40 chemoreceptors, multiple *CheA*, *CheW*, *CheY*, *CheZ*, *CheB*, *CheR*, *CheC* and *CheD* homologues in the *A. brasilense* genome [124, 65, 1]. The presence of multiple chemotaxis pathways and many additional chemotaxis proteins in *A. brasilense* genome indicates how complex chemotaxis pathway and signal transduction in this organism is. The signal transduction proteins and chemorecetors are organized and localized into two distinct sensory clusters and the signaling output of both clusters are required for chemotaxis and aerotaxis in *A. brasilense* [15, 96].

Experimetal results revealed that these clusters do communicate with each other. This cross-talk between the clusters originates at the chemoreceptors level [45, 110, 1]. Chemoreceptors of these two distinct clusters preferentially interact with both *CheA*1 and *CheA*4 (cluster 1) or *CheA*4 (cluster 2) [96, 1, 45]. Chemoreceptors failed to assemble into signaling clusters in the absence of *CheA*1 and *CheA*4. In the absense of *CheA*4, Tlp1 (Transducer like protein 1) and Tlp4a clusters were more diffused than in the wild-type, thus localization of Tlp1 and Tlp4a chemoreceptors is dependent on *CheA*4. It was also reported that Tlp1 and Tlp4 chemoreceptors belong to two physically distinct clusters since deleting Tlp1 mutant does not affect Tlp4 localization, expression and cluster formation, suggesting that Tlp1 signals in cluster 1 and Tlp4 signals in cluster 2 [65]. *AerC* (transducer for Aerotaxis and related responses, cytoplasmic) is a soluble chemoreceptor that localizes to the cell poles under nitrogen-fixing conditions [5, 128] and its localization to the cell poles is affected in the *Che*1 deletion background, and this chemoreceptor also affects reversal frequency controlled by the signaling output of the *Che*4 operon. Altogether, these data suggest that Tlp1 and Tlp4 interact with chemotaxis protein in the *Che*4 pathway and signal likely via the *Che*4; that *AerC* interacts with chemotaxis proteins from both *Che*1 and *Che*4 pathways and likely signals via both *Che*1 and *Che*4, provinding evidence for the cross-talk between disctinct clusters at the receptors level [110, 96]. Since *Che*1 is the ancestral pathway in *A. brasilense*, most of chemoreceptors are predicted to be in cluster 1 [1, 45].

The main output of the chemotaxis system is the motor switching which is regulated by $CheY$s. Since $CheY$ is required for motor switching, deletion of either $CheY$ or $CheA$ leads to smooth swimming phenotype, whereas overexpression of $CheY$ or $CheA$ leads to higher reversal frequency. A double mutant of $CheY1$ and $CheY4$ was shown to have residual reversal frequency in *A. brasilense*, and this result implies that there are some other $CheY$s that contribute motor switching [83]. There are seven $CheY$ proteins encoded in the genome of *A. brasilense*.

The connectivity of signaling pathways in *A. brasilense* is unknown. Mathematical modeling has provided considerable insight into the mechanism of chemotactic signaling in E. coli and other bacteria [81, 82, 92, 118, 47]. To understand the role of each signaling cluster, below we present an Ordinary Differential Equations (ODE) model, pictured in Figure 4.4, based on experimental observations. The model includes receptor-ligand binding, methylation/demethylation, phosphorylation/dephosphorylation and motor actuation. The corresponding reactions of each process are shown in Table 4.1. We use the model to understand the properties of signaling pathways and their connectivity. The model enables us to make testable predictions of the system behavior under different experimental conditions, which leads to new information that has not been uncovered by the experiments, or may be unattainable (or very difficult to attain) experimentally.

4.4 Possible pathway connectivities in *A. brasilense* chemotaxis

We applied model invalidation method to understand the connectivity of the *A. brasilense* chemotaxis system. The results from Chapter 3 revealed that the flagellar motor cannot be switched in absence of any of $CheY_4$, $CheY_6$, and $CheY_7$. It has been also reported that phosphorylated Che_4 binds to the flagellar switch directly [83, 65, 15]. It is still unknown whether $CheY_6$ and/or $CheY_7$ binds to the flagellar motor switch, or some of $CheY$'s affect some other proteins in the chemotaxis system to influence the switch activity indirectly, for example, by recuiting some protein which affects $CheA_4$ activity.

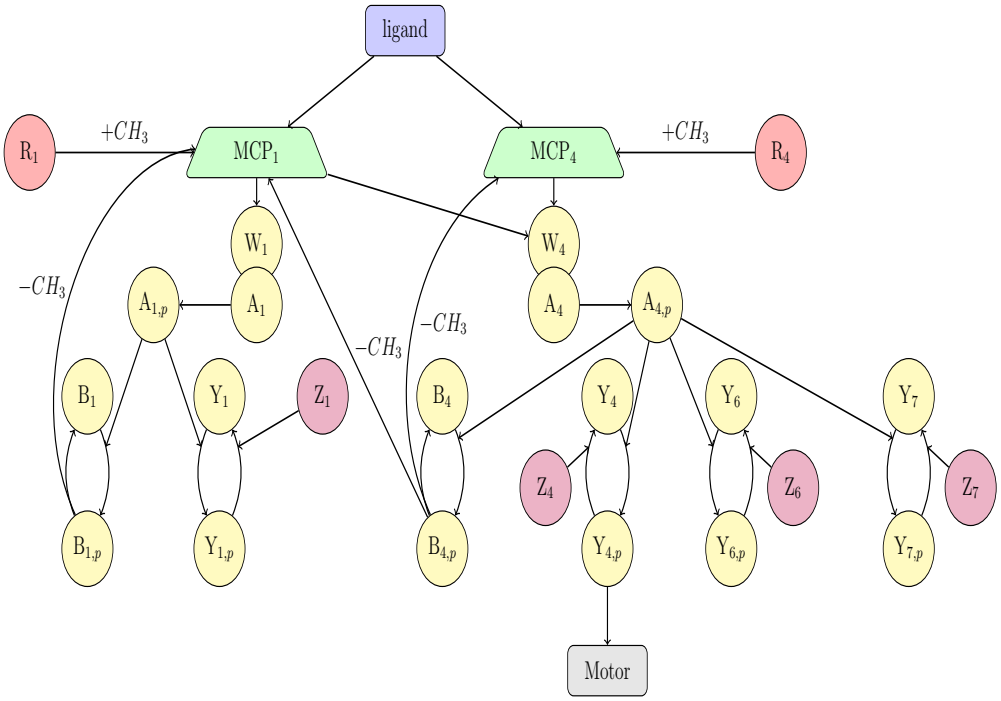

Figure 4.4: A schematic diagram of the *A. Brasilense* chemotactic signal transduction pathways. The currently known localization and connectivity of the chemotaxis pathway in *A. brasilense* is shown. Active MCP_1 [MCP_4] increases autophosphorylation of $CheA_1$ [$CheA_4$], then phosphoryl groups are transferred from $CheA_1$ [$CheA_4$] to $CheY_1$ [$CheY_4$] and $CheB_1$ [$CheB_4$]. While phoshorylated, $CheY_1$ ($Y_{1,p}$), [$CheY_4$ ($Y_{4,p}$)] hydrolysis is enhanced by the phosphatase $CheZ_1$ [$CheZ_4$], phoshorylated $CheB_1$ ($B_{1,p}$) [$CheB_4$ ($B_{4,p}$)] dephosphorylates spontaneously.

Table 4.1: Reactions within the *A. brasilense* chemotaxis pathways.

Type	Reaction
Ligand binding	$T_{1,mv} + L \leftrightarrow T_{1,m}L \ (\equiv T_{1,mo})$ $T_{4,mv} + L \leftrightarrow T_{4,m}L \ (\equiv T_{4,mo})$
Methylation	$T_{1,m} + R_1 \leftrightarrow T_{1,m}R_1 \quad T_{1,m}R_1 \rightarrow T_{1,m+1} + R_1$ $T_{4,m} + R_4 \leftrightarrow T_{4,m}R_4 \quad T_{4,m}R_4 \rightarrow T_{4,m+1} + R_4$
Demethylation	$T_{1,m} + B_{1,p} \leftrightarrow T_{1,m}B_{1,p} \quad T_{1,m}B_{1,p} \rightarrow T_{1,m-1} + B_{1,p}$ $T_{1,m} + B_{4,p} \leftrightarrow T_{1,m}B_{4,p} \quad T_{1,m}B_{4,p} \rightarrow T_{1,m-1} + B_{4,p}$ $T_{4,m} + B_{4,p} \leftrightarrow T_{4,m}B_{4,p} \quad T_{4,m}B_{4,p} \rightarrow T_{4,m-1} + B_{4,p}$
Phosphorylation	$T_1^a + A_{1,u} \rightarrow A_{1,p}$ $T_1^a + A_{4,u} \rightarrow A_{4,p}$ $T_4^a + A_{4,u} \rightarrow A_{4,p}$ $A_{1,p} + Y_{1,u} \rightarrow A_{1,u} + Y_{1,p}$ $A_{4,p} + Y_{4,u} \rightarrow A_{4,u} + Y_{4,p}$ $A_{4,p} + Y_{6,u} \rightarrow A_{6,u} + Y_{6,p}$ $A_{4,p} + Y_{7,u} \rightarrow A_{7,u} + Y_{7,p}$ $A_{1,p} + B_{1,u} \rightarrow A_{1,u} + B_{1,p}$ $A_{4,p} + B_{4,u} \rightarrow A_{4,u} + B_{4,p}$
Dephosphorylation	$Y_{1,p} + Z_1 \rightarrow Y_{1,u}$ $Y_{4,p} + Z_4 \rightarrow Y_{4,u}$ $Y_{6,p} + Z_6 \rightarrow Y_{6,u}$ $Y_{7,p} + Z_7 \rightarrow Y_{7,u}$ $B_{1,p} \rightarrow B_{1,u}$ $B_{4,p} \rightarrow B_{4,u}$
Motor actuation	$Y_p + FliM \rightarrow CW$

We created four different models with possible $CheY_6$, $CheY_7$ connectivities in the system. Each model in Fig.4.5 also contains all the known connectivities in Fig.4.4. First, we fitted each model with a set of parameters that produce wild-type experimental data well. We then compared the results of these models to the mutant experimental data which incorporate deletion or overexpression of some proteins.

4.5 Mathematical model

From detection of physicochemical cues to the activation of the flagellar motor, a series of chemical reactions are involved in relaying and regulating the signal. These reactions are split into three modules: sensing, signal transduction, and motor actuation, listed in Table 4.1. Assuming mass-action kinetics, these reactions can be modeled mathematically by ordinary differential equations (ODEs), which are described below.

Since both pathways (Fig.4.4) sense and process signals in the same fashion, we describe the ligand-binding/unbinding of the receptors, methylation/demethylation of the receptors and signal transduction of these signals for one generic pathway, called n^{th} pathway where $n = 1$ indicates the receptor and proteins belonging to the first pathway (cluster 1, involving MCP_1), while $n = 4$ indicates the second pathway (cluster 2, involving MCP_4).

We use the label $T_{n,m\lambda}$ for chemotaxis receptors, where $m = 0, 1, 2, 3, 4$ indicates methylation level (the number of methyl groups added to the receptor), and λ represents the status of the receptor, whether ligand-bound (o) for occupied or ligand-unbound (v) for vacant. Subscripts are used to describe whether the cytosolic protein is phosphorylated (p) or unphosphorylated (u) and (tot) is used to label total concentrations of different proteins. Superscript (i) indicates the receptor is in inactive state, and superscript (a) indicates the receptor is in active state, able to phosphorylate $CheA$.

4.5.1 Sensing

Since the timescale for ligand (L) binding is much shorter than the methylation and phosphorylation timescale, the ligand binding and unbinding can be assumed in

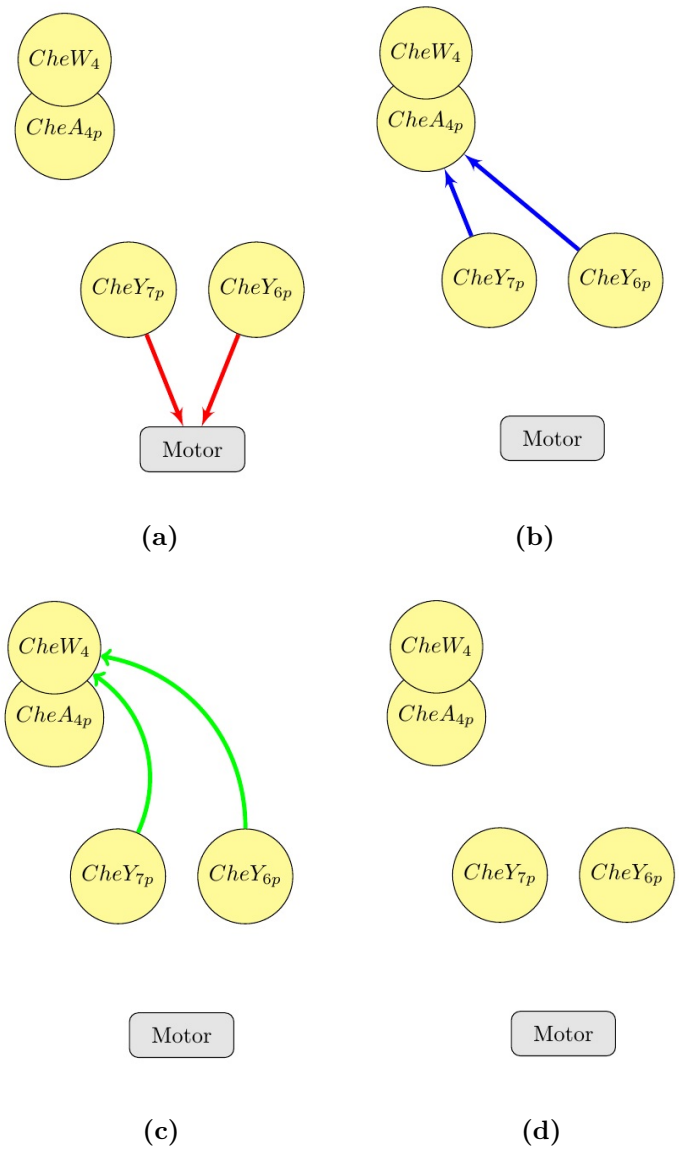

Figure 4.5: Possible additional connectivities in the *A. brasilense* chemotaxis signaling pathway. Four models of possible connectivity of $CheY_{6p}$ and $CheY_{7p}$ in the *A. brasilense* chemotaxis signaling pathway. (a) In the "red" model, $CheY_{6p}$ and $CheY_{7p}$ bind to the flagellar switch together with $CheY_{4p}$. (b) In the "blue" model, $CheY_{6p}$ and $CheY_{7p}$ prevent phosphate transfer from $CheA_{4p}$ to $CheY_4$. (c) In the "green" model, $CheY_{6p}$ and $CheY_{7p}$ affect $CheA_4$ activity. The autophosphorylation rate of Che_4 is assumed to be an increasing function of $CheY_{6p}$ and $CheY_{7p}$. (d) In this model, named the "gray" model, $CheY_{6p}$ and $CheY_{7p}$ act as phosphate sinks, they do not interact with any protein.

quasi-equilibrium and the ligand bound and unbound receptor concentrations for $T_{1,m}$ and $T_{4,m}$ at each methylation level m are given respectively by,

$$T_{1,mo} = \frac{L}{K_{1,D} + L} T_{1,m}, \qquad m = 0, 1, 2, 3, 4, \tag{4.1}$$

$$T_{4,mo} = \frac{L}{K_{4,D} + L} T_{4,m}, \qquad m = 0, 1, 2, 3, 4, \tag{4.2}$$

$$T_{1,mv} = \frac{K_{1,D}}{K_{1,D} + L} T_{1,m}, \qquad m = 0, 1, 2, 3, 4, \tag{4.3}$$

$$T_{4,mv} = \frac{K_{4,D}}{K_{4,D} + L} T_{4,m}, \qquad m = 0, 1, 2, 3, 4, \tag{4.4}$$

where $K_{1,D}$ and $K_{4,D}$ are the receptor-ligand dissociation constants for $T_{1,m}$ and $T_{4,m}$, respectively. The receptor concentrations at methylation level m is

$$T_{1,m} = T_{1,mv} + T_{1,mo}. \tag{4.5}$$

$$T_{4,m} = T_{4,mv} + T_{4,mo}. \tag{4.6}$$

The total receptor concentration of T_1 and T_4 are given by,

$$T_{1,tot} = \sum_{m=0}^{4} T_{1,m}. \tag{4.7}$$

$$T_{4,tot} = \sum_{m=0}^{4} T_{4,m}. \tag{4.8}$$

The total active receptors T_1^a and T_4^a are respectively given by,

$$T_1^a = \sum_{m=0}^{4} P_{1,m}(L) T_{1,m}, \tag{4.9}$$

$$T_4^a = \sum_{m=0}^{4} P_{4,m}(L) T_{4,m}, \tag{4.10}$$

while the total inactive receptors T_1^i and T_4^i are

$$T_1^i = \sum_{m=0}^{4}(1 - P_{1,m}(L))T_{1,m}, \tag{4.11}$$

$$T_1^i = \sum_{m=0}^{4}(1 - P_{1,m}(L))T_{1,m}, \tag{4.12}$$

$$T_4^i = \sum_{m=0}^{4}(1 - P_{1,m}(L))T_{4,m}, \tag{4.13}$$

where $P_{1,m}(L)$ and $P_{4,m}(L)$ respectively denote the total probability of the receptor complex being in active state for $T_{1,m}$ and $T_{n,m}$, and each is the sum of the probabilities of the ligand bound ($P_{1,mo}$ and $P_{4,mo}$) and non ligand bound ($P_{1,mv}$ and $P_{4,mv}$) being in active state:

$$P_{1,m}(L) = P_{1,mo}(L)\frac{L}{K_{1,D} + L} + P_{1,mv}(L)\frac{K_{1,D}}{K_{1,D} + L}. \tag{4.14}$$

$$P_{4,m}(L) = P_{4,mo}(L)\frac{L}{K_{4,D} + L} + P_{4,mv}(L)\frac{K_{4,D}}{K_{4,D} + L}. \tag{4.15}$$

The model assumes that $CheR_1$ and $CheR_4$ (denoted R_1 and R_4) respectively binds to the inactive receptors (T_1^i and T_4^i) and that phosphorylated $CheB_1$ and $CheB_4$ ($B_{1,p}$ and $B_{4,p}$) respectively binds to active receptors (T_1^a and T_4^a) ([81], [74]). Assuming that the methylation and demethylation reactions follow Michaelis-Menten kinetics, the rates are

$$r_{1,B} = \frac{k_{1,b}B_{1,p} + k_{41,b}B_{4,p}}{K_{1,B} + T_1^a}, \tag{4.16}$$

$$r_{4,B} = \frac{k_{4,b}B_{4,p}}{K_{4,B} + T_4^a}, \tag{4.17}$$

$$r_{1,R} = k_{1,r}\frac{R_1}{K_{1,R} + T_1^i}, \tag{4.18}$$

$$r_{4,R} = k_{4,r}\frac{R_4}{K_{4,R} + T_4^i}, \tag{4.19}$$

where $k_{1,b}$, $k_{4,b}$, $k_{1,r}$ and $k_{4,r}$ are catalytic constants, $K_{1,B}$ and $K_{4,B}$ are respectively Michaelis constants for the receptors demethylation reactions for T_1 and T_4, and $K_{1,R}$ and $K_{4,R}$ are respectively Michaelis constants for the receptors methylation reactions for T_1 and T_4. The

rate of methylation is proportional to the concentration of inactive receptors and the rate of demethylation is proportional to the concentration of active receptors.

The kinetic equations of receptor $T_{1,m}$ and $T_{4,m}$ can respectively be written as,

$$\frac{dT_{1,m}}{dt} = J_{1,m-1} - J_{1,m}, \quad m = 0, 1, 2, 3, 4, \tag{4.20}$$

$$\frac{dT_{4,m}}{dt} = J_{4,m-1} - J_{4,m}, \quad m = 0, 1, 2, 3, 4, \tag{4.21}$$

where $J_{1,m}$ and $J_{4,m}$ are respectively the net fluxes from methylation state m to state $m+1$ for the receptors $T_{1,m}$ and $T_{4,m}$, the flux being the difference of methylation and demethylation rates between these two states namely,

$$J_{1,m} = r_{1,R}(1 - P_{1,m}(L))T_{1,m} - r_{1,B}P_{1,m+1}(L)T_{1,m+1}, \qquad m = 0, 1, 2, 3. \tag{4.22}$$

$$J_{4,m} = r_{4,R}(1 - P_{4,m}(L))T_{4,m} - r_{4,B}P_{4,m+1}(L)T_{4,m+1}, \qquad m = 0, 1, 2, 3. \tag{4.23}$$

The end conditions for methylation fluxes are zero

$$J_{1,-1} = J_{1,4} = 0 \quad and \quad J_{4,-1} = J_{4,4} = 0. \tag{4.24}$$

4.5.2 Signal Transduction

Active T_1 receptors increase the activity of $CheA_1$ and $CheA_4$, (denoted by A_1 and A_4) whereas active T_4 receptors only increase the activity of $CheA_4$. Once A_1 and A_4 are activated, they acquire a phosphate group through autophosphorylation and transfer the phosphate group to the response regulator $CheY_1$ (Y_1) and $CheY_4$ (Y_4), respectively. Even though phosphorylated Y_1 and Y_4 can be dephosphorylated spontaneously, this process is respectively enhanced by the phosphatse Z_1 and Z_4. Activated A_1 and A_4 also transfer their acquired phosphate group to the demethylation enzymes $CheB_1$ (B_1) and $CheB_4$ (B_4). Phosphorylated B_1 and B_4 are dephosphorylated spontaneously. The kinetic equations for signal transduction are given below:

$$\frac{dA_{1,p}}{dt} = a_{1,P}T_1^a A_{1,u} - a_{1,Y}A_{1,p}Y_{1,u} - a_{1,B}A_{1,p}B_{1,u} \tag{4.25}$$
$$\frac{dA_{4,p}}{dt} = a_{4,P}(T_1^a + T_4^a)A_{4,u} - a_{4,Y}A_{4,p}Y_{4,u} - a_{4,B}A_{4,p}B_{4,u} \tag{4.26}$$
$$\frac{dY_{1,p}}{dt} = a_{1,Y}A_{1,p}Y_{1,u} - d_{1,Z}Y_{1,p} \tag{4.27}$$
$$\frac{dY_{4,p}}{dt} = a_{4,Y}A_{4,p}Y_{4,u} - d_{4,Z}Y_{4,p} \tag{4.28}$$
$$\frac{dY_{6,p}}{dt} = a_{6,Y}A_{6,p}Y_{6,u} - d_{6,Z}Y_{6,p} \tag{4.29}$$
$$\frac{dY_{7,p}}{dt} = a_{7,Y}A_{7,p}Y_{7,u} - d_{7,Z}Y_{7,p} \tag{4.30}$$
$$\frac{dB_{1,p}}{dt} = a_{1,B}A_{1,p}B_{1,u} - d_{1,B}B_{1,p} \tag{4.31}$$
$$\frac{dB_{4,p}}{dt} = a_{4,B}A_{4,p}B_{4,u} - d_{4,B}B_{4,p} \tag{4.32}$$

The model for signal transduction is the same for all models except for the "blue" and "green" models of Fig.4.5. For the "blue" model,

$$\begin{aligned}
\frac{dA_{4,p}}{dt} &= a_{4,P}(T_1^a + T_4^a)A_{4,u} - a^*_{4,Y}A_{4,p}Y_{4,u} - a_{4,B}A_{4,p}B_{4,u} \\
\frac{dY_{4,p}}{dt} &= a^*_{4,Y}A_{4,p}Y_{4,u} - d_{4,Z}Y_{4,p} \\
a^*_{4,Y} &= a_{4,Y}\frac{K_Y}{K_Y + Y_{6,P} + Y_{7,P}}
\end{aligned}$$

For the "green" model,

$$\begin{aligned}
\frac{dA_{4,p}}{dt} &= a^*_{4,P}(T_1^a + T_4^a)A_{4,u} - a_{4,Y}A_{4,p}Y_{4,u} - a_{4,B}A_{4,p}B_{4,u} \\
a^*_{4,P} &= a_{4,P}\frac{Y_{6,P} + Y_{7,P}}{K_A + Y_{6,P} + Y_{7,P}}
\end{aligned}$$

where $a_{1,P}$ and $a_{14,P}$ are respectively the phosphorylation rate of A_1 and A_4 by T_1^a active receptors and $a_{4,P}$ is the phosphorylation rate of A_4 by T_4^a active receptors. $a_{1,Y}$ is phosphorylation transfer rate from A_1 to Y_1 and $a_{4,Y}$, $a_{6,Y}$, and $a_{7,Y}$ are respectively

phosphorylation transfer rate from A_4 to Y_4, Y_6 and Y_7. $a_{1,B}$ and $a_{4,B}$ are phosphorylation transfer rate from A_1 to B_1 and A_4 to B_4. $d_{1,Z}$ is dephosphorylation rate of $Y_{1,p}$ by Z_1 and $d_{4,Z}$, $d_{6,Z}$, and $d_{7,Z}$ are respectively dephosphorylation rate of $Y_{4,p}$, $Y_{6,p}$ and $Y_{7,p}$ by Z_4, Z_6 and Z_7. Finally, $d_{1,B}$ and $d_{4,B}$ are spontaneous dephosphorylation rate of $B_{1,p}$ and $B_{4,p}$, respectively. K_Y and K_A are respectively Michaelis-Menten constants for A_4 for the "blue" and "green" models. Furthermore, the model has the following constraints:

$$\begin{aligned} A_{n,u} &= A_{n,tot} - A_{n,p} \quad n = 1, 4 \\ Y_{n,u} &= Y_{n,tot} - Y_{n,p} \quad n = 1, 4, 6, 7 \\ B_{n,u} &= B_{n,tot} - B_{n,p} \quad n = 1, 4 \end{aligned}$$

4.5.3 Motor actuation

The above intracellular signaling pathway determines the concentration of phosphorylated $CheY$, i.e. Y_p, which in turn binds to the flagellar motor ($FliM$) and decides the CW bias of the cell, that is, the fraction of time the cell spends in tumbling [130]. Using a Hill function with an appropriate Hill coefficient (h) to relate the CW bias and Y_p [26, 131], we can quantify CW bias as

$$CW = \frac{(Y_p)^h}{(H_S)^h + (Y_p)^h}, \tag{4.33}$$

with H_S a half saturation constant. The quantity $Y_p = Y_{4,p}$ for all the models except the "red" model, for which

$$Y_p = Y_{4,p} \frac{Y_{6,P} + Y_{7,P}}{K_M + Y_{6,P} + Y_{7,P}},$$

with K_M a constant for the "red" model.

4.6 Existence and Uniqueness

We now establish existence and uniqueness of the proposed model (4.20-4.21, 4.25-4.32) for any non-negative initial condition. We define the vector of unknowns

$$x(t) = (\, T_{1,m}(t), T_{4,m}(t), A_{1,p}(t), A_{4,p}(t), Y_{1,p}(t), Y_{4,p}(t), Y_{6,p}(t), Y_{7,p}(t), B_{1,p}(t), B_{4,p}(t) \,),$$

and the corresponding 18 ODEs

$$\begin{aligned}
\frac{dT_{1,m}}{dt} &= f_1(x(t)), \quad m = 0, 1, 2, 3, 4 \\
\frac{dT_{4,m}}{dt} &= f_2(x(t)), \quad m = 0, 1, 2, 3, 4 \\
\frac{dA_{1,p}}{dt} &= f_3(x(t)), \\
\frac{dA_{4,p}}{dt} &= f_4(x(t)), \\
\frac{dY_{1,p}}{dt} &= f_5(x(t)), \\
\frac{dY_{4,p}}{dt} &= f_6(x(t)), \\
\frac{dY_{6,p}}{dt} &= f_7(x(t)), \\
\frac{dY_{7,p}}{dt} &= f_8(x(t)), \\
\frac{dB_{1,p}}{dt} &= f_9(x(t)), \\
\frac{dB_{4,p}}{dt} &= f_{10}(x(t)).
\end{aligned}$$

Consider the following initial value problem

$$\begin{aligned}
x'(t) &= f(x(t)), \\
x(t_0) &= x_0.
\end{aligned} \tag{4.34}$$

where $f : \Omega \to \mathbb{R}^N$ is continuous, Ω is an open set in $\mathbb{R}^N$ and $x_0 \in \mathbb{R}^N$, $N = 18$ for the ODE system. Recall that a function f is Lipschitz if there exists a constant $K > 0$ such that

$$\|f(x) - f(y)\| \leq K\|x - y\| \tag{4.35}$$

for all $x,\ y \in \Omega$. The existence of a solution to the initial value problem given by (4.20-4.21, 4.25-4.32) with specified initial conditions can be shown easily in a straighforward approach using standard theory for ordinary differential equations (see [48, 112] for details.). The uniquness of the system will be proven by the following theorems (see [106, 56]).

Theorem 4.1 (Uniqueness). *If f is Lipschitz on each compact subset of Ω, then the initial value problem 4.34 has a unique solution.*

The next theorem specifies conditions on f which ensure that the solutions of 4.34 system are non-negative with given non-negative initial conditions.

Theorem 4.2 (Positivity). *Assume that whenever $x_0 \in \mathbb{R}^n$ satisfies $x_0 \geq 0$ with $x_{i0}(0) = 0$ for some i, then $f_i(x_0) \geq 0$. If $x_0 \in \mathbb{R}^n$ satisfies $x_0 \geq 0$, then $x(t) \geq 0$ for all $t \geq t_0$.*

We now prove non-negativity of solutions to (4.20-4.21, 4.25-4.32) system with given any non-negative initial conditions using Theorem 4.2 and then show the uniqueness of a solution by using Theorem 4.1.

Theorem 4.3. *The system (4.20-4.21, 4.25-4.32) has a non-negative solution for given any initial conditions*

$$x_0 = (T_{1,m}(0), T_{4,m}(0), A_{1,p}(0), A_{4,p}(0), Y_{1,p}(0), Y_{4,p}(0), Y_{6,p}(0), Y_{7,p}(0), B_{1,p}(0), B_{4,p}(0)) \geq 0.$$

Proof. Let us now check the non-negativity condition for our system.

1. Given $x_0 = (0, T_{4,m}(0), A_{1,p}(0), A_{4,p}(0), Y_{1,p}(0), Y_{4,p}(0), Y_{6,p}(0), Y_{7,p}(0), B_{1,p}(0), B_{4,p}(0)) \geq 0$. We obtain,

$$f_1(x_0) = r_{1,R}(1 - P_{1,m})T_{1,m-1} + r_{1,B}(P_{1,m+1}T_{1,m+1} \geq 0 \quad \text{for any m.}$$

2. Given $x_0 = (T_{1,m}(0), 0, A_{1,p}(0), A_{4,p}(0), Y_{1,p}(0), Y_{4,p}(0), Y_{6,p}(0), Y_{7,p}(0), B_{1,p}(0), B_{4,p}(0)) \geq 0$. We obtain,

$$f_2(x_0) = r_{4,R}(1 - P_{4,m})T_{4,m-1} + r_{4,B}(P_{4,m+1}T_{4,m+1} \geq 0 \quad \text{for any m.}$$

3. Given $x_0 = (T_{1,m}(0), T_{4,m}(0), 0, A_{4,p}(0), Y_{1,p}(0), Y_{4,p}(0), Y_{6,p}(0), Y_{7,p}(0), B_{1,p}(0), B_{4,p}(0)) \geq 0$. We obtain,

$$f_3(x_0) = a_{1,P}T_1^a A_{1,tot} \geq 0.$$

4. Given $x_0 = (T_{1,m}(0), T_{4,m}(0), A_{1,p}(0), 0, Y_{1,p}(0), Y_{4,p}(0), Y_{6,p}(0), Y_{7,p}(0), B_{1,p}(0), B_{4,p}(0)) \geq 0$. We obtain,

$$f_4(x_0) = a_{1,P}(T_1^a + T_4^a)A_{1,tot} \geq 0.$$

5. Given $x_0 = (T_{1,m}(0), T_{4,m}(0), A_{1,p}(0), A_{4,p}(0), 0, Y_{4,p}(0), Y_{6,p}(0), Y_{7,p}(0), B_{1,p}(0), B_{4,p}(0)) \geq 0$. We obtain,

$$f_5(x_0) = a_{1,Y}A_{1,p}Y_{1,tot} \geq 0.$$

6. Given $x_0 = (T_{1,m}(0), T_{4,m}(0), A_{1,p}(0), A_{4,p}(0), Y_{1,p}(0), 0, Y_{6,p}(0), Y_{7,p}(0), B_{1,p}(0), B_{4,p}(0)) \geq 0$. We obtain,

$$f_6(x_0) = a_{4,Y}A_{4,p}Y_{4,tot} \geq 0.$$

7. Given $x_0 = (T_{1,m}(0), T_{4,m}(0), A_{1,p}(0), A_{4,p}(0), Y_{1,p}(0), Y_{4,p}(0), 0, Y_{7,p}(0), B_{1,p}(0), B_{4,p}(0)) \geq 0$. We obtain,

$$f_7(x_0) = a_{6,Y}A_{6,p}Y_{6,tot} \geq 0.$$

8. Given $x_0 = (T_{1,m}(0), T_{4,m}(0), A_{1,p}(0), A_{4,p}(0), Y_{1,p}(0), Y_{4,p}(0), Y_{6,p}(0), 0, B_{1,p}(0), B_{4,p}(0)) \geq 0$. We obtain,

$$f_8(x_0) = a_{7,Y}A_{7,p}Y_{7,tot} \geq 0.$$

9. Given $x_0 = (T_{1,m}(0), T_{4,m}(0), A_{1,p}(0), A_{4,p}(0), Y_{1,p}(0), Y_{4,p}(0), Y_{6,p}(0), Y_{7,p}(0), 0, B_{1,p}(0)) \geq 0$. We obtain,

$$f_9(x_0) = a_{1,B}A_{1,p}B_{1,tot} \geq 0.$$

10. Given $x_0 = (T_{1,m}(0), T_{4,m}(0), A_{1,p}(0), A_{4,p}(0), Y_{1,p}(0), Y_{4,p}(0), Y_{6,p}(0), Y_{7,p}(0), B_{1,p}(0), 0) \geq 0$. We obtain,

$$f_{10}(x_0) = a_{4,B}A_{4,p}B_{1,tot} \geq 0.$$

Therefore, we have $f_i(x_0) \geq 0$ whenever $x_0 \geq 0$ with $x_{i0} = 0$ for some i. By Theorem 4.2, the solution $x(t)$ for $x_0 \geq 0$ is non-negative for all $t \geq 0$. □

Theorem 4.4. *The system (4.20-4.21, 4.25-4.32) has a unique solution for given any initial conditions.*

Proof. Uniqueness of the solution to the system (4.20-4.21, 4.25-4.32) follows from Theorem 4.1 when we show $f = (f_1, f_2, f_3, f_4, f_5, f_6, f_7, f_8, f_9, f_{10})$ is Lipschitz. We will show f is Lipschitz by showing f_i for $i = 1, \cdots, 10$ is Lipschitz. Note that every function that has bounded derivative is Lipschitz. We need to show that for $i = 1, \cdots, 10$ and $j = 1, \cdots, 10$, $\frac{\partial f_1}{\partial x_j}$ is bounded. The partial derivatives of f_1 with respect to each variables in x are as follows:

$$\frac{df_1}{dT_{1,m}} = r_{1,R}(1 - P_{1,m-1}(L))T_{1,m-1} - r_{1,B}P_{1,m}(L) + r_{1,R}(1 - P_{1,m}(L)) - r_{1,B}P_{1,m+1}(L)T_{1,m+1}$$

We have the derivatives of f_5 for each variables as following:

$$\frac{df_5}{dA_{1,p}} = a_{1,Y}Y_{1,u} - d_{1,Z}Y_{1,p}$$
$$\frac{df_5}{dY_{1,p}} = a_{1,Y}A_{1,p}(Y_{1,tot} - 1) - d_{1,Z}$$

The partial derivatives are bounded for f_1 and f_5 with respect to each variable in x. The partial derivates of f_i for $i = 2, 3, 4, 6, 7, 8, 9,$ and 10 with respect to each variable in x can be easily shown by following the same arguments as above. Since variables in x are bounded and each of the partial derivatives of f_i only depend on these variables, all the partial derivates would be bounded. Therefore, f_i for $i = 1, \cdots, 10$ with respect to each x_j for $j = 1, \cdots, 10$ is Lipschitz and the resulting f is Lipschitz. □

4.7 Numerical Schemes

The dynamical equations in the model were discretized with forward Euler time discretization. The numerical scheme was implemented and solved in FORTRAN 90, compiled with *GNU gfortran* compiler on Linux.

4.8 Numerical Simulations

The main results of the chemotaxis pathways model is decribed in this section. The protein concentrations and kinetic parameters for *A. brasilense* chemotaxis systems are not

available yet. For numerical solutions of our proposed models, the protein concentration for Che1 pathway are adopted from *E. coli* chemotaxis literature [81, 82, 107] and we take oncentrations of the proteins in Che4 pathway to be 3 times higher than the ones in Che1 pathway, except $CheY_6$ and $CheY_7$, while receptor concentrations in Che1 pathway to be 3 times higher than the ones in Che4 pathway, as found in experiments [1, 65, 45], listed in Table 4.2. The rates for Che1 and Che4 pathways are asummed to be the same and adopted from *E. coli* chemotaxis literature [81, 82, 107, 78], listed in Table 4.3.

In the simulations of each model, we measure adaptation time, which is determined as the time elapsed between application of the stimulus and the recovery of the reversal frequency to 50% of its prestimulus value. In the simulations, we measured the relaxation (adaptation) time from the main signaling pathway output $CheY_p$ since it is response regulator protein. The adaptation time is calculated as Full Width at Half Maximum (FWHM), which is the width of $Y_p(t)$ curve at half of its maximum amplitude. It has been reported that it takes about 80 seconds to return back to the prestimulus reversal frequency upon application of a stimulus for wild-type *A. brasilense* cells [43, 110]. First, parameters in probable models for *A. brasilense* chemotaxis systems were fitted so that they all produced experimental wild-type data well, as seen in Fig. 4.6. We then presented a set of numerical simulations of probable models for *A. brasilense* chemotaxis systems to invalidate all models against experiments but one of the candidate models which recapitulates all available wild-type and mutant experimental data. The only fitted parameters are $k_{1,R}$, $k_{4,R}$, and $k_{41,B}$ and the rest of parameters in the models are taken from Table 4.3 for simulations.

4.8.1 Overexpression of $CheY_4$

Overexpression of $CheY_4$ concentration in the cells, on average, five times as the concentration found in the wild-type cells at the beginning of the experiment increased adaptation time to two times the adaptation time that was measured for wild-type cells upon addition or removal of ligand. The models were simulated with over-expressed $CheY_4$ as shown in Figure 4.7. The "blue" and "gray" models did not produce the mutant experimental data. Thus, the "blue" and "gray" models were invalidated.

Table 4.2: Protein values within the *A. brasilense* chemotaxis pathways.

Parameter	Description	Value	Units
$T_{1,tot}$	T_1 concentration	15	μM
$T_{4,tot}$	T_4 concentration	5	μM
$A_{1,tot}$	$CheA_1$ concentration	5	μM
$A_{4,tot}$	$CheA_4$ concentration	15	μM
$B_{1,tot}$	$CheB_1$ concentration	0.28	μM
$B_{4,tot}$	$CheB_4$ concentration	0.84	μM
$Y_{1,tot}$	$CheY_1$ concentration	18.0	μM
$Y_{4,tot}$	$CheY_4$ concentration	54.0	μM
$Y_{6,tot}$	$CheY_6$ concentration	9.0	μM
$Y_{7,tot}$	$CheY_7$ concentration	9.0	μM
$R_{1,tot}$	$CheR_1$ concentration	0.160	μM
$R_{4,tot}$	$CheR_4$ concentration	0.480	μM

Table 4.3: The rates for the *A. brasilense* chemotaxis pathways model.

Parameter	Description	Value	Units
$a_{1,p}$	$CheA_1$ autophosphorylation by T_1	15.5	s^{-1}
$a_{4,p}$	$CheA_4$ autophosphorylation by T_4	15.5	s^{-1}
$a_{14,p}$	$CheA_4$ autophosphorylation by T_1	12.5	s^{-1}
$a_{1,Y}$	$CheA_1 \rightarrow CheY_1$ phosphorus transfer rate	100	$\mu M^{-1}s^{-1}$
$a_{4,Y}$	$CheA_4 \rightarrow CheY_4$ phosphorus transfer rate	100	$\mu M^{-1}s^{-1}$
$a_{6,Y}$	$CheA_4 \rightarrow CheY_6$ phosphorus transfer rate	100	$\mu M^{-1}s^{-1}$
$a_{7,Y}$	$CheA_4 \rightarrow CheY_7$ phosphorus transfer rate	100	$\mu M^{-1}s^{-1}$
$a_{1,B}$	$CheA_1 \rightarrow CheB_1$ phosphorus transfer rate	15	$\mu M^{-1}s^{-1}$
$a_{4,B}$	$CheA_4 \rightarrow CheB_4$ phosphorus transfer rate	15	$\mu M^{-1}s^{-1}$
$d_{1,B}$	$CheB_1$ dephosphorylation rate	1	s^{-1}
$d_{4,B}$	$CheB_4$ dephosphorylation rate	1	s^{-1}
$d_{1,Z}$	$CheY_1$ dephosphorylation rate	30	s^{-1}
$d_{4,Z}$	$CheY_4$ dephosphorylation rate	30	s^{-1}
$k_{1,B}$	$CheB_1$ catalytic constant for T_1	0.155	s^{-1}
$k_{4,B}$	$CheB_4$ catalytic constant for T_4	0.155	s^{-1}
$k_{41,B}$	$CheB_4$ catalytic constant for T_1	0.305	s^{-1}
$k_{41,B}$	$CheB_4$ catalytic constant	0.155	s^{-1}
$k_{1,R}$	$CheR_1$ catalytic constant	0.255	s^{-1}
$k_{4,R}$	$CheR_4$ catalytic constant	0.255	s^{-1}
$K_{1,B}$	$CheB_1$ Michaelis constant	0.540	μM
$K_{4,B}$	$CheB_4$ Michaelis constant	0.540	μM
$K_{1,R}$	$CheR_1$ Michaelis constant	0.364	μM
$K_{4,R}$	$CheR_4$ Michaelis constant	0.364	μM
$K_{1,d}$	The receptor-ligand dissociation rate for T_1	250	μM
$K_{4,d}$	The receptor-ligand dissociation rate for T_4	250	μM
H_S	Half saturation constant of CheY_p	3.1	μM
K_A	Michaelis constant	9	μM
K_Y	Michaelis constant	9	μM
K_M	Michaelis constant	9	μM
h	Hill coeeficient	5.5	
$P_{n,m\lambda}$	Relative activity of $T_{n,m}$	m 0 1 2 3 4 v 0 0.65 0.75 0.95 1.0 o 0 0.0 0.01 0.05 1.0	

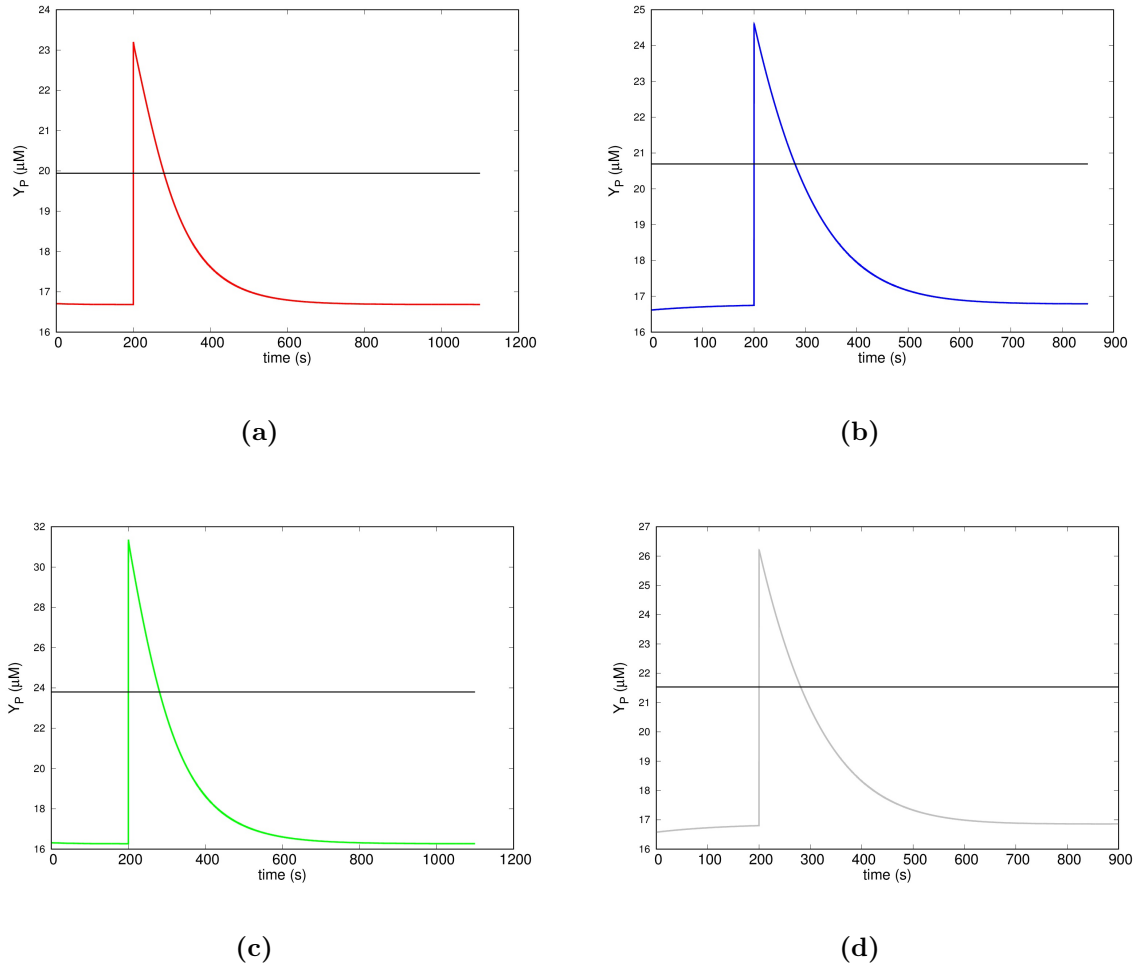

Figure 4.6: Fitting model parameters to the wild-type data of the chemotaxis system 1. Simulations of the wild-type models in response to 100 μM of ligand removed at 200 seconds. Fitted parameters $k_{1,R}$, $k_{4,R}$, and $k_{41,B}$ were fitted to wild-type data of the chemotaxis system. Other parameters in the model are taken from Table 4.3 for simulations. (a) fitted parameters $k_{1,R} = 0.819\ s^{-1}$, $k_{4,R} = 0.819\ s^{-1}$, and $k_{41,B} = 0.305\ s^{-1}$. (b) $k_{1,R} = 0.195\ s^{-1}$, $k_{4,R} = 0.195\ s^{-1}$, and $k_{41,B} = 0.195\ s^{-1}$. (c) $k_{1,R} = 0.835\ s^{-1}$, $k_{4,R} = 0.835\ s^{-1}$, and $k_{41,B} = 0.305\ s^{-1}$. (d) $k_{1,R} = 0.160\ s^{-1}$, $k_{4,R} = 0.160\ s^{-1}$, and $k_{41,B} = 205\ s^{-1}$.

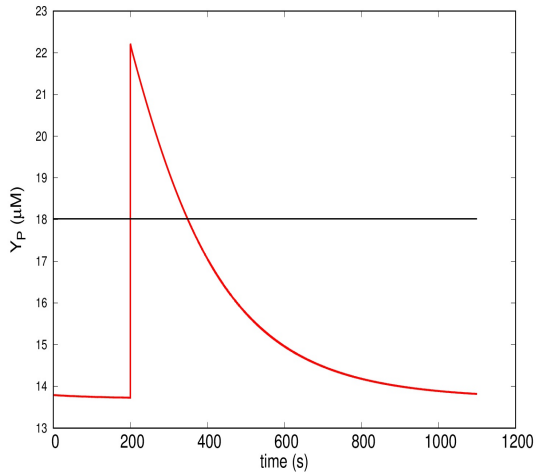

(a)

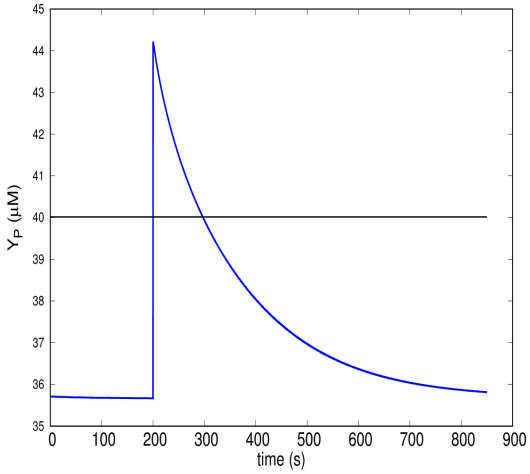

(b)

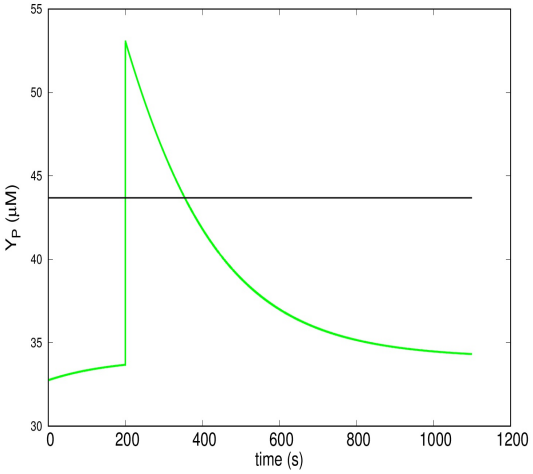

(c)

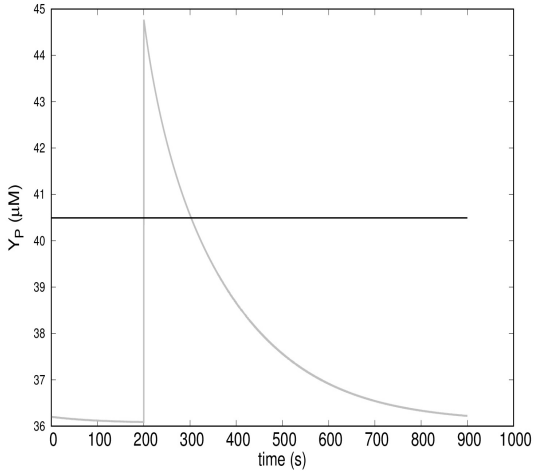

(d)

Figure 4.7: Fitting model parameters to the wild-type data of the chemotaxis system 2. Simulations of the wild-type models in response to 100 μM of ligand removed at 200 seconds. (a) It takes 148 seconds to adapt to its pre-stimulus level. (b) It takes 97 seconds. (c) It takes 154 secons. (d) It takes 102 seconds.

4.8.2 Deletion of either $CheY_6$ or $CheY_7$

Deletion of either *$CheY_6$ or $CheY_7$* resulted in the behavior that the bacteria swim without reversing their swimming direction. Thus, bacteria show no response to the addition or removal of ligand, i.e. no adaptation. The red and green models were simulated in strain that lacks $CheY_6$ or $CheY_6$ protein. The green model responds and adapts to changes in ligand concentration, whereas the red model does not respond to changes in ligand concentration. Thus, the green model was invalidated since it cannot produce the mutant data.

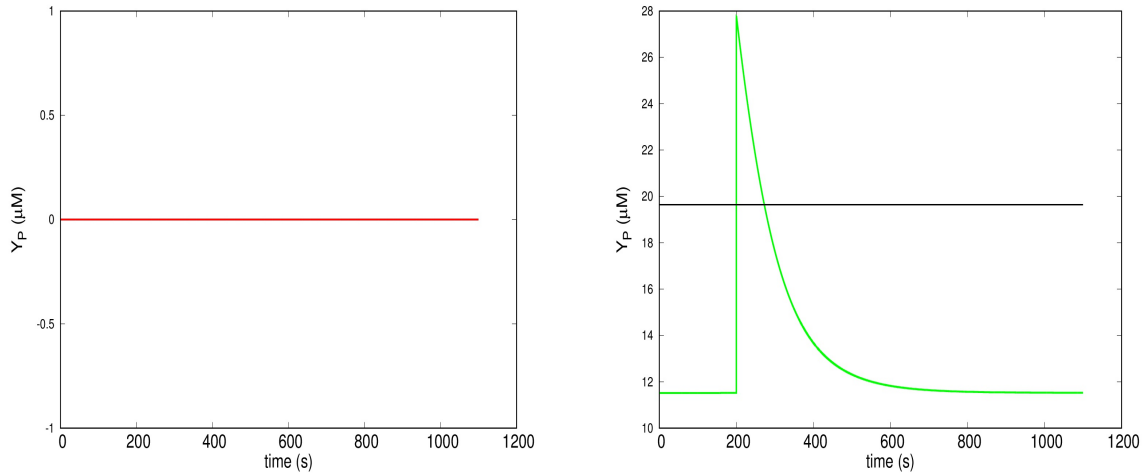

(a) **(b)**

Figure 4.8: Fitting model parameters to the wild-type data of the chemotaxis system 3. Simulations of the wild-type models in response to 100 μM of ligand removed at 200 seconds in mutant lacking $CheY_{6/7}$ strain. (a) It does not respond to changes in ligand concentration. (b) It does respond to changes in ligand concentration and adapts within 72 seconds.

4.9 Conclusions

It has been found that most motile bacteria possess multiple chemotaxis systems, in contrast to the model organism *E. coli*, which possesses one chemotaxis system [126, 97]. The available genome squence of of *A. brasilense* indicates the presence of four distinct chemotaxis operons with multiple homologues of the proteins found in *E. coli* [124]. *A. brasilense* cells use two

chemotaxis systems to regulate chemotaxis. The molecular mechanism by which *A. brasilense* bacteria use to execute chemotaxis is different from that in *E. coli*. On the other hand, there are many similarities with chemotaxis in *R. sphaeroides*, a bacterial species that has been extensively studied as a model organism for organisms for multiple chemotaxis pathways [90]. *R. sphaeroides* bacteria use two chemotaxis systems, named Che2 and Che3, to regulate the rotation of flagellar motor [47].

Experimental evidence shows that signaling outputs from Che1 and Che4 pathways, likely mediated via $CheY_1$ and $CheY_4$ are integrated at flagellar motor level in order to produce an appropriate response to changes in environmental conditions [83]. The concentration of proteins in Che4 operon are more abundant, about 3 times, than the concentration of proteins in Che1 operons, while the concentration of receptors in Che1 operon is about 3 times higher than those in Che4 operon [1, 65, 83]. Higher abundance of proteins in Che4 pathway will produce higher relaxation time after the cells are challenged with an attractant (or a repellent) via increasing (or decreasing) ligand concentration in experiments [65, 46]. We developed a mathematical model of simplest chemotaxis pathways based on these experimental results. The implication of our study is that *A. brasilense* cells use at least two chemotaxis system to regulate relaxation time in response to changes in the environment they live in. The numerical results in section 4.8 agree well with experimental results, at least qualitatively.

Unfortunately, using a more realistic model to simulate chemotaxis pathways in *A. brasilense* is still limited by the lack of quantitative experimental data and kinetic studies. For example, the contribution of other Che systems, Che2 and Che3, and other proteins in the *A. brasilense* genome to chemotaxis, cross-talk and synchronization of the two sensory pathways, the mechanism of integrating the signals produced by each of the signaling pathways to control the flagellar response, are yet unclear and under study.

Bibliography

[1] Aksenova, A. (2014). Localization of chemoreceptors in azospirillum brasilense. masters thesis. *University of Tennessee*. 73, 88, 94

[2] Alexandre, G. (2010). Coupling metabolism and chemotaxis-dependent behaviors by energy taxis receptors. *Microbiol*, 156:2283–2293. 9

[3] Alexandre, G. (2015). Chemotaxis control of transient cell aggregation. *Bacteriology*, 197(20):3230–3237. 7, 39, 66

[4] Alexandre, G., Greer, S. E., and Zhulin, I. B. (2000). Energy taxis is the dominant behavior in azospirillum brasilense. *Bacteriology*, 182:6042–6048. 3, 7, 8, 37

[5] Alexandre, G. and Zhulin, I. B. (2001). More than one way to sense chemicals. *Bacteriology*, 183(16):4681–4686. 73

[6] Alon, U., Camarena, L., Surette, M., Arcas, B. A., Liu, Y., Leibler, S., and Stock, J. B. (1998a). Response regulator output in bacterial chemotaxis. *EMBO*, 17(15):4238–4248. 40, 65, 70

[7] Alon, U., Surette, M., Barkai, N., and Leibler, S. (1998b). Robustness in bacterial chemotaxis. *Nature*, 397:168–171. 3, 68

[8] Barak, R., Nur, I., and Okon, Y. (1983). Detection of chemotaxis in azospirillum brasilense. *J. Appl. Bacteriol.*, 53:399403. 37

[9] Barak, R., Nur, I., Okon, Y., and Henis, Y. (1982). Aerotactic response of azospirillum brasilense. *Journal of Bacteriology*, 152:643–649. 37

[10] Barkai, N. and Leibler, S. (1997). Robustness in simple biochemical networks. *Nature*, 387:913–917. 40, 68, 70

[11] Beijerinck, M. W. (1883). Ueber atmungsfiguren beweglicher bakterien. *Zentrabl. Bakteriol. Parasitenkd.*, 14:827845. 6

[12] Berg, H. C. (1975). Chemotaxis in bacteria. *Annu Rev Biophys Bioeng*, 4:119136. 39, 65

[13] Berg, H. C. and Brown, D. A. (1972). Chemotaxis in escherichia coli analyzed by three-dimension tracking. *Nature*, 239:500–504. 58

[14] Bibikov, S. I., Miller, A. C., Gosink, K. K., and Parkinson, J. S. (2004). Methylation-independent aerotaxis mediated by the escherichia coli aer protein. *Journal of Bacteriology*, 186:3730–3737. 68

[15] Bible, A., Russell, M. H., and Alexandre, G. (2012). The azospirillum brasilense che1 chemotaxis pathway controls swimming velocity, which affects transient cell-to-cell clumping. *Bacteriology*, 194(13):3343–3355. 59, 71, 73, 74

[16] Bible, A. N. (2012). Characterization of the function of the azospirillum brasilense che1 chemotaxis pathway in the regulation of chemotaxis, cell length and clumping. *PhD dissertation, University of Tennessee*. 7, 10, 71

[17] Bogle, G. and Dunbar, P. R. (2013). On-latice simulation of t cell motility, chemotaxis, and trafficking in the lymph node paracortex. *PLoS ONE*, 7:e45258. 10

[18] Borkovich, K. A. and Simon, M. I. (1990). The dynamics of protein phosphorylation in bacterial chemotaxis. *Cell*, 63:1339–1348. 2, 65, 69

[19] Bourret, R. B. and Stock, A. M. (2002). Molecular information processing: lessons from bacterial chemotaxis. *J. Biol. Chem.*, 277:9625–9628. 1, 2, 65, 68

[20] Bray, D. (2001). Cell movements. *Garland Publishing, New York*. 66

[21] Bray, D., Levin, M. D., and Morton-Firth, C. J. (1998). Receptor clustering as a cellular mechanism to control sensitivity. *Nature*, 393:85–88. 66, 68, 70

[22] Brem, A. and Eisenbach, M. (2000). How signals are heard during bacterial chemotaxis: protein-protein interactions in sensory signal propagation. *Journal of Bacteriology*, 182:6865–6873. 1, 68

[23] Bubendorfer, S., Koltai, M., Rossmann, F., Sourjik, V., and Thormann, K. M. (2014). Secondary bacterial flagellar system improves bacterial spreading by increasing the directional persistence of swimming. *PNAS*, 111:11485–11490. 52

[24] Burnecki, K., Kepten, E., Garini, Y., Sikora, G., and Weron, A. (2015). Estimating the anomalous diffusion exponent for single particle tracking data with measurement errors - an alternative approach. *Nature*, 5:e11306. 48

[25] Cai, Q., Li, Z., Quayang, Q., Luo, C., and Gordon, V. D. (2016). Singly flagellated pseudomonas aeruginosa chemotaxes efficiently by unbiased motor regulation. *mBio*, 7:e00013–16. 52

[26] Cluzel, P., Surette, M., and Leibler, S. (2000). An ultrasensitive bacterial motor revealed by monitoring signaling proteins in single cells. *Science*, 287:1652–1655. 68, 83

[27] Codling, E. A., Plank, M. J., and Benhamou, S. (2008). Random walk models in biology. *J. R. Soc. Interface*, 5:813–834. 48

[28] Crocker, J. C. and Grier, D. G. (1996). Methods of digital video microscopy for colloidal studies. *Journal of Colloid and Interface Science*, 179:298–310. 42, 43

[29] Curk, T., Marenduzzo, D., and Dobnikar, J. (2013). Chemotactic sensing towards ambient and secreted attractant drives collective behavior of e. coli. *PLoS ONE*, 8:e74878. 10

[30] Eisenbach, M. (1996). Control of bacterial chemotaxis. *Molecular Microbiology*, 20:903–9010. 69

[31] Eisenbach, M. (2004). *Chemotaxis*. 39

[32] Eisenbach, M. (2011). Bacterial chemotaxis. *Encyclopedia of life sciences*. 1

[33] Eisenbach, M., Wolf, A., Welch, M., Caplan, R. Lapidus, I. R., Macnab, R. M., Aloni, H., and Asher, O. (1990). Pausing, switching and speed fluctuation of the bacterial flagellar motor and their relation to motility and chemotaxis. *J. Mol. Biol.*, 211:551–563. 2, 51, 59, 65

[34] Elmas, M., Mukherjee, T., Alexiades, V., and Alexandre, G. (2017). A two pathways model for chemotactic signaling in azospirillum brasilense. *Neural, Parallel, and Scientific Computations*, 25:345–357. 10

[35] Engelmann, T. W. (1881a). Neue methode zur untersuchung der sauerstoffausscheidung pflanzlicher und tierischer organismen. *Pflugers Arch. Gesammte Physiol.*, 25:285292. 6

[36] Engelmann, T. W. (1881b). Zur biologie der schizomyceten. *Pflugers Arch. Gesammte Physiol.*, 26:537545. 6

[37] Falke, J. J., Bass, R. B., Butler, S. L., Chervitz, S. A., and Danielson, N. A. (1997). The two-component signaling pathway of bacterial chemotaxis. *Annu. Rev. Cell Dev. Biol.*, 13:457512. 66

[38] Fatkullin, I. (2013). A study of blow-ups in the kellersegel model of chemotaxis. *Nonlinearity*, 26:81–94. 10

[39] Fischer, J. P. and Cypionka, H. (2006). Analysis of aerotactic band formation by desulfovibrio desulfuricans in a stopped-flow diffusion chamber. *FEMS Microbiol Ecol*, 55:186–194. 37

[40] Frankel, N. W., Pontius, W., Dufour, Y., Long, J., Hernandez-Nunez, L., and Emonet, T. (2014). Adaptability of non-genetic diversity in bacterial chemotaxis. *eLIFE*, 3:1–30. 10, 39, 66

[41] Gegner, J. A., Graham, D. R., Roth, A. F., and Dahlquist, F. W. (1992). Assembly of an mcp receptor, chew, and kinase chea complex in the bacterial chemotaxis signal transduction pathway. *Cell*, 70:975–982. 68, 69

[42] Gosink, K. K., Buron-Baral, M. C., and Parkionson, J. S. (2006). Signaling interactions between the aerotaxis transducer aer and heterologous chemoreceptors in escherichia coli. *Journal of Bacteriology*, 188:3487–3493. 68

[43] Greer-Phillips, S. E., Stephens, B. B., and Alexandre, G. (2004). An energy taxis transducer promotes root colonization by azospirillum brasilense. *J. Bacteriol.*, 186:6595–6604. 8, 88

[44] Grishanin, R. N., Gauden, D. E., and Armitage, J. P. (1997). Photoresponses in rhodobacter sphaeroides: role of photosynthetic electron transport. *J. Bacteriol.*, 179:2430. 2

[45] Gullett, J. M., Aksenova, A., A., H., Briegel, A., Kjr, A., Jensen, G., and Alexandre, G. (2017a). Distinct chemotaxis protein paralogs assemble into chemoreceptor signaling arrays to coordinate signaling output. *Proc Natl Acad of Sci USA*. 4, 71, 73, 88

[46] Gullett, J. M., Bible, A., and Alexandre, G. (2017b). Distinct domains of chea confer unique functions in chemotaxis and cell length in azospirillum brasilense sp7. *Journal of bacteriology*, 199. 71, 94

[47] Hamadeh, A., Roberts, M. J., Agust, E., McSharry, P. E., Maini, P. K., Armitage, J. P., and Papachritodoulou, A. (2011). Feedback control architecture and the bacterial chemotaxis network. *PLOS Computation Biology*, 7(5):1–15. 51, 71, 74, 94

[48] Hartman, P. (1964). Ordinary differential equations. *John Wiley & Sons, New York*. 84

[49] Hauri, D. C. and Ross, J. (1995). A model of excitation and adaptation in bacterial chemotaxis. *Biophysical Journal*, 68:708–722. 66, 69

[50] Hazelbauer, G. L., Falke, J. J., and Parkinson, J. S. (2008). Bacterial chemoreceptors: high-performance signaling in networked arrays. *Trends in biochemical sciences*, 33:9–19. 68

[51] Hess, J. F., Bourret, R. B., and Simon, M. I. (1988). Histidine phosphorylation and phosphoryl group transfer in bacterial chemotaxis. *Nature*, 336:139–143. 69

[52] Hintsche, M., Wljor, V., GroBmann, R., Kuhn, M. J., Thorman, K. M., Peruani, F., and Beta, C. (2017). A polar bundle of flagella can drive bacterial swimming by pushing, pulling, or coiling around the cell body. *Nature*, 14:40–49. 51, 52

[53] Horstmann, D. (2003). The keller-segel model in chemotaxis and its consequences i. *Jahresbericht der DMV*, 105:103–165. 10

[54] Horstmann, D. (2004). The keller-segel model in chemotaxis and its consequences ii. *Jahresbericht der DMV*, 106:51–69. 10

[55] Hou, S., Larsen, R. W., Boudko, D., Riley, C. W., Karatan, E., Zimmer, E., Ordal, M., and Alam, G. W. (2000). Myoglobin-like aerotaxis transducers in archaea and bacteria. *Nature*, 403:540–544. 8

[56] Hsieh, P. F. and Sibuya, Y. (1999). Basic theory of ordinary differential equations. *Springer, New York*. 84

[57] Jennings, M. S. and Crosby, J. H. (1901). Studies on reactions to stimuli in unicellular organisms. vii. the manner in which bacteria react to stimuli, especially to chemical stimuli. *Am. J. Physiol.*, 6:31–37. 6, 21

[58] Julius, A. (1975). Chemotaxis in bacteria. *Annu. Rev. Biochem.*, 44:341–356. 68

[59] Karan, F. S. N. and Chakraborty, S. (2016). Dynamics of a repulsive voter model. *IEEE Transactions on Computational Social Systems*, 3:13–22. 55

[60] Karan, F. S. N., Srinivasan, A. R., and Chakraborty, S. (2017). Modeling and numerical simulations of the influenced sznajd model. *Physical Review*, 96:022310. 55

[61] Kaul, H. and Ventikos, Y. (2013). A multi-paradigm modeling framework to simulate dynamic reciprocity in a bioreactor. *PLoS ONE*, 8:e59671. 10

[62] Keller, E. F. and Segel, L. A. (1971a). Model for chemotaxis. *J. Theor. Biol.*, 30:225–234. 10

[63] Keller, E. F. and Segel, L. A. (1971b). Model for chemotaxis. *J. Theor. Biol.*, 30:225–234. 10

[64] Koumoutsakos, P., Bayati, B., Milde, F., and Tauriello, G. (2011). Particle simulations of morphogenesis. *Math Models and Methods in Applied Sciences*, 21:955–1006. 10

[65] Kumar, D. (2012). Characterization of the che4 signal transduction pathway in taxis behaviors of azospirillum brasilense. masters thesis. *University of Tennessee*. 4, 7, 73, 74, 88, 94

[66] Lauga, E. (2016). Bacterial hydrodynamics. *Annual Review of Fluid Mechanics*, 48:105–130. 40

[67] Levit, M. N., Grebe, T. W., and Stock, J. B. (2002). Organization of the receptor-kinase signaling array that regulates escherichia coli chemotaxis. *The Journal of biological chemistry*, 277:36748–36754. 68

[68] Macnab, R. M. and Koshland, D. E. J. (1972). The gradient-sensing mechanism in bacterial chemotaxis. *Proc. Natl. Acad. Sci.*, 69(9):2509–2512. 2, 39, 65

[69] Maroulas, V. and Nebenfuhr, A. (2015). Tracking rapid intracellular movements: A bayesian random set approach. *Ann. Appl. Stat.*, 2:926–949. 40

[70] Masson, J. B., Voisinne, G., Wong-Ng, J., Celani, A., and Vergassola, M. (2012). Noninvasive inference of the molecular chemotactic response using bacterial trajectories. *PNAS*, 109:1802–1807. 46, 52

[71] Mazzaferri, J., Roy, J., Lefrancois, S., and Costantino, S. (2015). Adaptive settings for the nearest-neighbor particle tracking algorithm. *Bioinformatics*, 31:1279–1285. 44

[72] Mazzag, B. C., Zhulin, I. B., and Mogilner, A. (2003). Model of bacterial band formation in aerotaxis. *Biophysical Journal*, 85:3558–3574. 4, 9, 11, 37, 38, 71

[73] Meijering, E., Dzyubachyk, O., and Smal, I. (2012). Methods for cell and particle tracking. *Methods in Enzymology*, 504:183–200. 58

[74] Mello, B. A. and Tu, Y. (2003). Perfect and near-perfect adaptation in a model of bacterial chemotaxis. *Biophysical*, 84:2943–2956. 10, 70, 80

[75] Menolascina, F., Stocker, R., and Sontag, E. D. (2016). In-vivo indentification and control of aerotaxis in bacilus subtilis. *2016 IEEE 55th conference on decision and control (CDC), Las Vegas, NV.*, pages 764–769. 37

[76] Milton, R. J. and Kim, K. S. (1996). Medical microbiology. *University of Texas Medical Branch at Galveston, Galveston, TX*, 4th edition. 3

[77] Min, T. L., Mears, P. J., Golding, I., and Chemla, Y. R. (2012). Chemotactic adaptation kinetics of individual escherichia coli cells. *PNAS*, 109:9869–9874. 68

[78] Mingshan, L. and Hazelbauer, G. L. (2004). Cellular stoichiometry of the components of the chemotaxis signaling complex. *Journal of Bacteriology*, 186:3687–2694. 68, 88

[79] Moens, S., Michiels, K., Keihers, V., Van Leuven, F., and Vanderleyden, J. (1995). Cloning, sequencing, and phenotypic analysis of laf1,enconding the flagellin of the lateral flagella of azospirillum brasilense sp7. *J. Bacteriol.*, 177:5419–5426. 4

[80] Moens, S., Schloter, M., and Vanderleyden, J. (1996). Expression of the structural gene, laf1, encoding the flagellin of the lateral flagella in azospirillum brasilense sp7. *J. Bacteriol.*, 178:5017–5019. 4

[81] Morton-Firth, C. J. and Bray, D. (1998). Predicting temporal fluctuations in an intracellular signaling pathway. *Theory Niol*, 192:117–128. 69, 70, 74, 80, 88

[82] Morton-Firth, C. J., Shimizu, T. S., and Bray, D. (1999). A free-energy-based stochastic simulation of the tar receptor complex. *Mol Bio*, 286(4):1059–1074. 66, 70, 74, 88

[83] Mukherjee, T., Kumar, D., Burriss, N., Xie, Z., and Alexandre, G. (2016). Azospirillum brasilense chemotaxis depends on two signaling pathways regulating distinct motility parameters. *J Bacteriol*, 198:1764–1772. 4, 9, 38, 40, 59, 64, 71, 72, 74, 94

[84] O'Neal, L., Ryu, M. H., Gomelsky, M., and Alexandre, G. (2017). Optogenetic manipulation of ci-di-gmp levels reveals the role of c-di-gmp in regulating aerotaxis receptor activity in azosprillum brasilense. *J. Bacteriol.*, 199:e00020–17. 8, 9, 20, 21, 37

[85] Parkinson, J. S. (1993). Signal transduction schemes of bacteria. *Cell*, 73:857–871. 66

[86] Patlak, C. S. (1953). Random walk with persistence and external bias. *Bull. Math: Biophys.*, 15:311–338. 10

[87] Pfeffer, W. (1883). Locomotorische richtungsbewegungen durch chemische rieze. *Ber. Dtsch Bot. Ges.*, 1:524–533. 6

[88] Pisareva, A. S., Rukolainea, S. A., Samsonova, A. M., and Samsonovaa, M. G. (2015). Numerical analysis of particle trajectories in living cells under uncertainty conditions. *Biophysics*, 60:981–989. 47

[89] Pohl, O., Hintsche, M., Alirezaeizanjani, Z., Seyrich, M., Beta, C., and Stark, H. (2017). Inferring the chemotactic strategy of p. putida and e. coli using modified kramers-moyal coefficients. *PLOS Computational Biology*, 13:e1005329. 46, 51

[90] Porter, S. L. and Armitage, J. P. (2004). Phosphotransfer in rhodobacter sphaeroides chemotaxis. *J. Mol. Biol.*, 324:3545. 70, 94

[91] Qian, C., Wong, C. C., Swarup, S., and Chiam, K. H. (2013). Bacterial tethering analysis reveals a run-reverse-turn mechanism for pseudomonas species motility. *Applied and Environmental Microbiology*, 79:4734–4743. 4, 51, 52

[92] Rao, C. V., Glekas, G. D., and Ordal, G. W. (2004). Design and diversity in bacterial chemotaxis: a comperative study in escherichia coli and bacillus subtilis. *Plos Biol.*, 2:e49. 71, 74

[93] Rao, C. V., Kirby, J. R., and Arkin, A. P. (2008). The three adaptation systems of bacillus subtilis chemotaxis. *Trens Microbiol.*, 16:480–487. 71

[94] Rebbapragada, A., Johnson, M. S., Harding, G. P., Zuccharelli, A. J., Fletcher, H. M., Zhulin, I. B., and Taylor, B. L. (1997). The aer protein and the serine chemoreceptor tsr independently sense intracellular energy levels and transduce oxygen, redox, and energy signals for escherichia coli behavior. *Proc. Natl. Acad. Sci.*, 94:1054110546. 68

[95] Roberts, M. J., Elias, A., Hamadeh, A., Maini, P., McSharry, P. E., Armitage, J. P., and Papachritodoulou, A. (2009). A model invalidation-based approach for elucidating biological signalling pathways, applied to the pathway in r. sphaeroides. *BMC Systems Biology*, 3(105):1–14. 66, 69, 71

[96] Russell, M. H., Bible, A. N., Gooding, J. R., Campagna, S. R., Gomelsky, M., and Alexandre, G. (2013). Integration of the second messenger c-di-gmp into the chemotactic cignaling pathway. *mBio*, 4(2):1–13. 69, 71, 73

[97] S. L. Porter, S. L., Wadhams, G. H., and Armitage, J. P. (2011). Signal processing in complex chemotaxis pathways. *Nature Review*, 9:153–165. 3, 65, 69, 70, 93

[98] Scharf, B. E., Fahrner, K. A., and Turner, L. andBerg, H. C. (1998). Control of direction of flagellar rotation in bacterial chemotaxis. *Proc. Natl. Acad. Sci.*, 95:201–206. 69

[99] Scharf, B. E., Hynes, M. F., and Alexandre, G. (2016). Chemotaxis signaling systems in model beneficial plant-bacteria associations. *Plant Mol. Biol.*, 90:549–559. 3, 4, 7, 71

[100] Segall, J. E., Block, S. M., and Berg, H. C. (1986). Temporal comparisons in bacterial chemotaxis.. *PNAS*, 83:8987–8991. 2, 70

[101] Segel, L. A. (1976). Incorporation of receptor kinetics into a model for bacterial chemotaxis. *J. theor. Biol.*, 57:23–42. 11

[102] Segel, L. A. (1977). A theoretical study of receptor mechanisms in bacterial chemotaxis. *SIAM J. Appl. Math.*, 32:653–665. 11

[103] Sgouralis, I., Nebenfuhr, A., and Maroulas, V. (2017). A bayesian topological framework for the identification and reconstruction of subcellular motion. *SIAM Journal on Imaging Sciences*, 10:871–899. 40

[104] Shapiro, M. J., Panomitros, D., and Koshland, D. E. J. (1995). Interactions between the methylation sites of the escherichia coli aspartate receptor mediated by the methyltransferase. *Biological Chemistry*, 270(2):751–755. 40, 69

[105] Skoge, M. L., Endres, R. G., and Wngreen, N. S. (2006). Receptor-receptor coupling in bacterial chemotaxis: evidence for strongly coupled clusters. *Biophysical*, 90:4317–4326. 68

[106] Smith, H. (2011). An introduction to delay differential equations with applications to the life sciences. *Springer, New York*, 57. 84

[107] Sourjik, V. and Berg, H. C. (2002). Receptor sensitivity in bacterial chemotaxis. *Proc. Natl. Acad. Sci.*, 99(1):123–127. 88

[108] Sourjik, V. and Berg, H. C. (2004). Functional interactions between receptors in bacterial chemotaxis. *Nature*, 428:437–441. 2, 66, 68, 70

[109] Spiro, P. A., Parkinson, J. S., and Othmer, H. G. (1997). A model of excitation and adaptation in bacterial chemotaxis. *Proc. Natl. Acad. Sci.*, 94:7263–7268. 66, 69

[110] Stephens, B. B., Loar, S. N., and Alexandre, G. (2006). Role of cheb and cher in the complex chemotactic and aerotactic pathway of azospirillum brasilense. *Bacteriology*, 188(13):4759–4768. 66, 70, 71, 73, 88

[111] Stock, J. and Da Re, S. (1999). A receptor scaffold mediates stimulusresponse coupling in bacterial chemotaxis. *Cell Calcium*, 26:157–164. 2, 69

[112] Strogast, S. H. (2015). Nonlinear dynamics and chaos. *Westview press*. 84

[113] Taktikos, J., Stark, H., and Zaburdaev, V. (2013). How the motility pattern of bacteria afects their dispersal and chemotaxis. *PLoS ONE*, 8:e81936. 39

[114] Taktikos, J., Zaburdaev, V., and Stark, H. (2012). Collective dynamics of model microorganisms with chemotactic signaling. *Physical review*, 85:e051901. 10

[115] Taylor, B. L., Zhulin, I. B., and Johnson, M. S. (1999). Aerotaxis and other energy-sensing behavior in bacteria. *Microbiol*, 53:103–128. 2, 6, 8, 9, 37

[116] Theves, M., Taktikos, J., Zaburdaev, V., Stark, H., and Beta, C. (2013). A bacterial swimmer with two alternating speeds of propagation. *Biophysical Journal*, 105:1915–1924. 46, 51, 58

[117] Tindall, M. J., Maini, P. K., Porter, S. L., and Armitage, J. P. (2008a). Overview of mathematical approaches used to model bacterial chemotaxis ii: bacterial populations. *Bulletin of mathematical biology*, 70:1570–1607. 70

[118] Tindall, M. J., Porter, S. L., Maini, P. K., and Armitage, J. P. (2010). Modeling chemotaxis reveals the role of reversed phosphotransfer and a bi-functional kinase-phosphatase. *PLoS Comput Biol*, 6:e1000896. 74

[119] Tindall, M. J., Porter, S. L., Maini, P. K., Gaglia, G., and Armitage, J. P. (2008b). Overview of mathematical approaches used to model bacterial chemotaxis i: the single cell. *Bulletin of mathematical biology*, 70:1525–1569. 69, 70

[120] Vestergaard, C., Pedersen, J., Mortensen, K., and Flyvbjerg, H. (2015). Estimation of motility parameters from trajectory data. *Eur. Phys. J. Special Topics*, 224:1151–1168. 47

[121] Vladimirov, N. and Sourjik, V. (2009). Chemotaxis: how bacteria use memory. *Biol. Chem.*, 390:1097–1104. 66, 70

[122] Wadhams, G. H. and JP Armitage, J. P. (2004). Making sense of it all: bacterial chemotaxis. *Nature Rev. Mol. Cell. Biol.*, 5:1024–1037. 4, 70, 71

[123] Wedhams, G. H. and Armitage, J. P. (2004). Making sense of it all: bacterial chemotaxis. *Molecular Cell Biology*, 5:1024–1037. 2, 39, 65, 68

[124] Wisniewski-Dye, F., Borziak, K., Khalsa-Moyers, G., and Alexandre, G. e. a. (2011). Azospirillum genomes reveal transition of bacteria from aquatic to terrestrial environments. *PLoS Genet*, 7:e1002430. 71, 73, 93

[125] Wuichet, K., Alexander, R. P., and Zhulin, I. B. (2007). Comparative genomic and protein sequence analyses of a complex system controlling bacterial chemotaxis. *Methods Enzymol*, 422:1–31. 68

[126] Wuichet, K. and Zhulin, I. B. (2010). Origins and diversification of a complex signal transduction system in prokaryotes. *Sci Signal*, 3:ra50. 68, 93

[127] Xavier, M. (2010). Mean square displacement analysis of single-particle trajectories with localization error: Brownian motion in isotropic medium. *Phys Rev E. Stat Nonlin Soft Matter Phys.*, 82:041914. 48

[128] Xie, Z., Ulrich, L. E., Zhulin, I. B., and Alexandre, G. (2010). Pas domain containing chemoreceptor couples dynamic changes in metabolism with chemotaxis. *PNAS*, 107:2235–2240. 4, 7, 8, 68, 71, 73

[129] Yang, Y., He, J., Altindal, T., Xie, L., and Wu, X. L. (2015). A non-poissonian flagellar motor switch increases bacterial potential. *Biophysical Journal*, 109:1058–1069. 48

[130] Yuan, J. and Berg, H. C. (2012). Ultrasensitivity of an adaptative bacterial motor. *J. Mol. Bio*, 425:1760–1764. 68, 69, 83

[131] Yuan, J., Branch, R., Hosu, B. G., and Berg, H. C. (2012). Adaptation at the output of the chemotaxis signaling pathway. *Letter*, 484:233–237. 68, 83

[132] Zhulin, I. B. and Armitage, J. P. (1993). Motility, chemokinesis, and methylation independent chemotaxis in azospirillum brasilense. *J Bacteriol*, 175:952–958. 7, 9, 21, 40, 71

[133] Zhulin, I. B., Bespalov, V. A., Johnson, M. S., and Taylor, B. L. (1996). Oxygen taxis and proton motive force in azospirillum brasilense. *J Bacteriol*, 178:5199–5204. 3, 4, 7, 8, 9, 20, 37, 38, 71

Vita

Mustafa Elmas is originally from Suruç, Turkey and that is where he attended the first eight years of school. After completing his middle school education, Mustafa was awarded with a scholarship to study at a prestigious high school. During high school, Mustafa took part in a math competition and came in first place. That is when he realized that was a talent of his and this motivated him to study applied mathematics in college. During his undergraduate studies, he became interested in basic research and worked in computational and applied mathematics laboratory at Selçuk University. His undergraduate thesis work under supervision of Dr. Aydın Kurnaz, was to "Differential equations and their applications". When he graduated in June 2008, he started working as a high school mathematics teacher in his hometown Suruç until he moved to the United States to pursue a further education. As soon as Mustafa moved to the U.S., he applied for graduate school to get his masters degree in mathematics at University of Texas in San Antonio, Texas. Right after receiving his masters, he moved to Knoxville, Tennessee to go even further and acquire his PhD under the advisement of Dr. Vasilios Alexiades at University of Tennessee (UTK). Mustafa's research included "Mathematical models of bacterial chemotaxis" where he built mathematical models and a tracking software for automatic tracking of moving bacterial bacteria in order to characterize swimming behavior of *Azospirillum brasilense* cells. With this research, he began to value the importance and complexities of tiny organisms. During his PhD studies, he was the president and vice president of different student chapters at UTK-society for industrial and applied mathematics (SIAM) from 2016-2017, vice president of SIAM, and Society for Advancement of Chicanos/Hispanics and Native Americans in Science (SACNAS) from 2017-2018. Aside from the amazing educational accomplishments, he also is very passionate about helping minorities and those in need. He is constantly involved in

refugee and charity organizations. Mustafa's hobbies and interests include traveling, playing sports, and spending time with friends and family.